Unveiling Myelination Mechanisms in Schizophrenia

María Pascual García

Unveiling myelination mechanisms in schizophrenia

María Pascual García

Unveiling Myelination Mechanisms in Schizophrenia

Onthullen van myelinisatie mechanismen in schizofrenie

Thesis

To obtain the degree of Doctor from the Erasmus University Rotterdam by command of the rector magnificus

Prof. dr. A.L. Bredenoord

And in accordance with the decision of the Doctorate Board

The public defence shall be held on

Friday 17th March 2023 at 10.30 hrs

by

María Pascual García

born in Ciudad Real, Spain

Erasmus University Rotterdam

Doctoral committee

Promotor: Prof. dr. S.A. Kushner

Co-promotor: Dr. S. Hijazi

Other members: Prof. dr. M.C. Angulo
                    Prof. dr. Y. Elgersma
                    Dr. F.M.S. de Vrij

For my family

Table of content

Chapter 1

General introduction

Abstract

The brain is the most complex organ that animals possess. Many different cellular types, connections and specialised procedures compose the organ responsible for our actions, emotions and thoughts. Neuroscience is the branch responsible for the study of the brain, its key players and its mechanisms. Despite years of investigations, most of the machinery is still unknown. In this chapter, I will review the main aspects of the neocortex and the hippocampus, two parts of the brain implicated in important processes such as memory and decision-making. Both areas are composed of cellular elements that communicate and form an intricate neural network. Furthermore, for this sophisticated network to function efficiently, the nervous system has developed a way to enhance the speed of intracellular neuronal conduction and optimise energy expenditure: the myelin sheath. However, when this system or the cellular components fail to work, mental disorders such as schizophrenia arise. I will also summarise the main alterations found in essential areas, such as the neocortex or the hippocampus, in this psychiatric disease.

Introduction to the neocortex

There are billions of neurons in the brain, but just a few hundreds of different subcellular types, each one of them with their special characteristics and function. Identifying them is crucial to understand how the brain functions and provides us with the key to target particular brain insults and mental disorders.

Santiago Ramón y Cajal was the first to shed light on the microstructural anatomy of the brain at the beginning of the 20th century[1]. In his work, he depicted the intrinsic organisation of the neocortex, the largest and most developed region of the cerebral cortex, as well as other brain regions. The neocortex is sterotypically described as having a six-layered organization that is subdivided into columns[2] (**Figure 1a**). Each of these layers are involved in different tasks: layer I contains cell processes; layer II-III contains cells that project their axons to neighbouring areas of the neocortex; layer IV receives inputs from sensory areas; layer V and VI projects to areas outside the neocortex[3]. The function and structure across these layers also determine the distribution and morphology of the cells that reside within them. Several cell types can be distinguished within these layers, of which pyramidal cell comprise the most abundant type of neurons. The pyramidal cell name derives from their conic-shaped soma, from which originates the apical dendrite, the basal dendrites, and a single axon. This specialised structure serves to optimise local and inter-areal communication of brain structures. Precisely, the length of their axons is dependent on their long- and short-range projections, for which the complexity of their dendritic arborisation leverages the neuronal activity and plasticity[4,5]. In contrast to projection neurons, cortical interneurons keep their axons within the neocortex[6] and provide local inhibition, which is crucial for shaping and maintaining the cortical maps. Principal cells, interneurons and other non-neuronal cells named glia form cortical columns, which are the basic functional unit of the neocortex, where incoming information is processed and an output response is built. Information travels across different layers and columns in an intracolumnar and transcolumnar manner, which all together form the circuitry of the neocortex[6,7].

In his drawings, Ramón y Cajal also depicted the hippocampal formation (**Figure 1b**). The hippocampus is a structure of the cortical grey matter embedded in the temporal lobe. It belongs to the limbic system and is mainly involved in memory formation and retrieval, emotions, spatial navigation and decision making, for which it connects with many regions of the neocortex. The hippocampus - so called because of its resemblance with a seahorse (from Latin *hippocampus*) - has a curved shape named *Cornu Amonis* (CA). The CA is subdivided into four subfields from CA1-CA4, which ends

in the V-shaped region called dentate gyrus. The hippocampus receives inputs from the entorhinal cortex into the dentate gyrus and CA3 region via the perforant path. Mossy fibres connect the dentate gyrus with the CA3 region, which connects to the homolateral CA1 via Schaffer collaterals and the contralateral CA1 via the associational commissural pathway. CA1 sends projections into the subiculum that in turn send output back into the entorhinal cortex, completing a loop called the Papez circuit[8].

The hippocampus is a well-preserved structure from an evolutionary point of view. Given the critical roles subserved by this cortical region and the elegant organization of this anatomical region, a widespread heterogeneity of cellular types could explain its differential functions[9]. Like in the neocortex, pyramidal cells represent the vast majority of the cells in the dentate gyrus and the subfields of the *Cornu Ammonis*. Recent transcriptomic analyses have revealed distinct CA3 and CA1 pyramidal populations[10-12] that are homologous to neocortical pyramidal cells[13]. In contrast, analysis with RNA-sequencing of GABAergic interneurons in the hippocampal formation showed similar physiological and anatomical characteristics to those in the isocortex, with some cell types unique to the hippocampus[13]. Together, the diversity of cell types forms a network that ensures the functionality of the limbic area.
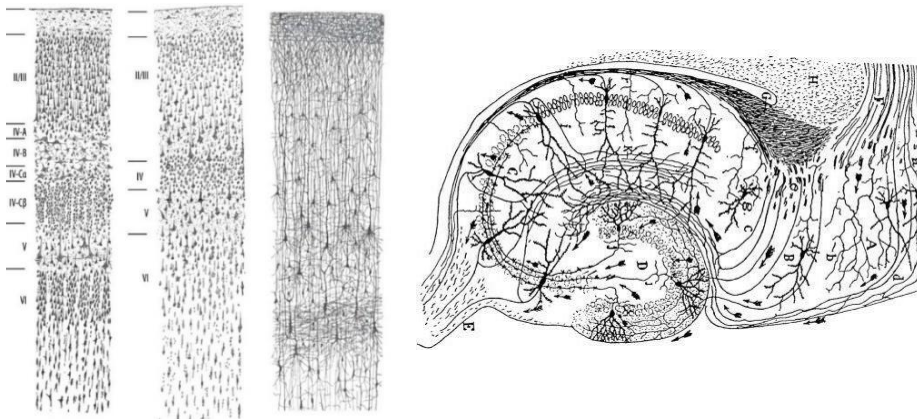
Figure 1. Drawings of the neocortex and hippocampus by Nobel laureate Santiago Ramón y Cajal. a) From left to right: Nissl and Golgi staining from human visual and motor cortex, where the six layers of the brain can be observed. **b)** Cross-section of the hippocampus. Imaged taken from Cajal Institute (CSIC), Madrid.

Connectivity of the brain and network dynamics

Pyramidal cells are the building blocks of the cerebral cortex. Information in the brain flows within and between neurons through special connections between axon and dendrites, named synapses. The specialized structure of pyramidal neurons enables them to project their axons locally and interareally, and to receive synaptic inputs onto

their dendrites. Pyramidal cells release glutamate - the main excitatory neurotransmitter in the cortex - onto the synaptic cleft of their targets, triggering an excitatory response that induces the membrane voltage potential of the postsynaptic cell to depolarize, and if reaching threshold, to generate an action potential (AP; see **Figure 4a**). In this manner, information is transmitted between cells, thereby creating a neuronal network.

Cortical and hippocampal networks are not only composed of excitatory glutamatergic pyramidal neurons, but also GABAergic inhibitory interneurons. γ -aminobutyric acid (GABA) is the main inhibitory neurotransmitter in the central nervous system (CNS). There is a large diversity of GABAergic interneuron types, each one exhibiting different anatomical, morphological, molecular and electrophysiological features. GABAergic interneurons have diverse functionality, such as regarding modulation of cellular excitability and the oscillatory activity of the brain, controlling temporal precision of pyramidal cells, synchronising cortical rhythms and maintaining excitation/inhibition (E/I) balance. Interneurons can be broadly classified into three major groups according to cell-type specific gene expression: parvalbumin (PV), somatostatin (SST) and the ionotropic serotonin receptor 5HT3aR[14] (**Figure 2**).

	PV ~40%		Sst ~30%		5HT3aR ~30%			
					Vip ~40% of 5HT3aR		non-Vip	
Morphological types	Basket	Chandelier	Martinotti	non-Martinotti	Bipolar / Multipolar; CCK small BC		SBC / NGFC; CCK large BC	
Targeting bias	Soma and proximal dendrites	Axon initial segment	Dendrites; Axonal plexus in L1	No plexus in L1	Interneurons		Synaptic and volume transmission	
Anatomical properties	•Most common IN type •Present in L2-L6 •Most prominent in L4 and L5 •Mostly multipolar dendritic arbor •Intra- and interlaminar axonal arbor •Intra- and intercolumnar axonal arbor •High connection probability to PCs and PV INs	•Mainly found in L2 and L6 •Multipolar dendritic arbor •Only target PCs •Axonal arbor largely local	•Found in L2-L6 •Abundant in L5 •Multipolar and bitufted dendritic arbor •Transcolumnar axon •Little to no connection with other SOM INs	•Found in L4 and L5 •Multipolar of bitufted dendritic arbor •No axonal plexus in L1 •L4 cells: single axonal plexus preferentially targeting PV INs •L5 cells: two axonal plexuses target both L4 and L5	•Enriched in L2/3 •Bipolar (most VIP INs): •Intracolumnar, vertically oriented dendrites crossing many layers •Intracolumnar axonal arbor		•Found in L1 •Multipolar dendritic arbor •Narrow, translaminar axon •Found in L1-6 •Small multipolar dendritic arbor •Dense axonal arbor	
Biophysical properties	FS firing pattern: •Low input resistance •Brief action potential •Can sustain high firing frequency •Little or no spike frequency adaptation	FS firing pattern slightly slower than typical FS basket cells	LTS, adapting or bursting: •High input resistance •Low max frequency firing •May show rebound spike •Spike frequency adaptation	Quasi FS: •Low input resistance •Fast action potential •High max frequency Spike frequency adaptation	•High input resistance •Many firing patterns: •Irregular spiking •Bursting •Mostly adapting		•LS firing pattern (most common) •High input resistance •Electrically coupled with other IN types	
Synaptic properties	Fast, strong and depressing excitatory inputs and inhibitory outputs	Depolarizing postsynaptic effect?	Facilitating excitatory inputs		Preferencially contact Sst INs		•Activate GABAB •Slow GABAA •Synaptic fatigue	
Other markers	Tac-1	Significant proportion expresses PV, depending on area	CR, nNOS, Reelin, NPY		CR, ChAT		Reelin, nNOS,	

Figure 2. GABAergic interneuron classification based on non-overlapping molecular markers. Morphological and biophysical properties are depicted here. Target, synaptic properties and anatomical characteristics also help with the classification of this heterogeneous GABAergic group. Figure from *Tremblay, R, et al. (2016)*[15].

PV[+] interneurons play a major role in the neocortex and hippocampus[16]. They are fast-spiking interneurons, which can fire at frequencies higher than 50 Hz. PV[+] interneurons comprise two cellular types: basket cells, which are the most common subtype and exihibit perisomatic synapses onto pyramidal cells; and chandelier cells, accounting for only 10% of PV[+] interneurons, that synapse onto pyramidal cells' axon initial segment (**Figure 3**). Basket cells receive excitatory inputs from pyramidal cells and inhibitory inputs from other PV[+] interneurons or themselves. Feedforward inhibition refers to PV[+] interneurons synapsing onto a pyramidal cell upon activation from afferent excitatory inputs[17]. During feedback inhibition, an activated pyramidal cell excites a PV[+] interneuron, which in turn inhibits the pyramidal cells back[17].
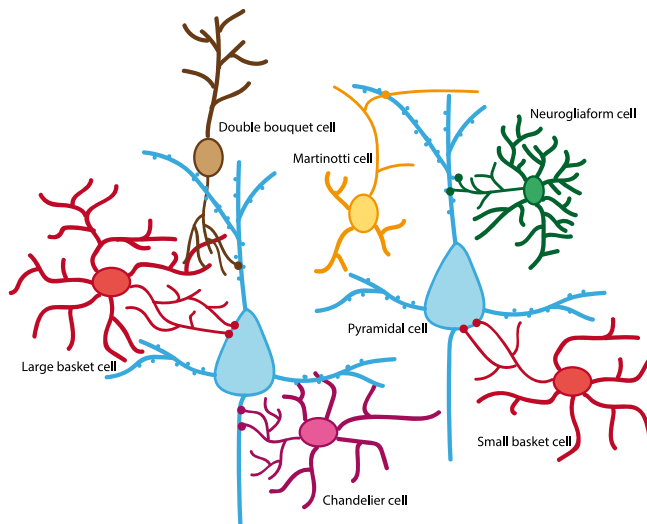

Figure 3. Outline of GABAergic cells. Pyramidal cells (blue) receive inhibitory synapses from basket cells (red) and chandelier cells (pink). Pyramidal cells also receive synaptic inputs on their tufted dendrite in layer 1 from Martinotti cells (yellow). Other cells such as double bouquet cells (in brown) contact pyramidal cells on their proximal dendrites to modulate the activity of the microcolumn. Neuroglia form cells (in green) project towards apical dendrites and provide slow cortical inhibition. Other cell types such as non-Martinotti cells, multipolar or single bouquet cells are not depicted here but also contribute to the correct functioning and synchronization of the cortical network.

Synchronization of neuronal network activity is essential to ensure proper communication within and between cortical regions. Neural oscillations are rhythmic

repetitive patterns of electrical activity that ensure synchronization of neuronal networks *in vivo*[18], and they are organised into different frequency bands[19]. These electrical patters are well preserved across species[19]. Interneurons are involved in maintenance of cortical waves. PV+ interneurons are responsible for the generation of gamma oscillations (30 – 80 Hz)[20]. These high-frequency oscillations contribute to sensory synchronisation and coordinate neuronal activity[21,22]. Thus, they are important in information processing and higher cognitive functions[23]. A deeper understanding of single-neuronal activity has greatly facilitated models of neuronal interactions in multicellular populations[24], and ultimately how information is encoded and retrieved within neural systems.

Models of neuronal activity

Neuronal activity is essential during development to regulate and refine neuronal connections through synapse formation and remodeling[25]. There are two types of synapses: electrical and chemical. In both cases, when a sufficient input current reaches the axon of the post-synaptic cell, an AP is generated (**Figure 4a**). To describe the ionic mechanisms that explain the initiation and propagation of an AP, the Nobel laureates Hodgkin and Huxley developed a mathematical model using the giant squid axon[26]. Neurons are excitable cells and each one of their components can be treated as an electrical element. In this manner, the cell membrane acts as a capacitor (Cm), where the voltage (Vm) describes the sum of changes across the membrane. Each channel type is represented as non-linear resistors. The resistance of each channel varies depending on whether the channel is open or closed. The equilibrium potential – or
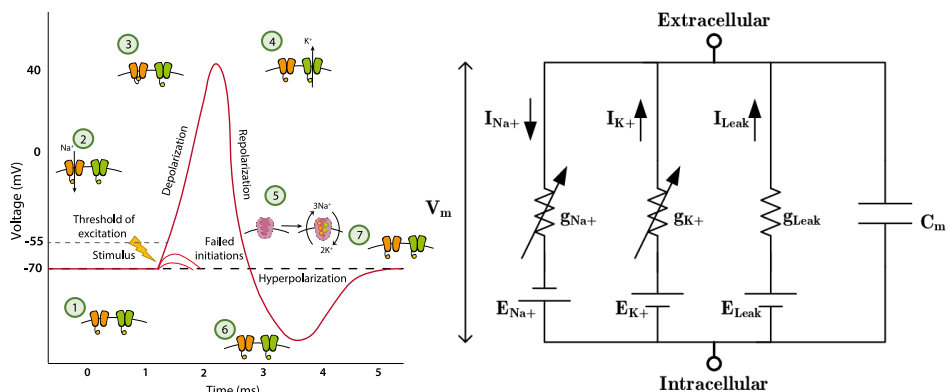
Figure 4. a) Classical phases of an action potential. *1)* Cell is at resting membrane potential. Stimuli do not generate an action potential because the membrane potential does not reach the threshold. *2)* Cell receives enough stimuli to reach the threshold, Na+v channels open and Na+ enters the cell. *3)* Na+v channels close and K+v channels begin to open. *4)* K+v channels fully open and K+ exits the cell. *5)* Na+-K+ pumps activate and three Na+ ions exit the cell while two K+ ions

enter, in order to repolarise the cell membrane. *6)* During the refractory period, K^+_v channels close. *7)* Extra K^+ ions leak down the electrochemical gradient and returns to resting state. Image adapted from BioRender. **b)** Hodgkin-Huxley model. Image from *Thanapitak, S.* (2012)[27].

electrochemical gradient -, calculated with the Nernst equation, is represented as a battery (E_n). The specific voltage-gated channels are defined by their conductance (g_n). Therefore, the total current (I) is the sum of the individual ion currents, which are a function of voltage and time (**Figure 4b**).

This complex electrical system has evolved and adapted to optimize the transmission of information. Channels in the lipid bilayer of the cellular membrane are adjusted according to the firing properties of each cellular type. This precise system of wires and connections comes at a high energetic cost. Thus, the CNS has developed different ways to cope with the metabolic expenditure[28], among which include isolation of the axonal compartment through myelination, specificity of synaptic function, glial support, or connectivity hubs (regions with a higher degree of connectivity)[29-31].

Myelin

In the CNS, we can distinguish two major anatomical compartments: grey and white matter. Grey matter is formed by the somata of neurons and glia and is responsible for most of the information processing of the CNS. White matter is composed of bundles of a fatty substance that surrounds axonal fibres, called myelin. Myelin is the lipid membrane that ensheaths axons in the peripheral nervous system (PNS) and in the CNS to enable saltatory conduction of APs. Similar to cables and wires, the myelin sheath covers axonal fibres in a manner that permits information to travel from the soma to the axonal terminal at a higher speed and with high fidelity, while also reducing the metabolic consumption of the neuron.

The extraordinary process of myelination is exclusive to vertebrates. Two glial cells – supporting cells to neurons – are in charge of insulating the axons of neurons: Schwann cells in the PNS and oligodendrocytes in the CNS. Oligodendrocytes undergo a complex differentiation process, from oligodendrocyte progenitor cells (OPCs) to myelinating oligodendrocytes (**Figure 5**).

These cells select the axons they are going to myelinate based on different molecular signals, most of which remain unknown[32]. Attractive and repulsive cues work together to establish myelination profiles[33]. Oligodendrocytes only myelinate those axons with a calibre thicker than 0.2 µm[34], but other biophysical properties such as fibre shape should also be considered[35]. Different myelination profiles are seen across layer and cellular types[36,37]. Cortical myelin plasticity is an adaptive mechanism[38], in which OPCs

and mature oligodendrocytes[39,40] adapt to changes in neuronal activity[41], and therefore refine neural circuitry. This process is essential for learning, memory and cognition[38,42].

The myelin sheath serves several purposes. The most extensively investigated is its function as an electrical insulator. The lipid bilayer that defined the internodes in the axons of some neurons reduces current leakage out of the axon and enables saltatory conduction of APs. The term saltatory refers to AP propagation through unmyelinated regions of axons, called nodes of Ranvier, that are densely populated with sodium and potassium channels. Because the flow of current is generated only at the nodes, the conduction velocity of APs is greatly increased up to 100-fold (APs can travel up to velocities of 150 m/s or 540 km/h)[43,44]. The isolation function of the myelin sheath has an indirect effect on the membrane resistance of the cell. Because channels are restricted to nodal regions, resistance is increased. On the other hand, the increase in the membrane thickness leads to a decrease in the capacitive current of the cell. Altogether, it allows a faster forward propagation of the AP.
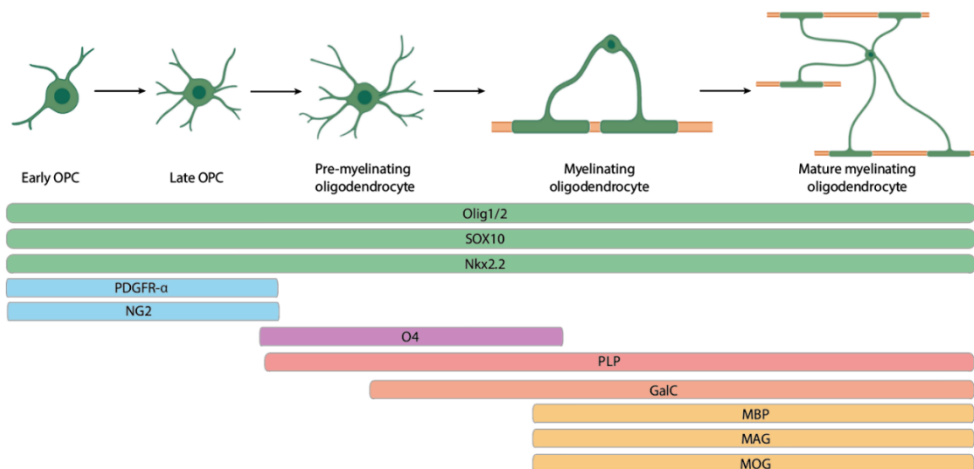
Figure 5. Differentiation and maturation process of oligodendrocyte lineage and associated markers. In the forebrain, OPCs are generated in the ventricular zone[32,45,46], from where they migrate to other areas of the brain, for which they depend on several extracellular matrix proteins[47]. Pre-myelinating oligodendrocytes start to express different proteins and glycoproteins that will enable them to start the myelinating process[34,48,49]. Mature oligodendrocytes produce myelin sheaths and express a series of myelin proteins, among which we can find myelin basic protein (MBP), proteolipid protein (PLP) and myelin associated glycoprotein (MAG)[49,50]. Different proteins are expressed at different stages of oligodendrocyte differentiation, from OPCs to mature and myelinating oligodendrocytes. Platelet-derived growth factor receptor (PDGFR-α); neural/glial antigen 2 (NG2); myelin proteolipid protein (PLP); galactocerebroside (GalC); myelin basic protein (MBP); myelin-associated glycoprotein (MAG); myelin oligodendrocyte glycoprotein (MOG). Figure based on *Kuhn, S et al. (2019)* and *Zhou, B. et al (2021)*[49,50].

Myelin substantially reduces the energetic consumption of neurons. The metabolic cost of an unmyelinated AP is high. ATP is necessary to restore the normal ionic gradients through Na^+ and K^+ -ATPases, which are more pronounced in unmyelinated axons. Oligodendrocytes provide neurons with metabolites to sustain the energy load of the cell[51]. Therefore, metabolic fuelling of myelinated axons through glial interactions and reduction of the number of open channels considerably lowers the energy demands of the cell.

Lastly, myelin-generating oligodendrocytes play an important role in the trophic support of the axon. Glia-axonal signalling is indispensable for the long-term integrity of the axon and its survival[51]. Additionally, membrane protein interactions between oligodendrocytes and neurons are also vital for the axon, without necessarily being implicated in myelin production[44]. This suggests that oligodendrocytes support axons beyond myelinating them.

## Introduction to schizophrenia

Schizophrenia is a severe and chronic psychotic disorder characterised by disturbances in cognition, perception, and behaviour. The lifetime prevalence is estimated between 0.3 to 0.7%, with an onset peak in the mid-20s[52]. The associated features of schizophrenia can be classified into three categories: positive, negative and cognitive symptoms. Positive symptoms refer to the presence of ideas or perceptions that are not typically present in people without psychosis; the most common are hallucinations, delusions, disorganised speech or catatonic behaviour. Negative symptoms are defined as characteristics which are normally present, but absent or reduced in schizophrenia, such as anhedonia, apathy, alogia or avolition. Finally, cognitive symptoms involve deficits concerning language, executive function, memory or social behaviour[53]. The presence of two or more of these symptoms for a long period of time are necessary criteria to establish a diagnosis[52].

Despite years of investigation, the pathophysiology underlying schizophrenia remains elusive. Schizophrenia is considered a polygenic disorder in which not only genetic but also environmental factors are involved in the aetiology[54] (**Figure 6**). Several hypotheses have been proposed to account for the onset and course of this disorder, however, none of them successfully fulfils all of the available data. The classical hypothesis is the dopaminergic theory, formulated in the 1960s. According to this hypothesis, the dopaminergic system becomes hyperactive in certain areas of the brain, explaining some of the positive symptoms[55]. This theory is supported by antipsychotic treatments, which block dopamine receptor D2[56]. However, the dopaminergic theory alone is unlikely to explain all the symptoms. Genome-wide association studies (GWAS)

have identified over 200 different alleles that could be linked to the course and development of schizophrenia[57]. Among these, a large proportion are related to neurotransmission[57,58]. Additionally, environmental risk factors also play a role in the disorder. Most of these agents occur during neurodevelopment[59], but also socio-economic factors[60], alcohol and drug consumption[61] have been associated with an increased risk of developing schizophrenia at older ages.

Network alterations in psychiatric disorders

Post-mortem studies in schizophrenia patients have enabled us to understand the morphological changes that the brain undergoes. At the cellular level, patients suffering from schizophrenia present a disorganised pattern of hippocampal pyramidal cells[62], and alterations in the expression of synaptic, mitochondrial or degradation genes are also found[63]. On the morphological level, pyramidal cells in the cortex showed a lower number of dendritic spines, consistent with a reduced number of excitatory inputs[64,65]. The reduced number of spines is associated with an increase of dendritic pruning triggered by an excess of synaptic glutamate[66]. The glutamate hypothesis proposes that there is a hypofunction of the NMDA receptor, a ionotropic glutamate receptor, which translates to an excess of neutrotransmitter[67,68]. Altogether, genetic and functional alterations combined can explain some of the clinical features of the disease.
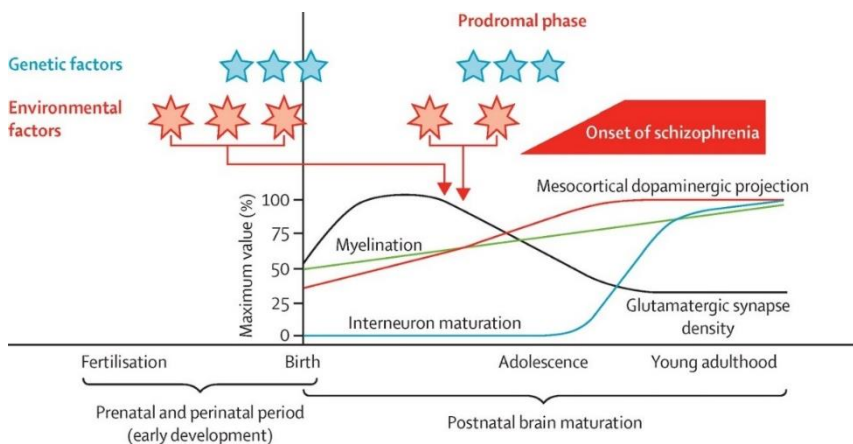
Figure 6. Interaction of genetic and environmental risk factors in the developmental pathology of schizophrenia. Effect of multiple genetic and environmental factors at prenatal and perinatal periods might lead to the development of schizophrenia by affecting important processes such as cell proliferation, neuronal migration or dendrite arborisation. Accumulation of these factors impair postnatal changes such as myelination, interneurons maturations, dopaminergic projections and glutamatergic synapses. After a prodromal phase, where some changes start to happen, there is the first psychotic event, generally during adolescence. Figure from *Owen, P, et al. (2016)*[59].

The GABAergic system is pivotal for the development and onset of psychiatric disorders. Early in development, the role of GABA is crucial for the establishment of cortical architecture[69] and cellular maturation[70-72]. Deficits in GABAergic inhibition have been widely reported in patients with schizophrenia[73]. Interneuron dysfunction has mostly focused on PV+ interneurons. Synaptic alterations and projections onto other neurons have been observed[74], and the mRNA expression of GABAergic producing enzymes, such as GAD67, and GABA levels are reduced[75-78]. PV+ interneuron intensity, a marker for neuronal activation, and density are decreased in cortical regions such as the PFC[79,80]. Furthermore, PV+ interneurons govern gamma-oscillations[81] involved during complex tasks such as attention, working memory or cognition[82], which are also altered in schizophrenia[83-85].

The E/I balance is a homeostatic and/or developmental process to maintain the ratio of excitatory and inhibitory synapses. An emerging hypothesis is that the increase in the ratio of E/I is involved in the neurophysiology of psychiatric disorders and contributes to the cognitive and behavioural deficits found in these patients[86-89]. Neurobiological mechanisms including neuronal homeostasis and deviations during development can effectively decrease E/I balance[89]. Many different dynamics explain the underlying mechanisms of the altered excitability, such as an increase in glutamatergic synapses or a decrease of inhibition. PV+ interneurons are important in the maintenance of E/I balance[90]; first, by modulating the capacity of pyramidal cells to fire, thus, opening a wide range of firing activity and input responses[91], and second, by limiting the time window of pyramidal cells to integrate excitatory inputs and produce an AP[92]. Certain regions, such as the PFC, where the E/I balance is 20/80%[93], are more susceptible to dysregulation with critical consequences for proper network functioning. Increasing inhibition in the PFC rescues some of the hallmark features of psychiatric disorders in mouse models[87,94], suggesting that E/I equilibrium is impaired in schizophrenia[90,95]. To sum up, PV+ interneurons control several fundamental processes, and loss of function can lead to aberrant cognition and behaviour.

Myelination and mental illness

Demyelination is the term employed to describe the loss of compact myelin from axons, ultimately leading to axonal damage and nerve conduction impirments[96]. It can be caused by an infection, autoimmune reactions, genetic causes or unknown reasons. Among the most well-known demyelinating diseases are multiple sclerosis and leukodystrophies. In schizophrenia, many studies link aberrant myelination with the onset and progression of the disease[59,97]. Clinical studies support that impaired myelination correlates with cognitive decline and other symptoms[98,99]. Neuroimaging studies have shown white matter abnormalities in many brain regions, especially the

corpus callosum, the frontal cortex and temporal regions[98,100]. Furthermore, several oligodendroglia markers have been found to be altered in these subjects[101,102], together with aberrant OPCs and reduced numbers of oligodendrocytes[103-106]. Notably, GWAS data pooled a handful of myelin/oligodendroglia genes associated to schizophrenia[107]. However, it is important to consider that schizophrenia is highly polygenic and many other genes and processes are associated with a higher risk of psychotic symptoms[57,108,109]. The interneuron myelination hypothesis of schizophrenia[97], for example, incorporates another participant into the myelin/oligodendrocyte equation. PV^{+} cells establish important connections with OPCs[110] and their myelination has been widely reported[37,97,111]. As these cells play important roles in network synchronisation, impaired myelination and loss of axonal integrity may be imperative for the tuning of the circuit.

Re-myelination is the process by which oligodendrocytes re-establish the myelin sheath in demyelinated axons. Myelin can be restored by establishing new myelin patterns formed by new myelinating oligodendrocytes[112,113], suggesting that recovery of the myelin sheath might reverse some of the symptoms. Indeed, novel pharmacological approaches that enhance remyelination have been introduced as potential therapeutic treatments for schizophrenia[114,115], suggesting possible alternatives to classical antipsychotic therapies.

Scope and outline of this thesis

The aim of this thesis is to unveil mechanisms that explain myelination of excitatory and inhibitory neurons in the neocortex and its relationship with psychiatric disorders such as schizophrenia. To that end, we will navigate through different cellular types with special emphasis on GABAergic interneurons, a minority neuronal population that has gained its way to the spotlight due to the important processes they are involved in, and their key role in psychiatric disorders.

Chapter 1 describes the main known findings of the literature related to interneurons, myelination and schizophrenia, and aims to lay the foundations for the upcoming chapters.

In *Chapter 2*, we explored the fundamental relationship between pyramidal cells and their myelination status. We found that this relationship is not only dependent on axon morphology but also brain region- and layer-dependent. Remarkably, human pyramidal cells also showed a strong association between myelination and axonal morphology.

In *Chapter 3*, we studied non-fast-spiking interneuron myelination, an understudied population of GABAergic interneurons. Myelination in the mouse brain was scarce across non-fast-spiking interneurons. Surprisingly however, human non-fast-spiking interneurons are often myelinated, indicating inter-species differences in these cellular types. Human interneurons also displayed a robust correlation between myelination and axonal morphology.

In *Chapter 4*, we examined the relationship between axonal morphology and myelination in fast-spiking interneurons. We observed that the joint combination of axonal calibre and length are strong predictors of interneuron myelination. Across species, human and mouse, predictive axonal thresholds were maintained.

In *Chapter 5*, we assessed the impact of lack or loss of myelin on PV$^+$ interneurons. The effects on brain activity, and in particular over slow brain waves, which are inhibited by PV$^+$ interneurons, were impacted by impaired myelination, but could be restored upon re-activation of myelin-deficient PV$^+$ interneurons.

In *Chapter 6*, we investigated the consequences of demyelination over self-inhibition in PV$^+$ interneurons. We found that impairing myelination at young ages has detrimental effects on the number of autapses and the firing properties of these cells. Re-myelination leads to partial recovery of these deficits.

In *Chapter 7*, we analysed the effect on myelination of a gene mutation known to be critical for changes in cellular morphology. We found that despite this mutation, oligodendrocytes were able to form myelin sheaths normally and there were no discernible impairments in the firing pattern of PV$^+$ interneurons.

In *Chapter 8*, we carried out electrophysiological and immunohistochemical experiments to understand the hyperexcitability of PV$^+$ interneurons in a mouse model of the 22q11 syndrome, which increases the risk of schizophrenia. We found that potassium channels play an important role in the excitability of these cells and that their modulation was not affected by specific agonists or antagonists, suggesting that these channels are not functional.

Finally, in *Chapter 9*, I critically review the main findings of the previous research and their significance in both fundamental and translational neurobiology. I focus on myelination of interneurons and the role they play in neuropsychiatric disorders, and propose mechanisms that could contribute to the consequentially aberrant functioning of cortical networks.

References

1.   DeFelipe, J. Sesquicentenary of the birthday of Santiago Ramón y Cajal, the father of modern neuroscience. *Trends Neurosci.* **25**, 481–484 (2002).
2.   Molnár, Z. Cortical Columns. in *Neural Circuit Development and Function in the Brain* 109–129 (Elsevier, 2013).
3.   Purves, D. *et al.* An Overview of Cortical Structure. (2001).
4.   DeFelipe, J. & Fariñas, I. The pyramidal neuron of the cerebral cortex: morphologycal and chemical characteristics of the synaptic inputs. **39**, (1992).
5.   Benavides-Piccione, R., Rojo, C., Kastanauskaite, A. & DeFelipe, J. Variation in Pyramidal Cell Morphology Across the Human Anterior Temporal Lobe. *Cereb. Cortex* **31**, 3592–3609 (2021).
6.   DeFelipe, J. *et al.* New insights into the classification and nomenclature of cortical GABAergic interneurons. *Nat. Rev. Neurosci. 2013 143* **14**, 202–216 (2013).
7.   Hawkins, J., Ahmad, S. & Cui, Y. A theory of how columns in the neocortex enable learning the structure of the world. *Front. Neural Circuits* **11**, 81 (2017).
8.   Fogwe, L. A., Reddy, V. & Mesfin, F. B. Neuroanatomy, Hippocampus. *StatPearls* (2021).
9.   Cembrowski, M. S. & Spruston, N. Heterogeneity within classical cell types is the rule: lessons from hippocampal pyramidal neurons. *Nat. Rev. Neurosci. 2019 204* **20**, 193–204 (2019).
10.   Thompson, C. L. *et al.* Genomic Anatomy of the Hippocampus. *Neuron* **60**, 1010–1021 (2008).
11.   Cembrowski, M. S. *et al.* Spatial Gene-Expression Gradients Underlie Prominent Heterogeneity of CA1 Pyramidal Neurons. *Neuron* **89**, 351–368 (2016).
12.   Cembrowski, M. S. *et al.* Dissociable Structural and Functional Hippocampal Outputs via Distinct Subiculum Cell Classes. *Cell* **173**, 1280-1292.e18 (2018).
13.   Yao, Z. *et al.* A taxonomy of transcriptomic cell types across the isocortex and hippocampal formation. *Cell* **184**, 3222-3241.e26 (2021).
14.   Rudy, B., Fishell, G., Lee, S. H. & Hjerling-Leffler, J. Three Groups of Interneurons Account for Nearly 100% of Neocortical GABAergic Neurons. *Dev. Neurobiol.* **71**, 45 (2011).
15.   Tremblay, R., Lee, S. & Rudy, B. Review GABAergic Interneurons in the Neocortex: From Cellular Properties to Circuits. (2016).
16.   Nahar, L., Delacroix, B. M. & Nam, H. W. The Role of Parvalbumin Interneurons in Neurotransmitter Balance and Neurological Disease. *Front. Psychiatry* **12**, 679960 (2021).
17.   Hu, H., Gan, J. & Jonas, P. Fast-spiking, parvalbumin+ GABAergic interneurons: From cellular design to microcircuit function. *Science (80-.).* **345**, (2014).
18.   Başar, E. Brain oscillations in neuropsychiatric disease. *Dialogues Clin. Neurosci.* **15**, 291 (2013).
19.   Buzsáki, G. & Draguhn, A. Neuronal Oscillations in Cortical Networks. *Science (80-.).* **304**, 1926–1929 (2004).
20.   Sohal, V. S., Zhang, F., Yizhar, O. & Deisseroth, K. Parvalbumin neurons and gamma rhythms enhance cortical circuit performance. *Nat. 2009 4597247* **459**, 698–702 (2009).
21.   Singer, W. Neuronal Synchrony: A Versatile Code for the Definition of Relations? *Neuron* **24**, 49–65 (1999).
22.   Uhlhaas, P. J. & Singer, W. Neural Synchrony in Brain Disorders: Relevance for Cognitive Dysfunctions and Pathophysiology. *Neuron* **52**, 155–168 (2006).
23.   Howard, M. W. *et al.* Gamma Oscillations Correlate with Working Memory Load in Humans. *Cereb. Cortex* **13**, 1369–1374 (2003).
24.   Mureşan, R. C., Jurjuţ, O. F., Moca, V. V., Singer, W. & Nikolić, D. The oscillation score: An efficient method for estimating oscillation strength in neuronal activity. *J. Neurophysiol.* **99**, 1333–1353 (2008).
25.   Hua, J. Y. & Smith, S. J. Neural activity and the dynamics of central nervous system development. *Nat. Neurosci. 2004 74* **7**, 327–332 (2004).
26.   Hodgkin, A. L. & Huxley, A. F. A quantitative description of membrane current and its application to conduction and excitation in nerve. *J. Physiol* 500–544 (1952).
27.   Thanapitak, S. Bionics Chemical Synapse. **7**, (2011).
28.   Attwell, D. & Laughlin, S. B. An energy budget for signaling in the grey matter of the brain. *J. Cereb. Blood Flow Metab.* **21**, 1133–1145 (2001).
29.   Tomasi, D., Wang, G. J. & Volkow, N. D. Energetic cost of brain functional connectivity. *Proc. Natl. Acad. Sci. U. S. A.* **110**, 13642–13647 (2013).
30.   Afridi, R., Kim, J. H., Rahman, M. H. & Suk, K. Metabolic Regulation of Glial Phenotypes: Implications in Neuron–Glia Interactions and Neurological Disorders. *Front. Cell. Neurosci.* **14**, 20 (2020).
31.   Lezmy, J., Harris, J. J. & Attwell, D. Optimising the energetic cost of the glutamatergic synapse. *Neuropharmacology* **197**, 108727 (2021).
32.   Bradl, M. & Lassmann, H. Oligodendrocytes: biology and pathology. *Acta Neuropathol.* **119**, 37 (2010).
33.   Redmond, S. A. *et al.* Somatodendritic Expression of JAM2 Inhibits Oligodendrocyte Myelination. *Neuron* **91**, 824–836 (2016).
34.   Simons, M. & Trajkovic, K. Neuron-glia communication in the control of oligodendrocyte function and myelin biogenesis. *J. Cell Sci.* **119**, 4381–4389 (2006).

35. Almeida, R. G. The rules of attraction in central nervous system myelination. *Front. Cell. Neurosci.* **12**, 367 (2018).
36. Tomassy, G. S. *et al.* Distinct Profiles of Myelin Distribution. *Science (80-.).* **344**, 319–324 (2014).
37. Stedehouder, J. *et al.* Fast-spiking Parvalbumin Interneurons are Frequently Myelinated in the Cerebral Cortex of Mice and Humans. *Cereb. Cortex* **27**, 5001–5013 (2017).
38. Bonetto, G., Kamen, Y., Evans, K. A. & Káradóttir, R. T. Unraveling Myelin Plasticity. *Front. Cell. Neurosci.* **14**, 156 (2020).
39. Hill, R. A., Li, A. M. & Grutzendler, J. Lifelong cortical myelin plasticity and age-related degeneration in the live mammalian brain. *Nat. Neurosci.* **21**, 683–695 (2018).
40. Hughes, E. G., Orthmann-Murphy, J. L., Langseth, A. J. & Bergles, D. E. Myelin remodeling through experience-dependent oligodendrogenesis in the adult somatosensory cortex. *Nat. Neurosci.* **21**, 696–706 (2018).
41. Gibson, E. M. *et al.* Neuronal activity promotes oligodendrogenesis and adaptive myelination in the mammalian brain. *Science (80-.).* **1252304**, (2014).
42. Xin, W. & Chan, J. R. Myelin plasticity: sculpting circuits in learning and memory. *Nat. Rev. Neurosci.* **21**, 682 (2020).
43. Purves, D. *et al.* Increased Conduction Velocity as a Result of Myelination. (2001).
44. Nave, K.-A. Myelination and support of axonal integrity by glia. *Nat. 2010 4687321* **468**, 244–252 (2010).
45. Pringle, N. P. & Richardson, W. D. A singularity of PDGF alpha-receptor expression in the dorsoventral axis of the neural tube may define the origin of the oligodendrocyte lineage. *Development* **117**, 525–533 (1993).
46. Timsit, S. *et al.* Oligodendrocytes originate in a restricted zone of the embryonic ventral neural tube defined by DM-20 mRNA expression. *J. Neurosci.* **15**, 1012 (1995).
47. Frost, E., Kiernan, B. W., Faissner, A. & Constant, C. Regulation of oligodendrocyte precursor migration by extracellular matrix: evidence for substrate-specific inhibition of migration by tenascin-C. *Dev. Neurosci.* **18**, 266–273 (1996).
48. Butts, B. D., Houde, C. & Mehmet, H. Maturation-dependent sensitivity of oligodendrocyte lineage cells to apoptosis: implications for normal development and disease. *Cell Death Differ. 2008 157* **15**, 1178–1186 (2008).
49. Zhou, B., Zhu, Z., Ransom, B. R. & Tong, X. Oligodendrocyte lineage cells and depression. *Mol. Psychiatry* **26**, 103–117 (2021).
50. Kuhn, S., Gritti, L., Crooks, D. & Dombrowski, Y. Oligodendrocytes in Development, Myelin Generation and Beyond. *Cells* **8**, 1424 (2019).
51. Nave, K.-A. Myelination and the trophic support of long axons. *Nat. Rev. Neurosci. 2010 114* **11**, 275–283 (2010).
52. American Psychiatric Association. Diagnostic and Statistical Manual of Mental Disorders. (2013).
53. Holder, S. D. & Wayhs, A. Schizophrenia. *Am. Fam. Physician* **90**, 775–782 (2014).
54. Schultz, S. H., North, S. W. & Shields, C. G. Schizophrenia: A Review. *Am. Fam. Physician* **75**, 1821–1829 (2007).
55. Toda, M. & Abi-Dargham, A. Dopamine hypothesis of schizophrenia: Making sense of it all. *Curr. Psychiatry Rep.* **9**, 329–336 (2007).
56. Abi-Dargham, A. *et al.* Increased baseline occupancy of D2 receptors by dopamine in schizophrenia. *Proc. Natl. Acad. Sci.* **97**, 8104–8109 (2000).
57. Ripke, S. *et al.* Biological insights from 108 schizophrenia-associated genetic loci. *Nat. 2014 5117510* **511**, 421–427 (2014).
58. Devor, A. *et al.* Genetic evidence for role of integration of fast and slow neurotransmission in schizophrenia. *Mol. Psychiatry* **22**, 792 (2017).
59. Owen, P. M. J., Sawa, P. A. & Mortensen, P. P. B. Schizophrenia. *Lancet (London, England)* **388**, 86 (2016).
60. Werner, S., Malaspina, D. & Rabinowitz, J. Socioeconomic Status at Birth Is Associated With Risk of Schizophrenia: Population-Based Multilevel Study. *Schizophr. Bull.* **33**, 1373 (2007).
61. Kendler, K. S., Ohlsson, H., Sundquist, J. & Sundquist, K. Prediction of Onset of Substance-Induced Psychotic Disorder and its Progression to Schizophrenia in a Swedish National Sample. *Am. J. Psychiatry* **176**, 711 (2019).
62. Conrad, A. J., Abebe, T., Austin, R., Forsythe, S. & Scheibel, A. B. Hippocampal Pyramidal Cell Disarray in Schizophrenia as a Bilateral Phenomenon. *Arch. Gen. Psychiatry* **48**, 413–417 (1991).
63. Arion, D. *et al.* Distinctive transcriptome alterations of prefrontal pyramidal neurons in schizophrenia and schizoaffective disorder. *Mol. Psychiatry* **20**, 1397–1405 (2015).
64. Garey, L. J. *et al.* Reduced dendritic spine density on cerebral cortical pyramidal neurons in schizophrenia. *J. Neurol. Neurosurg. Psychiatry* **65**, 446–453 (1998).
65. Glantz, L. A. & Lewis, D. A. Decreased dendritic spine density on prefrontal cortical pyramidal neurons in schizophrenia. *Arch. Gen. Psychiatry* **57**, 65–73 (2000).
66. Parellada, E. & Gassó, P. Glutamate and microglia activation as a driver of dendritic apoptosis: a core pathophysiological mechanism to understand schizophrenia. *Transl. Psychiatry 2021 111* **11**, 1–13 (2021).
67. Harrison, P. J., Law, A. J. & Eastwood, S. L. Glutamate receptors and transporters in the hippocampus in schizophrenia. *Ann. N. Y. Acad. Sci.* **1003**, 94–101 (2003).

68. Bauer, D., Gupta, D., Harotunian, V., Meador-Woodruff, J. H. & McCullumsmith, R. E. Abnormal Expression of Glutamate Transporter and Transporter Interacting Molecules in Prefrontal Cortex in Elderly Patients with Schizophrenia. *Schizophr. Res.* **104**, 108 (2008).

69. Haas, M. *et al.* Perturbations in cortical development and neuronal network excitability arising from prenatal exposure to benzodiazepines in mice. *Eur. J. Neurosci.* **37**, 1584–1593 (2013).

70. Huang, Z. J. Activity-dependent development of inhibitory synapses and innervation pattern: role of GABA signalling and beyond. *J. Physiol.* **587**, 1881 (2009).

71. Wu, X. *et al.* GABA Signaling Promotes Synapse Elimination and Axon Pruning in Developing Cortical Inhibitory Interneurons. *J. Neurosci.* **32**, 331 (2012).

72. Jahangir, M., Zhou, J. S., Lang, B. & Wang, X. P. GABAergic System Dysfunction and Challenges in Schizophrenia Research. *Front. Cell Dev. Biol.* **9**, 1042 (2021).

73. Lewis, D. A. Inhibitory Neurons in Human Cortical Circuits: Substrate for Cognitive Dysfunction in Schizophrenia. *Curr. Opin. Neurobiol.* **0**, 22 (2014).

74. Lewis, D. A. The Chandelier Neuron in Schizophrenia. *Dev. Neurobiol.* **71**, 118 (2011).

75. Perry, T. L., Buchanan, J., Kish, S. J. & Hansen, S. Gamma-aminobutyric-acid deficiency in brain of schizophrenic patients. *Lancet (London, England)* **1**, 237–239 (1979).

76. Volk, D. W., Austin, M. C., Pierri, J. N., Sampson, A. R. & Lewis, D. A. Decreased Glutamic Acid Decarboxylase67 Messenger RNA Expression in a Subset of Prefrontal Cortical γ-Aminobutyric Acid Neurons in Subjects With Schizophrenia. *Arch. Gen. Psychiatry* **57**, 237–245 (2000).

77. Guidotti, A. *et al.* Decrease in reelin and glutamic acid decarboxylase67 (GAD67) expression in schizophrenia and bipolar disorder: a postmortem brain study. *Arch. Gen. Psychiatry* **57**, 1061–1069 (2000).

78. Fatemi, S. H. *et al.* Glutamic acid decarboxylase 65 and 67 kDa proteins are reduced in autistic parietal and cerebellar cortices. *Biol. Psychiatry* **52**, 805–810 (2002).

79. Beasley, C. L., Zhang, Z. J., Patten, I. & Reynolds, G. P. Selective deficits in prefrontal cortical GABAergic neurons in schizophrenia defined by the presence of calcium-binding proteins. *Biol. Psychiatry* **52**, 708–715 (2002).

80. Enwright, J. F. *et al.* Reduced Labeling of Parvalbumin Neurons and Perineuronal Nets in the Dorsolateral Prefrontal Cortex of Subjects with Schizophrenia. *Neuropsychopharmacology* **41**, 2206 (2016).

81. Buzśaki, G. & Wang, X. J. Mechanisms of Gamma Oscillations. *Annu. Rev. Neurosci.* **35**, 203 (2012).

82. González-Burgos, G., Cho, R. Y. & Lewis, D. A. Alterations in Cortical Network Oscillations and Parvalbumin Neurons in Schizophrenia. *Biol. Psychiatry* **77**, 1031 (2015).

83. Lewis, D. A., Hashimoto, T. & Volk, D. W. Cortical inhibitory neurons and schizophrenia. *Nat. Rev. Neurosci. 2005 64* **6**, 312–324 (2005).

84. Cho, R. Y., Konecky, R. O. & Carter, C. S. Impairments in frontal cortical γ synchrony and cognitive control in schizophrenia. *Proc. Natl. Acad. Sci. U. S. A.* **103**, 19878–19883 (2006).

85. McNally, J. M. & McCarley, R. W. Gamma band oscillations: a key to understanding schizophrenia symptoms and neural circuit abnormalities. *Curr. Opin. Psychiatry* **29**, 202 (2016).

86. Rubenstein, J. L. R. & Merzenich, M. M. Model of autism: increased ratio of excitation/inhibition in key neural systems. *Genes, Brain Behav.* **2**, 255–267 (2003).

87. Yizhar, O. *et al.* Neocortical excitation/inhibition balance in information processing and social dysfunction. *Nat. 2011 4777363* **477**, 171–178 (2011).

88. Foss-Feig, J. H. *et al.* Searching for Cross-diagnostic Convergence: Neural Mechanisms Governing Excitation and Inhibition Balance in Schizophrenia and Autism Spectrum Disorders. *Biol. Psychiatry* **81**, 848 (2017).

89. Sohal, V. S. & Rubenstein, J. L. R. Excitation-inhibition balance as a framework for investigating mechanisms in neuropsychiatric disorders. *Mol. Psychiatry 2019 249* **24**, 1248–1257 (2019).

90. Lewis, D. A., Curley, A. A., Glausier, J. R. & Volk, D. W. Cortical Parvalbumin Interneurons and Cognitive Dysfunction in Schizophrenia. *Trends Neurosci.* **35**, 57 (2012).

91. Isaacson, J. S. & Scanziani, M. How Inhibition Shapes Cortical Activity. *Neuron* **72**, 231 (2011).

92. Delevich, K., Tucciarone, J., Huang, Z. J. & Li, B. The Mediodorsal Thalamus Drives Feedforward Inhibition in the Anterior Cingulate Cortex via Parvalbumin Interneurons. *J. Neurosci.* **35**, 5743 (2015).

93. Le Roux, N., Amar, M., Baux, G. & Fossier, P. Homeostatic control of the excitation–inhibition balance in cortical layer 5 pyramidal neurons. *Eur. J. Neurosci.* **24**, 3507–3518 (2006).

94. Lam, N. H. *et al.* Effects of Altered Excitation-Inhibition Balance on Decision Making in a Cortical Circuit Model. *J. Neurosci.* **42**, 1035–1053 (2022).

95. Lisman, J. Excitation, inhibition, local oscillations, or large-scale loops: what causes the symptoms of schizophrenia? *Curr. Opin. Neurobiol.* **22**, 537 (2012).

96. Mitew, S., Xing, Y. L. & Merson, T. D. Axonal activity-dependent myelination in development: Insights for myelin repair. *J. Chem. Neuroanat.* **76**, 2–8 (2016).

97. Stedehouder, J. & Kushner, S. A. Myelination of parvalbumin interneurons: a parsimonious locus of pathophysiological convergence in schizophrenia. *Mol. Psychiatry* **22**, 4–12 (2017).

98. Fields, R. D. White matter in learning, cognition and psychiatric disorders. *Trends Neurosci.* **31**, 361 (2008).

99. Voineskos, A. N. *et al.* Oligodendrocyte Genes, White Matter Tract Integrity, and Cognition in

Schizophrenia. *Cereb. Cortex* **23**, 2044–2057 (2013).

100. Kubicki, M., McCarley, R. W. & Shenton, M. E. Evidence for white matter abnormalities in schizophrenia. *Curr. Opin. Psychiatry* **18**, 121 (2005).
101. Georgieva, L. *et al.* Convergent evidence that oligodendrocyte lineage transcription factor 2 (OLIG2) and interacting genes influence susceptibility to schizophrenia. *Proc. Natl. Acad. Sci. U. S. A.* **103**, 12469–12474 (2006).
102. Voineskos, A. N. *et al.* A family-based association study of the myelin-associated glycoprotein and 2′,3′-cyclic nucleotide 3′-phosphodiesterase genes with schizophrenia. *Psychiatr. Genet.* **18**, 143–146 (2008).
103. Takahashi, N., Sakurai, T., Davis, K. L. & Buxbaum, J. D. Linking oligodendrocyte and myelin dysfunction to neurocircuitry abnormalities in schizophrenia. *Prog. Neurobiol.* **93**, 13 (2011).
104. Vostrikov, V. M. & Uranova, N. A. Reduced density of oligodendrocytes and oligodendrocyte clusters in the caudate nucleus in major psychiatric illnesses. *Schizophr. Res.* (2019).
105. de Vrij, F. M. *et al.* Candidate CSPG4 mutations and induced pluripotent stem cell modeling implicate oligodendrocyte progenitor cell dysfunction in familial schizophrenia. *Mol. Psychiatry* **24**, 757 (2019).
106. Kolomeets, N. S. & Uranova, N. A. Reduced number of satellite oligodendrocytes of pyramidal neurons in layer 5 of the prefrontal cortex in schizophrenia. *Eur. Arch. Psychiatry Clin. Neurosci. 2021* 1–9 (2021).
107. Roussos, P. & Haroutunian, V. Schizophrenia: Susceptibility genes and oligodendroglial and myelin related abnormalities. *Front. Cell. Neurosci.* **8**, 5 (2014).
108. Hakak, Y. *et al.* Genome-wide expression analysis reveals dysregulation of myelination-related genes in chronic schizophrenia. *Proc. Natl. Acad. Sci. U. S. A.* **98**, 4746–4751 (2001).
109. Jaffe, A. E. *et al.* Developmental and genetic regulation of the human cortex transcriptome illuminate schizophrenia pathogenesis. *Nat. Neurosci. 2018 218* **21**, 1117–1125 (2018).
110. Orduz, D. *et al.* Interneurons and oligodendrocyte progenitors form a structured synaptic network in the developing neocortex. *Elife* **4**, 1–53 (2015).
111. Micheva, K. D. *et al.* A large fraction of neocortical myelin ensheathes axons of local inhibitory neurons. *Elife* **5**, (2016).
112. Snaidero, N. *et al.* Myelin replacement triggered by single-cell demyelination in mouse cortex. *Nat. Commun.* **11**, 4901 (2020).
113. Orthmann-Murphy, J. *et al.* Remyelination alters the pattern of myelin in the cerebral cortex. *Elife* **9**, 1–61 (2020).
114. Li, Z., He, Y., Fan, S. & Sun, B. Clemastine rescues behavioral changes and enhances remyelination in the cuprizone mouse model of demyelination. *Neurosci Bull* **31**, 617–625 (2015).
115. Liu, J. *et al.* Clemastine Enhances Myelination in the Prefrontal Cortex and Rescues Behavioral Changes in Socially Isolated Mice. *J. Neurosci.* **36**, 957 (2016).

Chapter 4

Local axonal morphology guides the topography of interneuron myelination in mouse and human neocortex

J. Stedehouder[1] , D. Brizee[1] , J. A. Slotman[2] , M. Pascual-García[1] ,
M. L. Leyrer[3] , B. L. Bouwen[4 5] , C. M. Dirven[5] , Z. Gao[4] ,
D. M. Berson[3] , A. B. Houtsmuller[2] , S. A. Kushner[1]

[1] Department of Psychiatry, Erasmus MC University Medical Center, Rotterdam, Netherlands.
[2] Erasmus Optical Imaging Center, Department of Pathology, Erasmus MC University Medical Center, Rotterdam, Netherlands.
[3] Department of Neuroscience, Brown University, Providence, United States.
[4] Department of Neuroscience, Erasmus MC University Medical Center, Rotterdam, Netherlands.
[5] Department of Neurosurgery, Erasmus MC University Medical Center, Rotterdam, Netherlands.

Abstract

GABAergic fast-spiking parvalbumin-positive (PV) interneurons are frequently myelinated in the cerebral cortex. However, the factors governing the topography of cortical interneuron myelination remain incompletely understood. Here, we report that segmental myelination along neocortical interneuron axons is strongly predicted by the joint combination of interbranch distance and local axon caliber. Enlargement of PV+ interneurons increased axonal myelination, while reduced cell size led to decreased myelination. Next, we considered regular-spiking SOM+ cells, which normally have relatively shorter interbranch distances and thinner axon diameters than PV+ cells, and are rarely myelinated. Consistent with the importance of axonal morphology for guiding interneuron myelination, enlargement of SOM+ cell size dramatically increased the frequency of myelinated axonal segments. Lastly, we confirm that these findings also extend to human neocortex by quantifying interneuron axonal myelination from ex vivo surgical tissue. Together, these findings establish a predictive model of neocortical GABAergic interneuron myelination determined by local axonal morphology.

Introduction

Myelination is the insulating ensheathment of axons by oligodendrocytes to enhance action potential propagation and provide metabolic support[1]. Recent studies have shown that a large fraction of neocortical myelination arises from axons of fast-spiking, parvalbumin-positive (PV) interneurons[2,3]. Nearly every cortical PV+ interneuron is myelinated, and most frequently with a proximally-biased axonal topography consisting of short internodes interspersed with branch points[3,4]. In contrast, other neocortical GABAergic interneuron subtypes are more rarely and sparsely myelinated, raising the question of what factors determine this cell type-restricted pattern of neocortical interneuron myelination.

Axonal diameter has been previously demonstrated as an important neuronal factor influencing myelination. In the peripheral nervous system (PNS), a critical threshold of axonal diameter of ~1 μm has been identified, which largely predicts myelination[5]. However, in the central nervous system (CNS), the pattern is much less clear. Axons with diameters ~200 nm can become myelinated[6], while axon diameters as large as ~800 nm can remain unmyelinated[6]. In vitro, oligodendrocytes reliably initiate myelination of synthetic nanofibers above a critical diameter of ~300 nm but rarely do so for smaller diameters[7-9]. The diameter findings appear to extend to grey matter in vivo, where myelinated axons <300 nm are rarely observed[2,9]. Moreover, following acute demyelination regenerated myelin sheaths often re-establish their pre-morbid pattern of myelination, suggesting that intrinsic axonal factors are primary determinants of myelination[10]. Furthermore, oligodendrocytes appear to sense axonal diameters in vitro, and adjust their internode length based on fiber diameter[8]. Taken together, axonal diameter is firmly established as an important determinant underlying internode formation. However, in contrast to its high predictive validity in the PNS, axonal diameter is only moderately predictive of myelination topography in the CNS.

Here we examine the relationship between cortical interneuron myelination and axonal morphology in adult mouse prefrontal cortex. We find that the topography of myelination along individual PV+ axons is strongly predicted by the joint combination of axonal diameter and interbranch distance. The bivariate model combining axonal diameter and interbranch distance was superior to univariate models involving either axonal diameter or interbranch distance alone. We further explored the model robustness by implementing bidirectional manipulations of PV+ interneuron size. Enlargement of PV+ interneuron size resulting from cell-type specific deletion of *Tsc1* increased the incidence of myelinated segments. Conversely, reduction of PV+ interneuron size by cell-type specific deletion of *Ube3a* decreased the frequency of

myelinated segments. Yet notably, in both cases, the joint combination of interbranch distance and local axon caliber remained highly predictive of myelin topography. Lastly, we considered regular-spiking SOM+ cells, which normally have relatively shorter interbranch distances and thinner axon diameters than PV+ cells, and are rarely myelinated. However, enlargement of SOM+ cell size by cell type-specific deletion of *Tsc1* dramatically increased the frequency of myelinated axonal segments and with a topography accurately predicted by the bivariate model. Lastly, we find that interneurons reconstructed from human ex vivo surgical tissue also exhibit similar rules governing their axonal myelination. Together, these results establish a highly predictive model of neocortical GABAergic interneuron myelination topography based on local axonal morphology.

Results

Super-resolution imaging of individual fast-spiking, PV+ interneuron axons

To examine the relationship between the axonal morphology of PV+ interneurons and their myelination, we targeted fluorescent PV+ interneurons in the adult medial prefrontal cortex (mPFC) of *Pvalb*::cre[11],Ai14[12] mice for whole-cell patch-clamp recording and biocytin filling (n = 8 cells; **Figure 1a, b; Supplementary file 1**). Recorded cells exhibited the fast-spiking pattern associated with PV+ interneurons (**Figure 1c**). Biocytin-labeled cells were imaged by confocal microscopy for reconstruction (**Figure 1d**), followed by structured illumination microscopy (SIM) for high-resolution analysis of individual axonal segments[13] (see Materials and methods; **Figure 1 – Figure supplements 1-3**). We systematically analyzed PV+ interneuron axonal segments up to the 7th branch order, beyond which myelination was rarely observed in this region[3,4]. Axon shaft diameter averaged 0.34 ± 0.01 μm (range 0.16–0.98 μm) and decreased with increasing branch order (**Figure 1e-g**). *En passant* boutons, located primarily on more distal branches (≥5th branch order), averaged 0.71 ± 0.01 μm in diameter (range 0.34–1.26 μm; **Figure 1h**).

PV+ interneuron myelination co-varies with axon morphology

Myelin was visualized by immunolabeling for myelin basic protein (MBP). Consistent with previous studies[3,4], reconstructed PV+ interneurons consistently exhibited myelination of their proximal axons (8 out of 8; 100%, **Figure 2a, c**), while distal axonal segments remained unmyelinated (**Figure 2b, c**). Myelination of PV+ interneurons typically extended from branch point to branch point (**Figure 2c**), in which ~84% of myelinated internodes had their boundaries within 5 μm of an axonal branch point
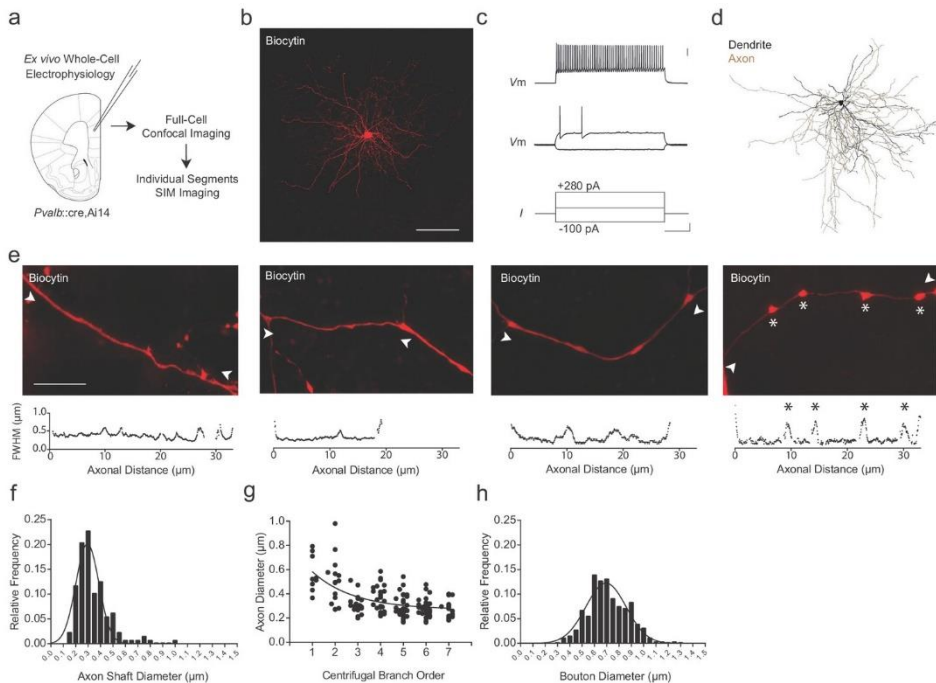
Figure 1. Super-resolution microscopy of fast-spiking, PV+ interneuron axons. a) Experimental approach. Biocytin-filled fast-spiking PV+ interneurons from mPFC were analyzed using both confocal imaging and structured illumination microscopy (SIM) imaging. See also **Figure 1 – Figure supplements 1-3**.**b**) Maximum projection confocal image of a representative biocytin-filled PV+ cell from mPFC layer V (red). Scale bar, 50 μm. **c**) Current clamp recording of evoked action potentials. Scale bars are 20 mV, 100 pA and 100 ms from top to bottom (right). **d**) Full reconstruction of a mPFC layer V PV+ interneuron. Soma and dendrites in black, axon in brown. **e**) Representative SIM *z*-stack projections of PV+ interneuron axonal segments (top), along with their corresponding FWHM diameter profiles (bottom). White arrowheads indicate measurement boundaries. From left to right: First branch order axon initial segment; second branch order unmyelinated axonal segment; third branch order myelinated axonal segment; sixth branch order unmyelinated axonal segment featuring multiple *en-passant* boutons (indicated by asterisks). Scale bar, 10 μm. **f**) Distribution histogram of PV+ interneuron axon shaft diameters, fitted with a Gaussian curve. $n = 140$ axonal segments/8 cells. **g**) Average axon shaft diameter decreases steadily over centrifugal branch order. $n = 140$ segments/8 cells. $p < 0.001$, one-way ANOVA. **h**) Distribution of axonal *en passant* bouton diameters of PV+ interneuron axons, fitted with a Gaussian curve. $n = 250$ boutons/8 cells. Abbreviations: FWHM, full-width half-maximum. I, input current. SIM, structured illumination microscopy. Vm, membrane voltage.

(**Figure 2d**). For each reconstructed interbranch segment, we examined the relationship between the probability of segmental myelination and the average axon shaft diameter using receiver operating characteristic (ROC) analysis[14]. Axon shaft diameter strongly co-varied with myelination, with a critical univariate threshold at 334

nm (area under curve, AUC = 0.93; sensitivity = 97.2%, specificity = 84.4%), above which internodes were often present and below which myelination was rarely observed (**Figure 2e-g**). However, 30% of interbranch segments with axon shaft diameter >334 nm remained incorrectly classified by the univariate ROC model (15 of 50 segments), suggesting additional deterministic factors underlying the variance in segmental myelination.

We next considered the univariate relationship of interbranch distance with segmental myelination. We found that myelination occurred more frequently along uninterrupted interbranch segments greater than 17.4 µm (AUC = 0.79; sensitivity = 97.2%, specificity = 60.4%; **Figure 2f, g**). However, similar to the relationship with axonal diameter, a substantial proportion of interbranch segments >17.4 µm were unmyelinated (48%, 35 of 73 segments).

Therefore, we implemented a bivariate ROC analysis[15] to explore whether the intersection of interbranch distance and axonal diameter might yield improved estimates of segmental myelination. Using a bivariate ROC analysis, the optimal interbranch distance and axonal diameter were 13.7 µm and 334 nm, respectively (AUC = 0.99; **Figure 2f, g**). The joint combination of these two thresholds correctly predicted whether 128 of 132 segments contained an internode (97.0% accuracy), a significant improvement over the univariate models (interbranch distance: 70.5% accuracy, Fisher's Exact Test p<0.001; axonal diameter: 87.9% accuracy, Fisher's Exact Test p=0.005). In particular, the bivariate model correctly predicted 35 of 36 myelinated internodes (sensitivity = 97.2%), matching that of the univariate predictors (Fisher's Exact Test p=0.99). However, the joint combination of interbranch distance and axonal diameter also predicted with high accuracy those segments in which myelination was absent (93 of 96 segments, specificity = 96.9%), in contrast to the univariate models
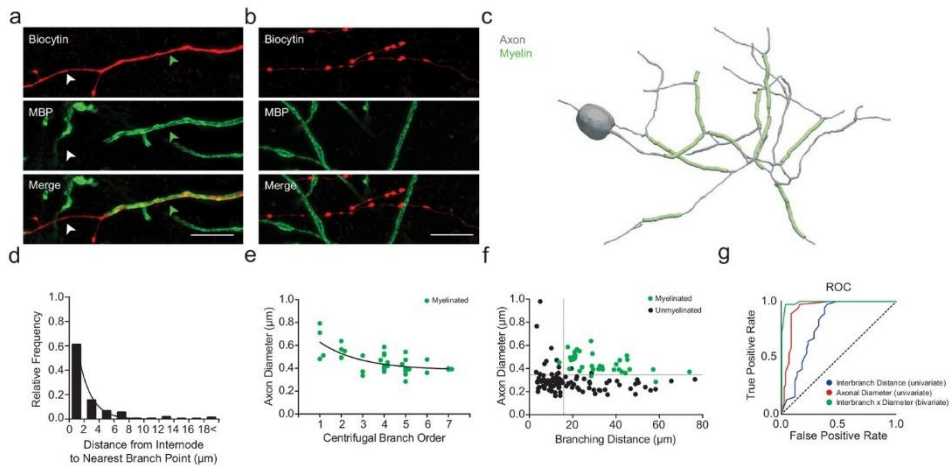
Figure 2. PV+ interneuron axon diameter co-varies with myelination. a) Average SIM *z*-stack projection of a biocytin-filled PV+ interneuron axon (red) along with its myelination (MBP; green arrowhead), centered over a fourth branch order segment. Note that the relatively thinner axonal segment is unmyelinated (white arrowhead). Scale bar, 5 µm. **b**) Average SIM *z*-stack projection of a biocytin-filled PV+ interneuron axon (red) lacking myelination (MBP), centered over a seventh branch order segment. Note the frequent *en passant* boutons and thin axon shaft. (**c**) Neurolucida reconstruction of an mPFC fast-spiking PV+ interneuron axon. Axon in grey, myelinated segments in green. Note the proximal onset of myelin, consisting of short internodes interspersed by branch points. **d**) Frequency histogram of nearest neighbor distance from internodes to branch points. *n* = 81 segments/5 cells. **e**) Average axon segment diameter versus branch order, exclusively for segments showing myelination. *n* = 39 segments/8 cells. p<0.001, one-way ANOVA. **f**) The joint combination of axonal diameter and interbranch point distance is highly predictive of segmental myelination. Each circle represents an individual axonal segment. Myelinated segments (green) are consistently thicker and longer compared to unmyelinated segments (black), with critical thresholds (dotted lines) of 13.4 µm and 334 nm for interbranch distance and diameter, respectively. *n* = 140 segments/8 cells. **g**) Receiver-operator characteristic (ROC) curves for interbranch distance (blue) and diameter (red) as univariate predictors, as well as the significantly improved joint bivariate prediction (green) of myelination status (p<0.001). Diagonal dotted line indicates the non-discrimination reference boundary. Abbreviations: ROC, receiver-operator characteristic.

(Fisher's Exact Test; axonal diameter: p=0.004, interbranch distance: p<0.001). These findings suggest that the combination of interbranch distance and axonal diameter are highly predictive of segmental myelination along PV+ interneurons.

To independently corroborate the findings from supra-resolution imaging, we utilized electron microscopy (EM) for assessing the morphology and myelination of PV+ cell axons. We utilized a genetic labeling method to enhance the electron dense contrast of PV+ cell axons by stereotactic injection of a cre-dependent adeno-associated virus (AAV2) into the mPFC of *Pvalb*::cre mice. Virus-transduced *Pvalb*::cre cells expressed the EM marker APEX2[16] fused with membrane-targeted GFP (mGFP-APEX2), permitting cell-type specific visualization of labeled PV+ cells in both fluorescence and electron micrographs (**Figure 3a-c, e, f**). Prior to ultrastructural analysis, we used confocal microscopy to confirm that GFP+ neurons resembled PV+ cells morphologically. We also confirmed that nearly all of the virally labeled cells were immunopositive for PV (93.9 ± 1.3%; **Figure 3b-d**). We then used APEX2-mediated peroxidase histochemistry to produce intracellular electron dense labeling. PV+ cells were readily detected by their darkened cytoplasmic staining in electron micrographs. This allowed us to identify axonal processes belonging to PV+ interneurons, whether myelinated or not (**Figure 3e, f**). The distributions of axon shaft diameter and bouton diameter, and their relationship with axonal branch order, were also highly comparable to previous ultrastructural analyses of fast-spiking, PV+ interneurons[16-18]. Consistent with the fluorescence microscopy analysis (**Figure 2**), myelination was observed exclusively

around PV+ axonal fibers with shaft diameters > 330 nm. Mean diameter was significantly larger in myelinated than in unmyelinated segments (**Figure 3g**). Thus, axon morphology strongly predicts myelination of PV+ interneurons using two independent methods.
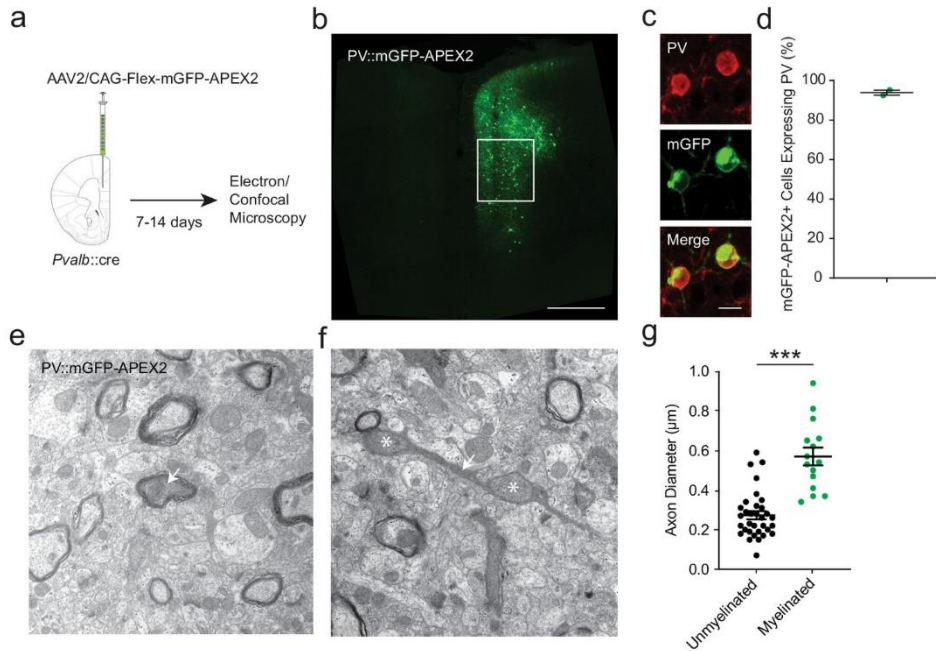

Figure 3. APEX2 contrast-enhanced electron microscopy confirms that smaller-diameter axonal segments lack myelination. a) Experimental flowchart. *Pvalb*::cre mice were given unilateral injections into mPFC with AAV2/CAG-flex-mGFP-APEX2, and sacrificed for confocal and electron microscopy after 7 to 14 days. **b**) Confocal image of unilateral PV-specific mGFP-APEX2 expression in mPFC (green). White square depicts the region of interest in the prelimbic area. **c**) Representative confocal microscopy image of mGFP-APEX2 fluorescence (green) and its colocalization with PV immunofluorescence (red). **d**) Quantification of colocalization between mGFP-APEX2+ cells and PV immunofluorescence. 93.9 ± 1.3% of mGFP-APEX2+ cells expressed PV. $n = 2$ mice **e-f**) Electron microscopy images (14kx) of PV::mGFP-APEX2+ myelinated **e**) and unmyelinated **f**) axons (arrows). Morphological enlargements featuring mitochondria (asterisks) were not included in the diameter analysis. **g**) PV+ interneuron axonal segments featuring myelination have a larger average diameter (green) than unmyelinated axons (black). Unmyelinated: 0.269 ± 0.019 µm, $n = 38$; myelinated: 0.570 ± 0.045 µm, $n = 15$. ***$p<0.001$. Unpaired two-tailed Student's *t*-test. Black bars represent mean ± s.e.m.

Bi-directional manipulation of PV+ axon morphology alters myelination

In order to examine the robustness of axonal morphology in predicting PV+ interneuron myelination topography, we performed cell-type specific manipulations known to

influence axonal geometry. Deletion of the *Tsc1* gene has been previously shown to induce enlarged somata of various neuronal cell types across a diversity of brain regions[19-22]. Moreover, the Akt-mTOR pathway, a downstream target of *Tsc1*, is one of the main regulators of axon caliber[23]. Conversely, mice harboring a deletion of *Ube3a* have recently been shown to exhibit smaller neurons[24,25] with reduced axonal diameters in corpus callosum[26].

To obtain PV cell-specific deletions, *Pvalb*::cre mice were crossed with floxed *Tsc1^{f/f}* mice (PV::TSC1) and floxed *Ube3a^{p/f}* mice (PV::UBE3A) (**Figure 4a; Figure 4 – Figure supplements 1-2**). PV+ cells in adult mPFC of PV::TSC1 mice exhibited a ~50% increase in soma size, in accordance with a strong upregulation of pS6$^{235/236}$, a downstream target of mTOR (**Figure** 4b,c). PV::TSC1 cells showed filopodia-like extensions on their soma and proximal dendrite, which were not observed in PV::WT cells (**Figure 4 – Figure supplement 1f**). Conversely, PV::UBE3A mice exhibited a ~15% reduction in PV+ interneuron soma area (**Figure 4b, c**). Notably, mPFC PV cell density was similar across PV::UBE3A, PV::TSC1, and PV::WT mice (**Figure 4 – Figure supplement 3a-b**).
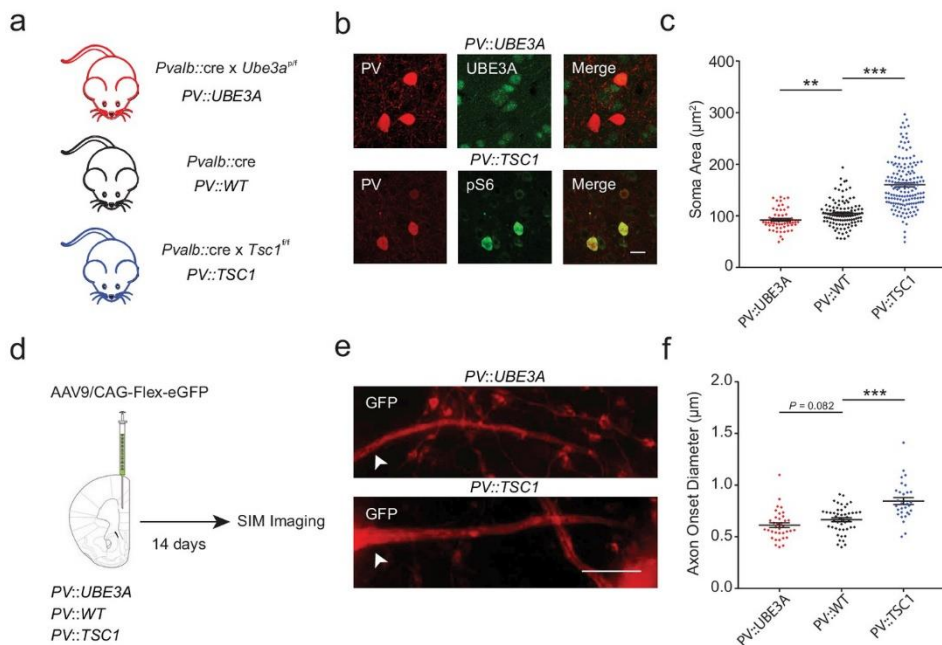
Figure 4. PV::TSC1 and PV::UBE3A mice exhibit reciprocal alterations of PV+ cell morphology. a) Overview of mouse breeding scheme. **b**) Maximum projection confocal image of PV+ somata (red) in PV::UBE3A mice lacking UBE3A (green; top), and in PV::TSC1 mice showing high pS6 expression (green, bottom). Higher magnification images are provided in Figure 4–figure

supplements 1–2. Scale bar, 15 μm. (**c**) Quantification of PV+ interneuron maximum projection soma area from mPFC layers II-V. PV::UBE3A: 92.1 ± 2.7 μm^2; *n* = 58 cells; PV::WT: 104.6 ± 2.5 μm^2; *n* = 109 cells PV::TSC1: 160.2 ± 3.8 μm^2; *n* = 159 cells; *n* = 3 mice per group. **d**) Experimental procedure. PV::UBE3A, PV::WT and PV::UBE3A were stereotactically injected with AAV9/CAG-Flex-eGFP in the mPFC and analyzed two weeks later with SIM imaging. **e**) Representative projection of a SIM *z*-stack showing primary axon branches (red) originating from transfected GFP+ somata in PV::UBE3A and PV::TSC1 mice. White arrowhead indicates location of axon onset. Scale bar, 2 μm. **f**) PV+ interneuron axon caliber quantifications from mPFC layers II-V. PV::UBE3A: 0.613 ± 0.023 μm; *n* = 36 axons; PV::WT: 0.665 ± 0.019 μm; *n* = 46 axons; PV::TSC1: pS6+ 0.846 ± 0.034 μm; *n* = 30 axons*; n* = 3 mice per group. ***p<0.001; **p<0.01; *p<0.05. One-way ANOVA followed by *post hoc* Tukey's test. Black bars represent mean ± s.e.m.

To examine axon caliber, adult PV::TSC1, PV::UBE3A and PV::WT mice received unilateral stereotactic injections in the mPFC of adeno-associated virus (AAV) containing cre-dependent GFP. Fourteen days later, mice were sacrificed and axons originating from GFP+ somata were imaged using SIM **(Figure 4d)**. Since we observed that the diameter of the 1st branch order strongly correlated to diameter of consecutive axonal segments (**Figure 1**), we measured primary axonal diameter at the 1st branch order for GFP-labelled cells from PV::TSC1, PV::UBE3A and PV::WT cells as a high-throughput indication of axon caliber. Consistent with enlarged somata, this analysis revealed a significantly increased primary axonal caliber of PV::TSC1 PV+ cells compared to PV::WT cells (**Figure 4e, f**). In contrast, axons from PV::UBE3A showed a non-significant trend toward decreased primary axon caliber compared to PV::WT cells (**Figure 4e, f**).

We next performed whole-cell electrophysiological recordings of adult mPFC PV+ cells combined with biocytin-filling and *post hoc* MBP immunofluorescence as previously described (**Figure 5a; Figure 4 – Figure supplement 4**)[3,4]. Recorded PV+ cells in PV::TSC1, PV::UBE3A and PV::WT exhibited fast-spiking firing characteristics, with no detectable differences between genotypes (**Figure 5b – d; Figure 4 – Figure supplement 4**). Confocal imaging followed by proximal axonal reconstructions (**Figure 5e–h**) revealed that all PV::TSC1 cells exhibited axonal myelination (13 of 13 cells; 100%; **Figure 5f-i**), similar to PV::WT cells (10 of 11 cells; 90%) and PV::UBE3A cells (7 of 8 cells; 88%). *Tsc1*-deficient PV+ cells showed increased axonal myelination per cell compared to PV::WT cells (**Figure 5j**). Interestingly, the increase in myelination per cell was associated with both an increase of average internode length (**Figure 5k**) as well as a higher number of internodes per cell (**Figure 5l**), but without a change of interbranch distance (**Figure 5m**). Onset of myelination, measured as axonal distance from the soma or originating dendrite to the beginning of the first internode, was unchanged (**Figure 5n**). In contrast to PV::TSC1 cells, *Ube3a*-deficient PV+ cells exhibited a

decrease in axonal myelination (**Figure** 5i,j), including both a lower number and shorter length of internodes (**Figure 5k, l**), consistent with their reduced soma size. Finally, the initial point of myelin onset from the soma was unchanged in PV::UBE3A cells (**Figure 5n**). Despite these PV+ cell type-specific alterations in myelination, no robust changes were observed in global myelination (**Figure 5 – Figure supplement 1a, b**) or CC1+ mature oligodendrocyte density (**Figure 5 – Figure supplement 1c, d**).
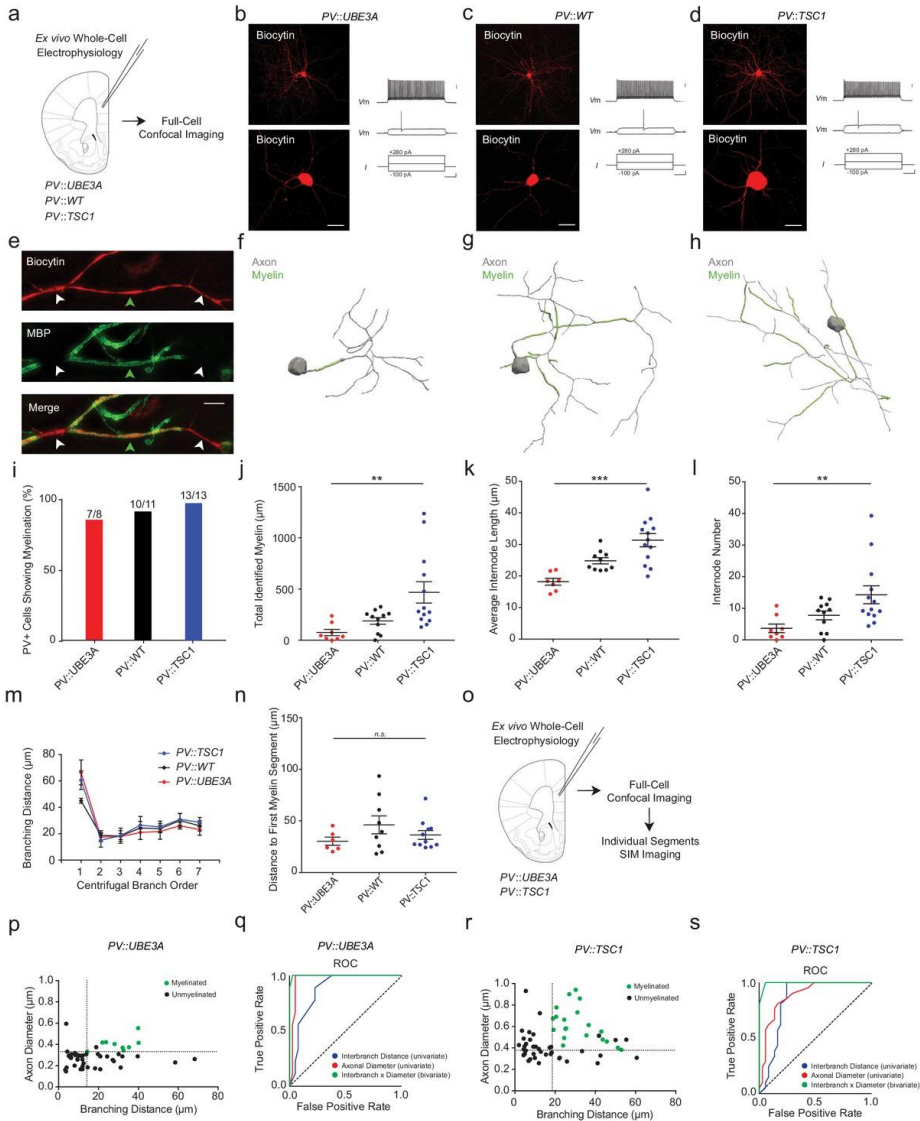
Figure 5. PV::UBE3A and PV::TSC1 mice exhibit bi-directional alterations in PV+ interneuron axonal myelination. a) Experimental approach. Biocytin-filled fast-spiking PV+ interneurons from each genotype were first analyzed using confocal imaging. **b–d**) Maximum projection image of a representative biocytin-filled PV+ cell (red, top), a close-up of a biocytin-filled somata (red, bottom), with a corresponding fast-spiking action potential train for PV::UBE3A **b**), PV::WT **c**), and PV::TSC1 **d**). Scale bars are 50 μm (left) and 20 mV, 100 pA and 100 ms from top to bottom (right). **e**) Representative SIM *z*-stack projection of a biocytin-filled PV+ interneuron axon centered over a 4th order branch (red), demonstrating myelinated (MBP, green; green arrowhead) and unmyelinated segments (white arrowhead). Scale bar, 5 μm. **f–h**) Proximal axon reconstructions (grey) including myelinated segments (green) of representative cells from PV::UBE3A **f**), PV::WT **g**), and PV::TSC1 **h**) mice. **i**) Nearly all PV+ cells exhibit axonal myelination, independent of genotype. **j–l**) PV+ cell-specific genetic manipulations bi-directionally alter myelin content **j**), internode length **k**) and number of internodes per cell **l**). **m**) The distribution of interbranch distance remains similar across genotypes (p=0.575, repeated measures ANOVA group x branch order interaction). **n**) Distance from the soma to the onset of myelination was unaffected by PV+ cell-specific deletion of *Ube3a* or *Tsc1*. p=0.589, one-way ANOVA. **o**) Experimental approach. Biocytin-filled fast-spiking PV+ interneurons from PV::UBE3A and PV::TSC1 mice were analyzed using both confocal and SIM imaging. **p**) The joint combination of axonal diameter and interbranch point distance is highly predictive of PV::UBE3A cell segmental myelination. Critical thresholds (dotted lines) for interbranch distance and axonal diameter were 14.1 μm and 332 nm, respectively. *n* = 49 segments/3 cells. Myelinated segments, green circles. Unmyelinated segments, black circles. **q**) Receiver-operator characteristic (ROC) curve for PV::UBE3A cells. ROC curves of segmental myelination, comparing univariate models of interbranch distance (blue) and axonal diameter (red), and their joint bivariate combination (green). Diagonal dotted line indicates the non-discrimination reference boundary. (**r**) The joint combination of axonal diameter and interbranch point distance is highly predictive of PV::TSC1 cell segmental myelination. Critical thresholds (dotted lines) for interbranch distance and axonal diameter were 18.6 μm and 378 nm, respectively. *n* = 58 segments/3 cells. Myelinated segments, green circles. Unmyelinated segments, black circles. **s**) ROC curves for PV::TSC1 cells. ROC curves of segmental myelination, comparing univariate models of interbranch distance (blue) and axonal diameter (red), and their joint bivariate combination (green). Diagonal dotted line indicates the non-discrimination reference boundary. ***p<0.001, **p<0.01, *p<0.05, n.s. non-significant. One-way ANOVA in **j**, **k**, **l** and **n**. Repeated measures ANOVA in **m**. Black bars represent mean ± s.e.m. Abbreviations: I, input current. ROC, receiver-operator characteristic. Vm, membrane voltage.

Systematic analysis of individual PV+ interneuron axonal segments in PV::UBE3A and PV::TSC1 cells confirmed a similarly strong co-variation between axon morphology and segmental myelination as observed in PV::WT mice (**Figure 5o-s**). ROC analysis of PV::UBE3A cells yielded bivariate thresholds of axonal diameter >332 nm and interbranch distance >14.1 μm (sensitivity = 100%, specificity = 97.5%; AUC = 0.99) (**Figure 5p, q**). Analogously, ROC analysis of the PV::TSC1 cells yielded bivariate thresholds of axonal diameter >378 nm and interbranch distance >18.6 μm (sensitivity = 100%, specificity = 94.6%; AUC = 0.99) (**Figure 5r, s**). Similar to PV::WT, the bivariate model for PV::TSC1 significantly improved the prediction accuracy of

segmental myelination compared to the univariate models (axonal diameter: p=0.015; interbranch distance: p=0.027). For PV::UBE3A, the bivariate model was a significant improvement over the univariate model based on interbranch distance (p=0.004), but statistically similar to the univariate model for axonal diameter (p=0.500). Together, these findings demonstrate the robustness of the joint combination of interbranch distance and axonal diameter for accurately predicting the topography of PV+ interneuron myelination in vivo, across a wide range of axonal morphologies.

SOM+ and PV+ interneurons adhere to similar myelination rules

Regular spiking, SOM+ interneurons[27] have relatively few myelinated internodes along their axons in mPFC[3] and contribute minimally to total neocortical myelination content[2]. Is this sparse myelination also predicted by their axonal morphology, as we observed for PV+ interneurons? Do SOM+ interneuron axons share the thinner shaft diameters or more closely spaced branch points of unmyelinated segments of PV+ axons?

To examine this possibility, we performed whole-cell recordings and intracellular biocytin-labeling of SOM+ interneurons in mPFC using *Sst*::cre[28],Ai14[12] mice (*n* = 10; **Figure 6a-d**; **Figure 1 – Figure supplement 3**). The identity of filled cells was further confirmed as SOM+ interneurons based upon their characteristic electrophysiological and morphological features[27] (**Figure 6c, d**; **Supplementary file 2**; **Figure 7 – Figure supplement 1e**). Among the 10 reconstructed SOM+ axons, we found only a single myelinated internode (**Figure 6e- h**). Axonal shaft diameter as quantified using SIM averaged 0.303 ± 0.015 μm (range 0.222–0.561 μm; **Figure 6f**, **Figure 7 – Figure supplement 1f**) and decreased with increasing branch order (**Figure 6g**). Notably, the vast majority of unmyelinated SOM+ axonal segments had smaller diameters and/or more closely spaced branch points than the threshold values identified among myelinated segments in PV+ interneurons (**Figure** 6h inset; dashed line).

Since we identified only a single myelinated segment, we could not reliably determine critical thresholds for axonal diameter and interbranch distance thresholds among wild-type SOM+ interneurons. Notably, however, this single myelinated segment had an axonal diameter of 561 nm and interbranch distance of 16.8 μm, which exceeded the morphometric thresholds we identified for wildtype PV+ interneurons. Similarly, the vast majority of unmyelinated SOM+ interneuron axon segments fell below morphometric thresholds for axonal diameter and/or interbranch distance identified for PV::WT cells (79 of 88 segments; 89.8%) (**Figure 6h**). These data indicate that the myelination rules derived from the analysis of PV+ cells may be generalizable to other neocortical interneurons, including SOM+ cells.
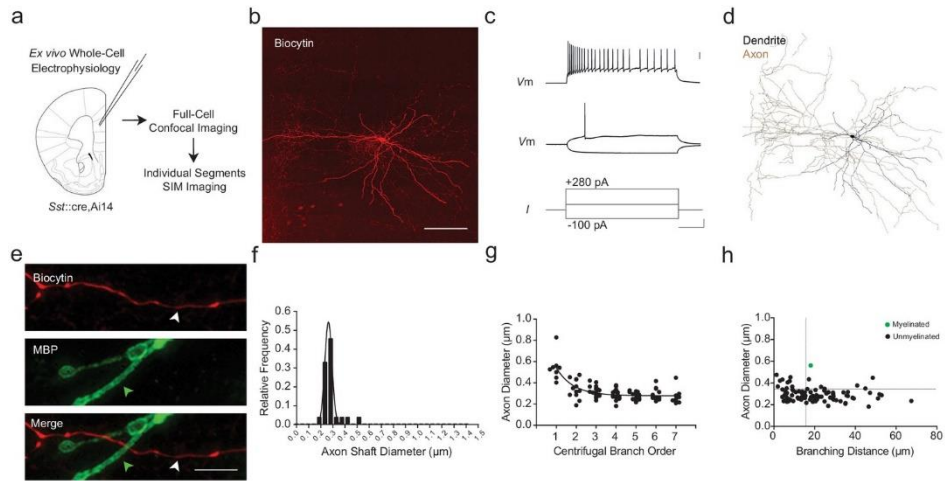
Figure 6. mPFC SOM+ interneurons have subthreshold axonal morphology and are correspondingly unmyelinated. a) Experimental approach. Biocytin-filled regular-spiking SOM+ interneurons from mPFC were analyzed using both confocal imaging and SIM imaging. See also **Figure 1–figure supplements 1-3**. **b**) Maximum projection confocal image of a representative biocytin-filled SOM+ interneuron (red). Scale bar, 50 µm. **c**) SOM+ interneuron recording demonstrating a low threshold for AP initiation, spike frequency adaptation, and AP amplitude attenuation. Scale bars are 20 mV, 100 pA and 100 ms from top to bottom. **d**) Neurolucida reconstruction of the SOM+ cell depicted in **b**). Soma and dendrite in black, axon in brown. Note the tortuous axonal arbor and dendrites. **e**) mPFC SOM+ interneurons are rarely myelinated. Representative confocal image of a SOM+ interneuron axon (red), centered over a 3rd branch order segment (white arrowhead) without myelination (MBP, green; green arrowhead). Scale bar, 10 µm. **f**) Frequency histogram of SOM+ interneuron axon shaft diameter, fitted with a Gaussian curve. n = 88 axonal segments/6 cells. **g**) Axon shaft diameter decreases monotonically with increasing centrifugal branch order. n = 88 segments/6 cells. $p < 0.001$, one-way ANOVA. **h**) Distribution of axonal segment diameter and interbranch distances for myelinated (green circles) and unmyelinated (black circles) segments. n = 88 segments/6 cells. Dotted lines indicate the bivariate thresholds derived from *PV::WT* interneurons. Abbreviations: I, input current. Vm, membrane voltage.

## Genetic manipulation of SOM+ axon morphology induces de novo myelination

Factors other than axon morphology could explain why SOM+ interneurons are largely unmyelinated, such as expression of active inhibitors of myelination[29] (Redmond et al., 2016). We therefore asked whether we could induce de novo myelination of SOM+ cells by altering their axonal morphology. Using an analogous approach to that we used for PV+ cells, we deleted *Tsc1* specifically in SOM+ cells by crossing *Sst*::cre and floxed *Tsc1^{f/f}* mice. SOM+ interneurons identified by *post hoc* immunolabeling had ~65% larger soma size in mPFC compared to WT mice (**Figure 7a, b**; **Figure 7 –**

Figure supplement 1). Moreover, cre-dependent viral labeling of SOM+ cells followed by SIM imaging showed increased axon calibers for SOM::TSC1 cells (1st order branches) compared to WT mice (**Figure 7c, d**). SOM+ cell density was unchanged in the mPFC of SOM::TSC1 mice (**Figure 7 – Figure supplement 2a, b**).

We next performed whole-cell electrophysiological recordings in mPFC SOM+ cells combined with biocytin-filling and *post hoc* MBP immunofluorescence to examine the influence of the enlarged morphology on axonal myelination (**Figure 7e, f**; **Figure 1 – Figure supplement 3**; **Figure 7 – Figure supplement 1**). Recorded SOM::TSC1 cells exhibited reduced input resistance and intrinsic excitability, with no changes in single action potential characteristics (**Figure 7 – Figure supplement 3**).

Confocal microscopy followed by axonal reconstruction showed that whereas SOM::WT cells were rarely myelinated (0 out of 6; 0%), which is in line with the *Sst*::cre,Ai14 cells, myelination of SOM::TSC1 cells was highly frequent (11 out of 11; 100%; **Figure 7f – h**). Moreover, SOM::TSC1 cells showed corresponding increases in total length of myelination (**Figure 7i**), internode length (**Figure 7k**), and number of internodes (**Figure 7j**). Myelin onset appeared at 55.8 ± 7.2 µm from the soma (**Figure 7n**), typically initiating between the 2nd and 6th branch order. No myelin was identified on more distal axonal segments (branch order ≥10). Myelination was found equally on the primary axon and on axon collateral branches (**Figure 7l**). Furthermore, SOM::TSC1 myelination was constrained by axonal branch points, in that 87% of internodes began or ended within 5 µm of a branch point (**Figure 7m**).

Analyses of individual axonal segments using SIM along SOM::TSC1 cells revealed a similar relationship between myelination and the joint combination of axonal diameter and interbranch distance (**Figure 7o-q**) as found in wildtype PV+ cells (**Figure 2f**, **Figure 5n, o**). ROC analysis of SOM::TSC1 cells yielded thresholds of axonal diameter >406 nm and interbranch distance >11.8 µm (sensitivity = 0.95, specificity = 0.90; AUC = 0.94) (**Figure 7p**). The bivariate model exhibited a significantly improved the prediction accuracy for segmental myelination compared to the univariate models (axonal diameter: $p<0.001$, interbranch distance: $p<0.001$). These findings suggest that axonal morphology, and in particular the combination of axonal caliber and interbranch distance, governs the local segmental myelination of PV+ and SOM+ neocortical interneurons.
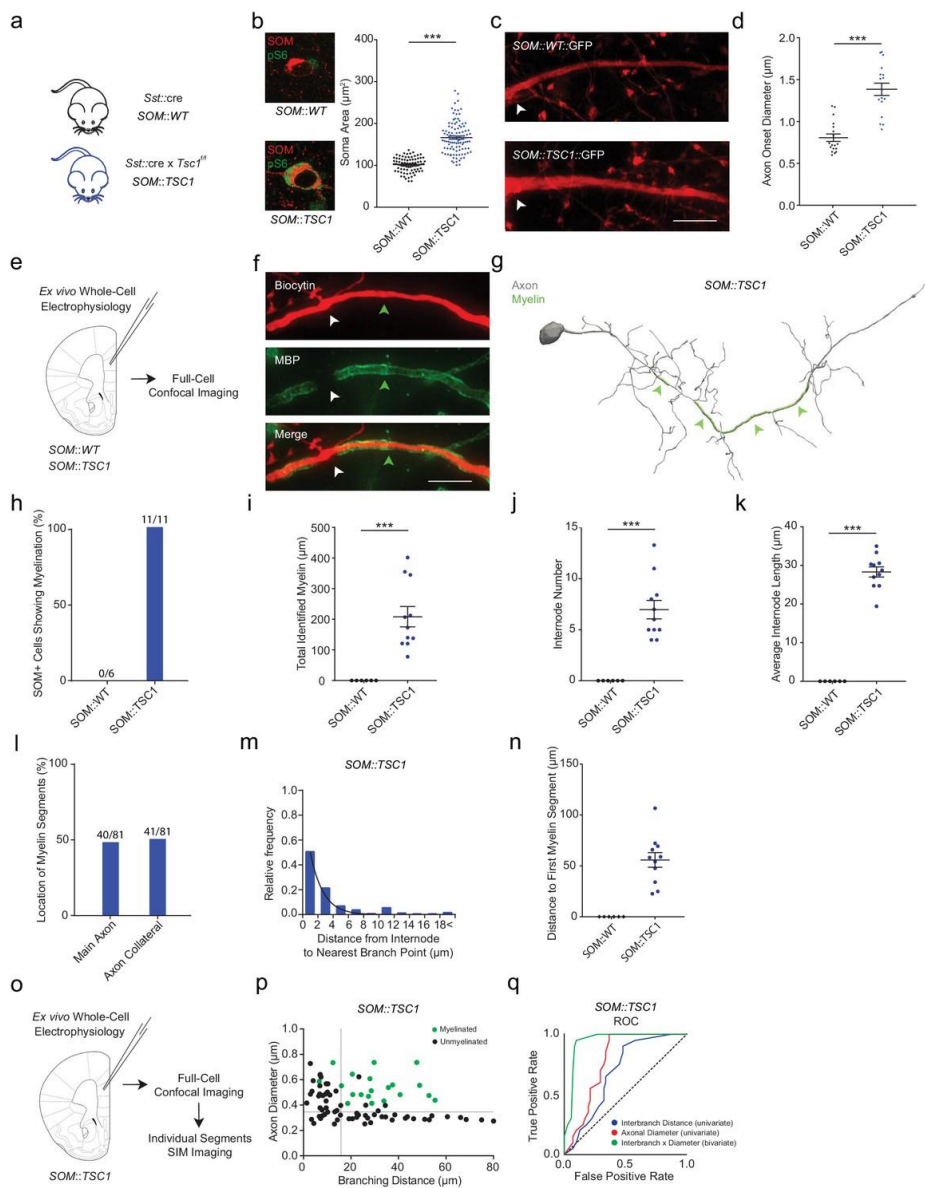
Figure 7. SOM::TSC1 cells are frequently myelinated. a) Overview of mouse breeding scheme. **b**) SOM::TSC1 cells have enlarged somata. Left: Representative confocal images of SOM+ cells (red) confirm the increased expression of pS6 (green) in SOM::TSC1 cells. Higher magnification images in **Figure 7–figure supplement 1**. Right: SOM+ interneuron maximum projection soma area from mPFC layers II-V. SOM::WT: 101.8 ± 1.9 µm^2, $n = 81$ cells; SOM::TSC1: 166.4 ± 3.7 µm^2, $n = 103$ cells; $n = 3$ mice per group. ***$p<0.001$. Unpaired two-tailed Mann-Whitney U-test. **c**) Representative SIM z-stack projection images of GFP-labelled SOM+ interneuron axons (red). SOM::WT (top), SOM::TSC1 (bottom). Scale bar, 3 µm. **d**). SOM::TSC1 cells have an increased

axonal diameter. SOM::WT: 0.799 ± 0.049 µm, n = 18 cells; SOM::TSC1: 1.407 ± 0.076 µm, n = 17 cells; n = 3 mice per group. ***p<0.001. Unpaired two-tailed Mann-Whitney U-test. **e**) Experimental approach. Biocytin-filled regular-spiking SOM+ interneurons from mPFC of SOM::WT and SOM::TSC1 mice were analyzed using confocal imaging **f**) Representative confocal z-stack projection image of a biocytin-filled SOM::TSC1 interneuron axon (red) and myelination (MBP), centered over a 7th branch order segment. Unmyelinated branch point indicated by white arrowhead. Scale bar = 10 µm. **g**) Neurolucida reconstruction of an mPFC SOM::TSC1 cell. The axon (grey) shows multiple myelinated internodes (green) along the main branch. Note the frequent thin, tortuous, and unmyelinated axon collaterals. **h**) In contrast to SOM::WT cells, all 11 reconstructed SOM::TSC1 cells were myelinated. **i–k**) SOM::TSC1 cells exhibit a robust **i**) total myelin (208.30 ± 33.14 µm), **j**) number of internodes (6.97 ± 0.90 µm), and **k**) internode length (28.33 ± 1.31 µm). ***p<0.001, Unpaired Student's two-tailed t-test. SOM::WT: n = 6; SOM::TSC1: n = 11. **l**) Myelin segments occur with similar frequency on main SOM::TSC1 axon branches and axon collaterals (p=0.99, Fisher's Exact Test). **m**) Frequency histogram of nearest neighbor distance from internodes to branch points. n = 38 segments/4 cells. **n**) Distance from the soma or originating dendrite to the onset of myelination was measurable only for SOM::TSC1 cells due to the very infrequent myelination of SOM::WT cells. **o**) Experimental approach. Biocytin-filled regular-spiking SOM+ interneurons from SOM::TSC1 mice were analyzed using confocal and SIM imaging. **p**) The joint combination of axonal diameter and interbranch point distance is highly predictive of PV::TSC1 cell segmental myelination. Critical thresholds (dotted lines) for interbranch distance and axonal diameter were 11.8 µm and 406 nm, respectively. n = 86 segments/5 cells. Myelinated segments, green circles. Unmyelinated segments, black circles. **q**) ROC curves for SOM::TSC1 cells. ROC curves of segmental myelination, comparing univariate models of interbranch distance (blue) and axonal diameter (red), and their joint bivariate combination (green). Diagonal dotted line indicates the non-discrimination reference boundary. Unpaired Student's two-tailed t-test in **i**), **j**) and **k**). Unpaired two-tailed Mann-Whitney U-test in **b**) and **d**) owing to non-normality. Black bars represent mean ± s.e.m. Abbreviations: ROC, receiver-operator characteristic.

Neocortical SOM+ interneurons are morphologically and electrophysiologically heterogeneous[30]. Therefore, to further examine the extent of SOM::TSC1 myelination across a wider population of cells, we employed SOM-specific sparse viral transduction using cre-dependent GFP expression in adult mPFC, followed by MBP immunofluorescence (**Figure 8a**). Although this method precludes electrophysiological confirmation of adapting spiking patterns and detailed axonal reconstructions, it provides a higher-throughput examination of mPFC SOM+ interneuron myelination. We examined axons originating from mPFC layer II-V GFP+ interneuron somata from SOM::WT and SOM::TSC1 mice for colocalization with MBP (**Figure 8b**). Of 26 SOM::WT+ cells examined, 4 (15%) were myelinated (**Figure 8c**). Conversely, of 50 SOM::TSC1+ cells examined, 46 (92%) were myelinated (p<0.001; **Figure 8c**). Consistent with the high proportion of SOM+ cell myelination, the mPFC of SOM::TSC1 exhibited a marked increase of global myelination (**Figure 8d, e**) and a higher density of CC1+ mature oligodendrocytes (**Figure 8f, g**).

Together, these data suggest that axonal morphology is necessary and sufficient to govern neocortical interneuron myelination. In particular, we propose that the combination of interbranch distance and axonal diameter together determine the topographical distribution of internodes along the axons of neocortical interneurons.
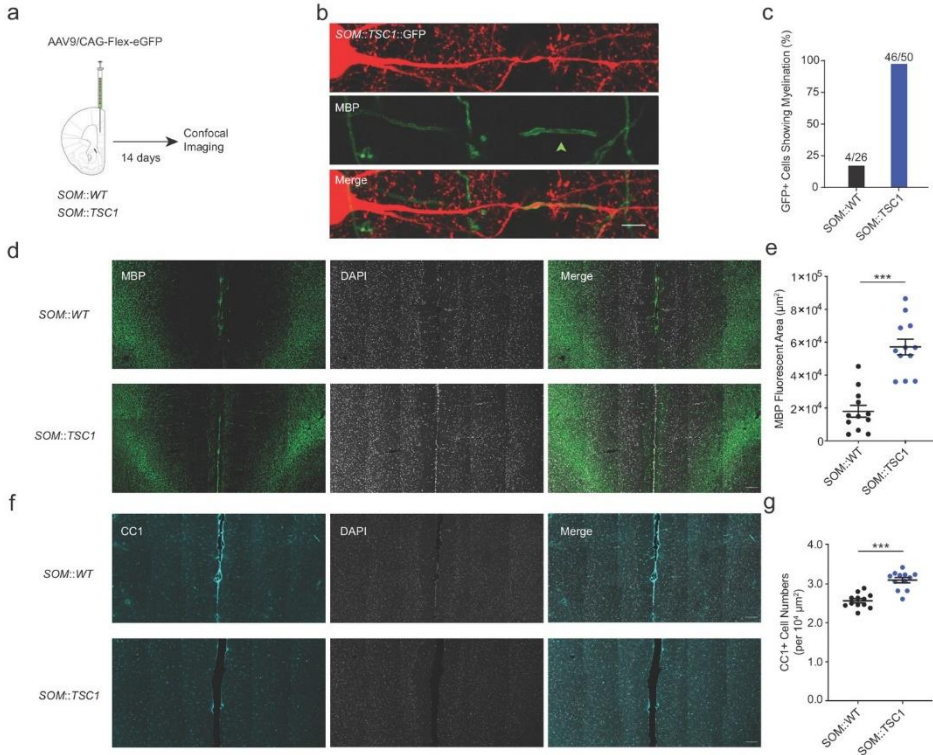

Figure 8. Extensive axonal myelination of SOM::TSC1 cells. a) Experimental flowchart. Adult SOM::WT and SOM::TSC1 mice were injected with low-titer AAV9 cre-dependent GFP reporter virus in mPFC, and sacrificed 14 days later for MBP immunofluorescence labeling and confocal microscopy. **b**) Maximum projection confocal image of a GFP-labelled SOM::TSC1+ interneuron showing circumferential MBP expression (green). Scale bar, 5 μm. **c**) A high proportion of virally-labelled SOM::TSC1 cells exhibited myelination (92.0%, 46 of 50 cells), in contrast to SOM::WT cells (15.4%, 4 of 26 cells) (p<0.001, Fisher's Exact Test). **d**) Representative low-magnification confocal image from mPFC showing the robust increase of myelination (MBP, green) in SOM::TSC1 compared to SOM::WT mice. DAPI in white. Scale bar, 100 μm. **e**) Quantification of MBP+ area in mPFC of SOM::TSC1 mice ($5.7 \times 10^4 \pm 0.48 \times 10^4$ μm^2) compared to SOM::WT mice ($1.8 \times 10^4 \pm 0.36 \times 10^4$ μm^2). p<0.001, Unpaired Student's two-tailed t-test. **f**) Confocal microscopy image showing immunofluorescence of CC1 (cyan) and DAPI (white) in adult mPFC of SOM::WT and SOM::TSC1 mice. Scale bar, 100 μm. **g**) CC1+ cell density in adult mPFC of SOM::TSC1 and SOM::WT mice. p<0.001, Unpaired Student's two-tailed t-test. Black bars indicate mean ± s.e.m.

Human neocortical interneurons adhere to similar myelination rules

We next examined whether the above findings in mice also extend to human neocortex. Using ex vivo resected tissue from patients undergoing tumor surgery, we performed whole-cell electrophysiological recordings (**Supplementary file 3**) and intracellular biocytin labeling with *post hoc* MBP immunofluorescence of fast-spiking interneurons classified on the basis of morphology and electrophysiology (**Figure 9a-e**; 4 cells from four donors; see *Materials and methods*).

Reconstructed human fast-spiking interneurons exhibited a similar total length of myelination (432.0 ± 137.9 µm), average internode length (44.7 ± 4.9 µm), and number of internodes (9.7 ± 1.9 internodes) as previously described[3]. Myelin onset appeared at 36.2 ± 13.3 µm from the soma, initiating between the 1st (2 out of 4 cells; 50%) and 3rd branch order (2 out of 4 cells; 50%). Analogous to mouse interneurons, no myelin was identified on more distal axonal segments (branch order ≥10; **Figure 9f**).
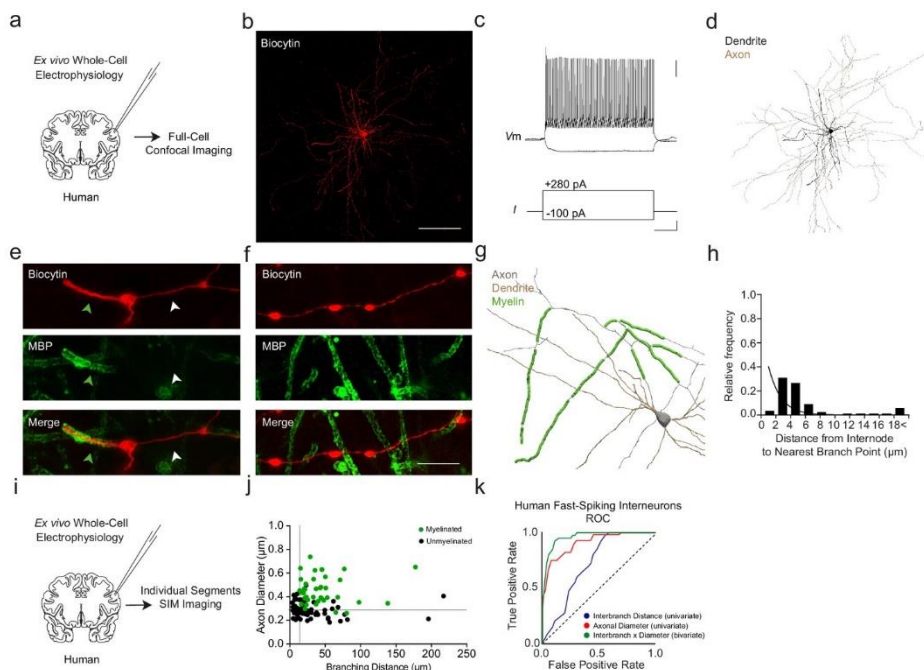
Figure 9. Myelination thresholds extend to fast-spiking interneurons in human cortex. a) Experimental approach. Biocytin-filled interneurons from human ex vivo resected cortical tissue were analyzed using confocal imaging. **b**) Maximum projection confocal image of a representative biocytin-filled human fast-spiking interneuron (red). Scale bar, 50 µm. **c**) Current clamp recording of evoked action potentials of human fast-spiking interneuron. Scale bars are 20 mV, 100 pA and 100 ms from top to bottom (right). **d**) Full reconstruction of a human fast-spiking interneuron. Soma and dendrites in black, axon in brown. **e**) Representative SIM z-stack projection image of a PV+ cell

(biocytin, red), centered over a myelinated (MBP; green) 1st order axonal segment. Note that the myelinated axonal segment (green arrowhead) has a larger diameter than the unmyelinated axon segment (white arrowhead). **f**) Representative SIM *z*-stack projection featuring an unmyelinated segment of axon (red) centered over the 3rd branch order. Scale bar 10 μm for **e**) and **f**). **g**) Neurolucida reconstruction of a human fast-spiking interneuron axon. Axon in grey, myelinated segments in green. Since axon originated from proximal dendrite, dendrite is also depicted in brown. Note the proximal onset of myelin, consisting of short internodes interspersed by branch points. **h**) Frequency histogram of nearest neighbor distance from internodes to branch points. *n* = 55 segments/3 cells. (**i**) Experimental approach. Biocytin-filled interneurons from human ex vivo resected cortical tissue were analyzed using SIM imaging. **j**) The joint combination of axonal diameter and interbranch point distance is highly predictive of human fast-spiking interneuron segmental myelination. Critical thresholds (dotted lines) for interbranch distance and axonal diameter were 13.7 μm and 328 nm, respectively. *n* = 96 segments/4 cells. Myelinated segments, green circles. Unmyelinated segments, black circles. **k**) ROC curves for human fast-spiking interneurons. ROC curves of segmental myelination, comparing univariate models of interbranch distance (blue) and axonal diameter (red), and their joint bivariate combination (green). Diagonal dotted line indicates the non-discrimination reference boundary. Abbreviations: ROC, receiver-operator characteristic. I, input current. Vm, membrane voltage.

Analyses of individual axonal segments using SIM along human fast-spiking interneurons revealed a similar relationship between myelination and the joint combination of axonal diameter and interbranch distance (**Figure 9h – j**) as found in mouse PV+ cells (**Figure 2f**). ROC analysis of human interneurons yielded thresholds of axonal diameter >328 nm and interbranch distance >13.7 μm (sensitivity = 92.5%, specificity = 89.3%; AUC = 0.96; **Figure 9k**). The accuracy of the bivariate model (90.6%, 87 of 96 segments) was significantly higher than interbranch distance (66.7%, $p<0.001$) but non-significantly different from axonal diameter (83.3%, $p=0.198$). Together, these findings suggest that mouse and human neocortical interneurons follow similar morphological rules guiding the topography of axonal myelination.

Discussion

Fast-spiking, PV-positive interneurons are frequently myelinated in the cerebral cortex, and their myelination forms a considerable proportion of cortical myelin[2,3,31]. PV+ myelination exhibits a proximally-biased topography consisting of short internodes interspersed by branch points, whereas more distal axonal segments decorated with frequent *en passant* boutons remain unmyelinated[3,4]. Conversely, other interneuron subclasses, such as irregularly spiking SOM-positive interneurons, are sparsely myelinated and contribute minimally to the total content of neocortical myelin[3]. However, it has remained unknown why PV+ interneurons are preferentially myelinated compared to other neocortical interneuron subtypes. Here, we have provided evidence

suggesting that axonal morphology is a strong determinant of the topography of myelination along individual axons.

Using single-cell axonal reconstructions, we revealed a high co-variation between segmental myelination and the joint combination of interbranch distance (~14 µm) and axonal diameter (~330 nm) thresholds. These parameters were remarkably similar across two interneuron subtypes (PV *vs.* SOM) and independent of genetic manipulation of their morphologies. Moreover, our results appear to provide an explanation for the proximally-biased topography of PV+ interneuron myelination, in which internodes are consistently present at the first axonal branch order with a declining probability at increasing branch orders[3,4]. Given that axonal shaft diameter decreases with increasing branch order (see **Figure 1h**, but also Hu and Jonas, 2014[18]), distal axonal segments would therefore remain unmyelinated by virtue of their thinner axon shafts, despite often retaining supra-threshold interbranch distances. Differences in axon morphology presumably also account, at least in part, for the more robust myelination of neocortical PV+ interneurons relative to other interneuron subtypes[2,3]. However, it remains unknown whether the myelination rules revealed here for interneurons extends to neocortical pyramidal cells, which also exhibit interspersed unmyelinated segments[32]. Prior studies using serial EM have identified a ~ 300 nm threshold of axon diameter for both GABAergic as well as non-GABAergic axons, suggesting the morphological parameters could well extend to excitatory axons[2].

We find here that an uninterrupted interbranch distance of ~14 µm is a strict requirement for segmental myelination in both PV+ and SOM+ interneurons. This threshold approximates the length of the smallest myelinated internodes found on neocortical axons of PV+ interneurons[3] and pyramidal neurons[32], and more generally across unspecified cell types in the cerebral cortex[33]. Notably, pre-myelination nodal clustering – the clustering of voltage-gated sodium channels which later form nodes of Ranvier – exists in similar intervals[34]. One possibility is that ~14 µm is the minimum biophysical length compatible with oligodendrocyte ensheathment.

The functional consequence of cortical interneuron myelination is currently unknown. Fast-spiking PV+ interneurons have demanding metabolic requirements[35]. As myelination has been established to function critically in providing axonal metabolic support[36-38], myelination of PV+ interneurons could function by helping to optimize axonal energy utilization. Moreover, PV+ interneurons coordinate fast synchronizing network activity in the gamma frequency range[39], for which segmental interneuron myelination could enhance synchronized inhibition through local modulation of action potential conduction velocity. This is particularly interesting given recent findings that distance-dependent inhibition functions in regulating gamma synchrony[40].

Only a small fraction of neocortical myelin localizes along the axons of irregular-spiking SOM+ interneurons, even though these cells represent ~30% of interneurons[41]. Accordingly, we found that the limited myelination of SOM+ interneurons was highly consistent with their generally thinner axon diameter and shorter interbranch distances compared to PV+ cells. Enlargement of SOM+ interneurons by cell-type restricted deletion of *Tsc1* led to a dramatic increase in the frequency and extent of axonal myelination. Notably, this de novo myelination of SOM::TSC1 cells was also accurately predicted by the same joint axonal diameter and interbranch distance parameters as identified in PV+ interneurons. However, compared to the PV::TSC1 cell manipulation, SOM::TSC1 mice exhibited a more robust increase of global myelination in the mPFC, which was accompanied by an increased number of CC1+ mature oligodendrocytes. One possibility for this finding is that PV+ cell morphology is already largely optimized for supra-threshold morphology permissive of myelination, in contrast to SOM+ cells which are predominantly unmyelinated under normal conditions and therefore exhibit a greater magnitude increase of myelination when their morphology is enlarged by deletion of *Tsc1*. A second non-mutually exclusive possibility is that SOM::TSC1 deletion results in additional non-cell autonomous effects that enhance global myelination and recruitment of mature oligodendrocytes.

An important outstanding question is whether the axonal morphology rules of PV+ and SST+ interneurons extend to neocortical glutamatergic pyramidal cells[42]. Some evidence exists to suggest that analogous morphological thresholds might also extend to non-GABAergic cells in the neocortex[2,43]. For example, the more frequently myelinated first-order axonal segment of PV+ GABAergic axons has a ~ 2.5 fold larger caliber than glutamatergic pyramidal neurons[44]. However, the highly discontinuous topography of internodes along glutamatergic pyramidal cells also suggests a major influence of factors beyond morphology[32]. One possibility is that myelination of pyramidal neurons involves a combination of attractive and/or repulsive molecular cues, such as neuregulin-ErbB signaling[45] or glutamatergic signaling[46-50], in addition to axonal morphological thresholds[51]. Furthermore, a recent study observed that a subset of neocortical oligodendrocytes exclusively ensheath GABAergic interneurons, raising the possibility that distinct subtypes of oligodendrocytes might have neuronal cell type-specific rules governing axonal myelination[52].

Myelination of neocortical glutamatergic pyramidal neurons is modulated in vivo by experience, as well as direct manipulation of neuronal activity[53]. Activity-dependent myelination also extends to neocortical PV+ interneurons, a finding associated with concordant alterations in axonal morphology[4]. When considered together with the current findings, it is therefore possible that neuronal activity-dependent

myelination[54,55] in the cerebral cortex might be mediated by axonal morphological plasticity.

The current studies were focused primarily on locally-projecting GABAergic interneurons in prefrontal cortex. However, several studies have identified long-range GABAergic projecting cells including, but not limited to, PV+ and SOM+ subclasses[56-59]. The high proportion of cerebral cortex PV+ cells exhibiting axonal myelination[3] makes it likely that long-range PV+ cells are also myelinated. However, due to technical limitations of slicing and intracellular biocytin labeling, it was not possible to definitively identify and reconstruct long-range GABAergic axons. Thus, the question remains open whether long-range GABAergic axons are also frequently myelinated and whether axonal morphology is similarly predictive of their myelination. Moreover, a related issue regards whether the present findings acquired in grey matter also extend to white matter, especially given regional differences among oligodendrocyte lineage cells[60,61].

Myelination of GABAergic interneurons has been observed in multiple mammalian species[31]. Notably, human neocortical fast-spiking PV+ interneurons appear to have more extensive total myelination per cell than is observed in mice[3,43]. This raises the possibility that neocortical interneuron myelination might have a crucial influence on higher cognitive function, as well as potentially in the pathophysiology of disorders involving CNS myelination impairments, such as multiple sclerosis or schizophrenia[31,47]. Therefore, it is important to determine the extent to which the morphological determinants of interneuron myelination are evolutionarily conserved. Here, we have performed axonal reconstructions and determined the topographical distribution of myelin internodes along human fast-spiking interneurons from acutely resected ex vivo neocortical tissue. We found that segmental neocortical interneuron myelination conforms to similar bivariate morphological thresholds as observed in mouse neocortex, on the basis of interbranch distance and axonal diameter, suggesting a species conservation of the biophysical constraints on the myelinating function of oligodendrocytes.

In conclusion, we demonstrate that the joint combination of interbranch distance and axonal shaft diameter accurately predicts the topography of neocortical interneuron myelination in vivo in both mouse and human.

Materials and methods

Mice

All experiments were approved by the Dutch Ethical Committee and in accordance with the Institutional Animal Care and Use Committee (IACUC) guidelines. The following mouse lines were obtained from Jackson Laboratory:

- *Pvalb*[tm1(cre)Arbr]/J mice (*Pvalb*::cre)[11] www.jax.org/strain/008069
- *Sst*[tm2.1(cre)Zjh]/J (*Sst*::cre)[12,28] www.jax.org/strain/013044
- *Gt(ROSA)26Sor*[tm14(CAG-tdTomato)Hze]/J[12] (Ai14) www.jax.org/strain/013044
- *Tsc1*[tm1Djk]/J (*Tsc1*[f/f]) www.jax.org/strain/005680
- *C57BL/6J* (WT) www.jax.org/strain/000664

Floxed *Ube3a* mice (*Ube3a*[p+/mf]) were described previously[26].

All lines were backcrossed for more than 10 generations in C57BL/6J. Reporter lines were crossed to obtain heterozygous *Pvalb*::cre/heterozygous Ai14 (*Pvalb*::cre,Ai14) and heterozygous *Sst*::cre/heterozygous Ai14 (*Sst*::cre,Ai14). Mutant lines were crossed to obtain heterozygous *Pvalb*::cre/homozygous *Tsc1*[/f] (PV::TSC1). Heterozygous *Pvalb*::cre/heterozygous *Ube3a*[p+/mf] (PV::UBE3A) were obtained by crossing male homozygous *Pvalb*::cre with female *Ube3a*[p+/mf]. Heterozygous *Pvalb*::cre mice wildtype littermates for the mutant alleles from both breeding lines were used as controls (PV::WT). Both mutant lines were viable and healthy, although PV::TSC1 mice developed a severe ataxia during development. We have occasionally observed spontaneous seizures during routine handling in PV::TSC1 but not PV::UBE3A lines. In addition, mutant lines were crossed to obtain heterozygous *Sst*::cre/homozygous *Tsc1*[/f] (SOM::TSC1). Heterozygous *Sst*::cre mice wildtype littermates for the mutant alleles from this breeding lines were used as controls (SOM::WT). SOM::TSC1 mice did not display any behavioral abnormalities. No spontaneous seizures were observed during routine handling.

For all experiments, mice were used from 8 to 12 weeks of age. Mice were group-housed and maintained on a 12 h light/dark cycle (lights on 07:00-19:00) with ad libitum access to food and water. All experiments were performed during the light phase of the cycle.

Human brain tissue

Infiltrated peri-tumoral neocortical tissue was obtained from four patients undergoing tumor resection surgery at the Department of Neurosurgery (Erasmus University Medical Center, Rotterdam, The Netherlands). All procedures regarding human tissue were performed with the approval of the Medical Ethical Committee of the Erasmus University Medical Center. Written informed consent of each patient was provided in accordance with the Helsinki Declaration.

  – Patient #1 was an 84-year-old male who presented with a glioblastoma in the right parieto-occipital lobe. He had no significant psychiatric or past medical history, and no history of epilepsy or seizures. Patient received no anti-epileptic or cytostatic medication.

  – Patient #2 was a 52-year-old male who presented with metastases secondary to a melanoma in right temporal lobe. He had no significant psychiatric or other notable past medical history, and no history of epilepsy or seizures. Patient received no anti-epileptic or cytostatic medication.

  – Patient #3 was a 62-year-old male who presented with a right temporal lobe glioblastoma. He had no history of seizures, or notable psychiatric or medical history. Patient received no anti-epileptic or cytostatic medication.

  – Patient #4 was an 80-year-old male who presented with a glioblastoma in the right frontoparietal lobe. He had no significant psychiatric or other notable past medical history, no history of epilepsy or seizures, and received no anti-epileptic or cytostatic medication.

Viral labeling and CNO injections

Adult mouse viral labelling was performed as reported before[3], with minor adjustments. Specifically, adult PV::TSC1, PV::UBE3A, PV::WT, SOM::TSC1 and SOM::WT were used for axon diameter analysis, electrophysiology and single-cell reconstructions. Uncrossed heterozygous *Pvalb*::cre mice were used for PV-specific electron microscopy using APEX2. The following viral vectors were used:

  – AAV9/CAG-Flex-eGFP (University of Pennsylvania Viral Vector Core).
  – AAV2/CAG-Flex-mGFP-APEX2 (a gift from ML Leyrer and DM Berson)[62].

Anesthesia was induced using 5% isoflurane (O_2 flow of 0.5 L/min), and subsequently maintained with 1–2% isoflurane during surgery. Body temperature was maintained at 37°C. Mice were placed into a custom-made stereotaxic frame using a mouth bar (Stoelting) for head fixation. Analgesia was provided systemically by subcutaneous Temgesic injection (buprenorphine 0.5 mg/kg) and locally by xylocaine spray (100 mg/mL, AstraZeneca) directly applied on the skull. To access the brain, a longitudinal scalp incision of ~1 cm length was made to reveal the skull, and a small craniotomy (<1 mm) was performed overlying the injection sites at the following coordinates (in mm): mPFC: +1.75 bregma, ±0.35 lateral, −1.9 dorsoventral (mm, from brain surface).

Mice used for electrophysiological recordings received 0.5 µL in a ¼ dilution in 0.1 M PB. Virus was aspirated in a borosilicate glass micropipette, which was slowly lowered to the target site. Virus injection was controlled by an automated syringe pump (infusion speed 0.1 µl/min). At the conclusion of the injection, the micropipette was maintained

in place for 5 min and then slowly withdrawn. The surgical wound was closed with skin-glue (Derma+flex). Mice were left to recover for exactly 14 days to allow expression of the GFP protein. Importantly, mice were single-housed after surgery until used for electrophysiology or perfusion and immunofluorescence processing.

Electrophysiology

Mice

Anesthesia was induced using 5% isoflurane and mice were decapitated in ice-cold, NMDG-based cutting solution containing (in mM): 93 N-methyl-d-glucamine (NMDG), 93 HCl, 30 $NaHCO_3$, 25 D-glucose, 20 HEPES, 5 Na-ascorbate, two thiourea, 10 $MgCl_2$, 3 Na-pyruvate, 2.5 KCl, 1.25 NaH_2PO_4 and 0.5 $CaCl_2$ (300 mOsm, pH 7.4) oxygenated with 95% O_2/5% CO_2 before decapitation. After decapitation, the brain was quickly dissected. Coronal slices from the frontal cortex (300 μm) were cut with a vibrating slicer (Microm HM 650V, Thermo Scientific) and incubated in cutting solution at 37°C for 5 min., followed by oxygenated (95% O_2/5% CO_2) artificial cerebrospinal fluid (aCSF) at 37°C for 15 min. ACSF contained (in mM) 127 NaCl, 25 $NaHCO_3$, 25 D-glucose, 2.5 KCl, 1.25 NaH_2PO_4, 1.5 $MgSO_4$ and 1.6 $CaCl_2$. Slices were then allowed to recover at room temperature in the dark for at least 1 h before recordings.

In *Pvalb*::cre;Ai14 and *Sst*::cre;Ai14 mice, PV+ and SOM+ interneurons respectively were visualized by native tdTomato fluorescence using an RFP filter (Semrock, Rochester, NY, USA). In PV::TSC1, PV::WT, and PV::UBE3A mice, PV+ interneurons were visualized by expression of GFP using a GFP filter (Semrock, Rochester, NY, USA). Similarly, in SOM::TSC1 and SOM::WT mice, SOM+ interneurons were visualized by expression of eGFP using a GFP filter. Whole-cell recordings were made from layer III-V of the prelimbic area of the mPFC (between ~200 and 600 μm from midline; see Figure 1 – Figure supplement 3; bregma: +2.10 till +1.54 mm) at between ~20 μm and ~60 μm of the slice surface using borosilicate glass pipettes (3.5–5.5 MΩ resistance) with intracellular solution containing (in mM) 120 K-gluconate, 10 KCl, 10 HEPES, 10 K-phosphocreatine, 4 ATP-Mg, 0.4 GTP, and 5 mg/ml biocytin (pH was adjusted to 7.4 using KOH, and osmolarity measured 285–290 mOsm).

Recordings were performed in aCSF at near-physiological temperatures (32–33°C) using HEKA EPC10 quattro amplifiers and Patchmaster software (40 Hz sampling rate). Series resistance was typically <25 MΩ and fully compensated for bridge balance and capacitance; recordings in which the series resistance exceeded 25 MΩ were not included in the pooled averages. No correction was made for liquid junction potential. Data analysis was performed offline using Igor Pro v6 (Wavemetrics). Individual interneurons were recorded and filled for at least 20 min. In addition, cells were injected

at least 10 times with large depolarizing currents in current clamp mode (500 pA, 5 Hz, 2 s) to facilitate biotin diffusion into fine axonal arbors.

Basic physiological characteristics were determined from voltage responses to square-wave current pulses of 500 ms duration, ranging from –100 pA to +400 pA, and delivered in 20 pA intervals. Input resistance was determined by the slope of the linear regression through the voltage-current curve. Sag was determined as the voltage difference between the lowest voltage response and the steady-state response at the last 50 ms to a square-wave current pulses of 500 ms duration at –100 pA. Single action potential (AP) characteristics were obtained from the first elicited action potential. AP threshold was defined as the inflection point at the foot of the regenerative upstroke. AP amplitude was defined as the voltage difference between the threshold and peak voltage. AP half-width was measured at half of the peak amplitude. AP rise time was quantified as duration from 10% to 90% of the peak amplitude. The fast after-hyperpolarizing potential (fAHP) amplitude was measured as the peak hyperpolarizing deflection from AP threshold following AP initiation. AP frequency was determined from the number of APs in response to a square-wave current pulse of 500 ms duration.

Human

Ex vivo recordings of acutely resected frontal cortex were performed as previously described[3]. Non-eloquent overlaying tissue requiring surgical resection was utilized in order to access the location of a tumor. Immediately following resection, the tissue block was transferred to oxygenated (95% O_2/5% CO_2) ice-cold artificial cerebrospinal fluid (aCSF) containing (in mM) 127 NaCl, 25 $NaHCO_3$, 25 D-glucose, 2.5 KCl, 1.25 NaH_2PO_4, 1.5 $MgSO_4$ and 1.6 $CaCl_2$ during rapid transport to the laboratory. The time between surgical resection and tissue slicing was <10 min. Whole-cell recordings were performed similarly to mice as described above.

Fluorescence immunohistochemistry

Mouse

Deep anaesthesia was induced by intraperitoneal injection of pentobarbital, and mice were transcardially perfused with saline followed by 4% paraformaldehyde (PFA). Brains were dissected and post-fixed in 4% PFA for 2 h at room temperature. Brains were transferred into 10% sucrose phosphate buffer (PB 0.1 M, pH 7.3) and stored overnight at 4°C. Embedding was performed in a 12% gelatin/10% sucrose block, with fixation in 10% paraformaldehyde/30% sucrose solution (PB 0.1 M) for 2 h at room temperature and immersed in 30% sucrose (PB 0.1 M) at 4°C overnight. Forty micrometer coronal sections were collected serially (rostral to caudal) using a freezing microtome (Leica,

Wetzlar, Germany; SM 2000R) and stored in 0.1 M PB. Sections were pre-incubated with a blocking PBS buffer containing 0.5% Triton X-100% and 10% normal horse serum (NHS; Invitrogen, Bleiswijk, The Netherlands) for 1 h at room temperature. Sections were incubated in a mixture of primary antibodies in PBS buffer containing 0.4% Triton X-100% and 2% NHS for 72 h at 4°C. The following primary antibodies were used:

- mouse anti-PV (1:1000, Swant, 235, lot #10-11(F)); RRID:AB_10000343
- rabbit anti-PV (1:1000, Swant PV25); RRID:AB_10000344
- goat anti-MBP (1:300, Santa Cruz, C-16, sc-13914, lot #F2416); RRID:AB_648798
- mouse anti-MBP (1:300, Santa Cruz, F-6, sc-271524); RRID:AB_10655672
- mouse anti-Ube3a (1:300, Sigma, 3E5, SAB1404508, lot #G4251-3E5); RRID:AB_10740376
- rabbit anti-pS6$^{S235/236}$ (1:300, Cell Signaling Technologies, 2211S, lot #23); RRID:AB_331679
- goat anti-SOM (1:300, Santa Cruz, D-20, sc-7819, lot #E1915); RRID:AB_2302603
- mouse anti-APC [CC1] (1:200, Abcam, ab16794); RRID:AB_443473

Sections were washed with PBS and incubated with corresponding Alexa-conjugated secondary antibodies (1:300, Invitrogen) and cyanine dyes (1:300, Sanbio, Uden, The Netherlands) in PBS buffer containing 0.4% Triton X-100, 2% NHS for 2–5 h at room temperature. Sections were washed with PB 0.1 M and mounted on slides, cover slipped with Vectashield H1000 fluorescent mounting medium (Vector Labs, Peterborough, UK), sealed and imaged.

Recovery of biocytin-labelled cells following electrophysiological recordings was performed as reported before[3], with minor alterations. Specifically, 300 μm slices were incubated overnight at 4°C in fresh 4% paraformaldehyde (PFA). Slices were extensively rinsed at room temperature in PBS and stained in PBS buffer containing 0.4% Triton X-100, 2% normal horse serum (NHS; Invitrogen, Bleiswijk, The Netherlands) and streptavidin-conjugated secondary antibody (1:300, Jackson; for PV::cre,Ai14-labelled and SOM::cre,Ai14-labelled cells) or streptavidin-Cy3 (1:300; Invitrogen; for GFP-labelled cells) overnight at 4°C. Slices were washed with PBS and PB 0.1 M and mounted on slides, cover slipped with 150 μl Mowiol (Sigma), sealed, and imaged for their axonal morphology (see Confocal imaging and analysis). To avoid excessive thinning or dehydration of 300 μm sections, cells were mounted, immediately imaged and returned to PB 0.1 M directly after imaging.

After full cell imaging, 300 μm slices were extensively washed in PB 0.1 M and incubated overnight at 4°C in 30% sucrose (0.1 M PB). Sections were then carefully recut at 40 μm using a freezing microtome (Leica, Wetzlar, Germany; SM 2000R) and stored serially in 0.1 M PB at 4°C. Serial 40 μm sections were extensively washed with PBS and pre-

incubated with a blocking PBS buffer containing 0.5% Triton X-100% and 10% NHS for 1 h at room temperature. Sections were incubated in PBS buffer containing 0.4% Triton X-100% and 2% NHS for 72 h at 4°C and goat anti-MBP. Then, sections were washed with PBS, and incubated with corresponding Alexa-conjugated secondary antibodies (1:300, Invitrogen) and cyanine dyes (1:300, Sanbio, Uden, The Netherlands) in PBS buffer containing 0.4% Triton X-100, 2% NHS for 5 h at room temperature. For biocytin, streptavidin-A488 (1:300, Jackson) and streptavidin-Cy3 (1:300, Invitrogen) were additionally used. Sections were washed with PB 0.1M and mounted on slides, cover slipped with Vectashield H1000 fluorescent mounting medium (Vector Labs, Peterborough, UK), sealed and imaged.

Human tissue

Three-hundred μm electrophysiology slices with biocytin-labelled cells were incubated overnight at 4°C in 4% PFA. Slices were stained with secondary streptavidin-Cy3 (1:300, Sanbio, Uden, The Netherlands) in PBS buffer containing 0.5% Triton X-100% and 1% BSA for 5 h at room temperature. Next, three-hundred thick images were taken with confocal microscopy (see Confocal imaging and analysis). Slices were then rinsed at room temperature in 0.1 M PB, incubated for 16 h at 4°C in 10% sucrose (0.1 M PB), and overnight at 4°C in 30% sucrose (0.1 M PB). Forty μm sections were collected serially using a freezing microtome (Leica, Wetzlar, Germany; SM 2000R) and stored in 0.1 M PB. Sections were extensively washed and pre-incubated with a blocking PBS buffer containing 0.5% Triton X-100% and 5% bovine serum albumin (BSA; Sigma-Aldrich, The Netherlands) for 1 h at room temperature. Next, sections were incubated in a mixture of primary antibodies in PBS buffer containing 0.5% Triton X-100% and 1% BSA for 72 h at 4°C. The following primary antibodies were used: mouse anti-MBP (1:300, Santa Cruz, F-6, sc-271524).

Sections were extensively washed with PBS (>2 h), and incubated with corresponding Alexa-conjugated secondary antibodies (1:300, Invitrogen), and streptavidin-cyanine dyes (1:300, Sanbio, Uden, The Netherlands) in PBS buffer as previously described. Sections were washed with PB 0.1 M and mounted on slides, cover slipped with Vectashield H1000 fluorescent mounting medium (Vector Labs, Peterborough, UK) and sealed.

Confocal imaging and analysis

Confocal imaging was performed using a Zeiss LSM 700 microscope (Carl Zeiss) equipped with Plan-Apochromat 10x/0.45 NA, 40x/1.3 NA (oil immersion) and 63x/1.4 NA (oil immersion) objectives. Alexa405/DAPI, Alexa488, Cy3/mCherry/tdTomato, and

Alexa647 were imaged using excitation wavelengths of 405, 488, 555, and 639, respectively.

Quantification of interneuron-specific deletion of *Tsc1* or *Ube3a* as well as cell size analyses were performed in the prelimbic region in both hemispheres of the mPFC (bregma: +2.10 till +1.54 mm). We obtained tiled *z*-stack images (2048 × 2048 pixels) at 40x magnification with 1x digital zoom at a step size of 1 µm. Stacks were randomly sampled across layers II-V. For quantification of deletion efficiency, immunofluorescent somatic co-localization of PV or SOM and pS6$^{S235/236}$ or Ube3a was manually-counted using NIH ImageJ (version 1.41). At least three *z*-stacks were analyzed per mouse. For quantification of cell size, outlines of non-overlapping PV+ or SOM+ cell bodies were manually drawn and area and outline were calculated using Measure function of ImageJ. Cells were *post hoc* divided into pS6+ and pS6- or Ube3a+ and Ube3a- groups and compared.

Density of PV+, SOM+ and CC1+ cells were measured in the prelimbic area of the mPFC (bregma +2.20 till +1.70) in brain slices obtained from transcardially perfused animals. For PV+ cell counts, single plane 3 × 3 tile scan (1789 × 1789 µm) confocal images were obtained using the 10x objective with 1x digital zoom. All images captured both hemispheres. A 750 × 800 µm counting frame was established bilaterally from the midline. Within this counting frame, cells were manually counted utilizing the multi-point tool (Fiji image analysis software, version 2.0.0). Cell density was calculated in standardized 10^4 µm^2 fields of view. SOM+ and CC1+ cell counts were performed using single plane 6 × 3 tile scan (1767 × 896 µm) confocal images capturing both hemispheres, with a 20x objective and 1x digital zoom.

Overall myelination in the prelimbic area of the mPFC (bregma +2.20 to +1.70) was measured in brain slices obtained from transcardially perfused animals. To capture both hemispheres, single plain, 6 × 3 tile scans (1767 × 896 µm) where made using a 20x objective with 1x digital zoom. MBP+ fluorescent area was quantified by employing the particle analysis tool in Fiji image analysis software (version 2.0.0).

Axonal examinations of virally-labelled cells were obtained by 63x magnification with 1x digital zoom and a step size of 0.5 µm. Cells were randomly sampled from layers II-V of the prelimbic area of the mPFC. Examination of occurrence of axonal myelination was performed offline using ImageJ. Axons were identified as the thinnest, smoothest, and most highly branched processes originating from either the soma or primary dendrite. In addition, axons seemed to branch at more obtuse ≥90° angles from one another, often turning back toward the soma, whereas dendrites branched at smaller angles

(<90°), continuing their trajectory away from the soma. Additionally, SOM+ interneuron dendrites ubiquitously showed spines, whereas axons did not.

Axonal reconstructions of biocytin-filled cells were obtained at 63x magnification with 1x digital zoom and a step size of 0.5 µm. Images were transferred to Neurolucida 360 software (v2.8; MBF Bioscience) and reconstructed using interactive tracing with the Directional Kernels method. Reconstructed soma, axon and myelin segments were analyzed with Neurolucida Explorer (MBF Bioscience). All reconstructed PV+ cells had a classic basket cell morphology[30], for which none had a chandelier cell morphology. SOM+ cells predominantly exhibited a Martinotti morphology[30] with an axonal arbor directed toward layer II-III. All SOM+ interneurons contained dendritic spines, whereas none of the PV+ interneurons did, including in any of the mutant lines.

Images for exact locations of all biocytin-filled cells (Figure 1—Figure supplement 3) were obtained at 10x magnification with 1x digital zoom, and distance from the center of the soma till the midline was measured using ImageJ.

Axons were considered to be myelinated when they exhibited at least one MBP-positive myelinated internode. Axons were considered to be unmyelinated when we could not identify a single MBP-positive myelinated internode across the axon up to at least the 7th branch order in mice and 10th branch order in human cells. The distance to first myelin was defined as the distance along the axon from the soma, or in the case of dendrite-originating axons the distance from the originating dendrite, to the initial point of MBP immunofluorescence. Myelin segments that exited a slice were removed from subsequent analysis. Distance from internodes till consecutive branch points were quantified from the center of the branch point till the onset of MBP immunofluorescence. Internodes that were not followed by a branch point – followed by another internode or an axonal segment that exited the slice – were not taken along for analysis. No spatial corrections were made for tissue shrinkage.

Structured Illumination Microscopy (SIM) and Analysis

Imaging was performed using a Zeiss Elyra PS1 system. 3D-SIM data was acquired using a 63x/1.4 NA (oil immersion) objective. 488, 561 and 642 100 mW diode lasers were used to excite the fluorophores together with respectively a BP 495–575 + LP 750, BP 570–650 + LP 75 or LP 655 emission filter. For 3D-SIM imaging, a grating was present in the light path, modulated in 5 phases and five rotations, and multiple z-slices with an interval of 110 nm were recorded on an Andor iXon DU 885, 1002 × 1004 EMCCD camera. Raw images were reconstructed using Zen 2012 software (Zeiss), and analyzed with NIH ImageJ and Fiji image analysis software.

To avoid overexposure and induce background minimization, images were taken starting from the edge of the soma or dendrite following along the first axonal branch order onward. Each axonal segment was imaged individually from branch point till the next branch point, with the experimenter blinded to the myelination status of the segments. Axonal segments that exited the slice were removed from further analysis. Axonal segments that were predominantly oriented in the *z*-axis (maximum *z*-range: ~15–20 μm) were not taken along for further analysis.

For structured branch diameter analysis, images were loaded into Fiji and analyzed analogously to previously reported[13] using custom-written software. Briefly, an average-intensity projection was applied on individual axonal segments. A confocal whole-cell overview image and full reconstruction were used to track the centrifugal branch order of each traced segment. Segments were traced from the center of a branch point along the axon till the center of the next branch point using the Simple Neurite Tracer plugin for Fiji[63]. Traces always followed the centrifugal direction away from the soma. Next, along the trace, perpendicular lines of 50 pixels (equals 2 μm) were placed on every pixel (~40 nm) along the trace. On these perpendicular lines, biotin fluorescence intensity values were determined and a Gaussian curve was fitted on the intensity profile. Only fits with $r^2 > 0.9$ were included in further analysis, resulting in a loss of approximately ~10% of axonal pixel measurements. Subthreshold fits ($r^2 < 0.9$) occurred due to occasional high background fluorescence, other processes in close proximity (axons/dendrites), extensive axon curvature, or rare axonal filopodia. Next, from the Gaussian fit the full width at half maximum (FWHM) was calculated. Consecutive FHWM values were not averaged, and individual pixel FWHM values are provided. Diameter profiles of full axon segments (excluding branch points and *en passant* boutons) were generated and analyzed further. Axonal segments that exited the slice before reaching the next branch point would be excluded from further analysis. Where applicable, after complete analysis segments were divided into unmyelinated and myelinated segments.

For comparative axon diameter analysis of PV+ and SOM+ interneurons in PV::TSC1, PV::UBE3A, PV::WT, SOM::TSC1 and SOM::WT, GFP-transduced cells from layers II till V were imaged, and the axon diameter of individual cells was determined at the start of the AIS at ~3–5 μm from the soma or from the originating dendrite using FWHM measurements in Fiji. Similar to the detailed axon segment reconstructions, only measurements with fits > 0.9 were included in the analysis.

mGFP-APEX2 labeling, Electron Microscopy and image analysis

Adult heterozygous *Pvalb*::cre mice were unilaterally injected (see Viral Labeling) with AAV2/CAG-Flex-mGFP-APEX2 in a 0.5 μl bolus undiluted with a titre of 2.93×10^{12} in

the adult mPFC using the following coordinates: mPFC: +1.75 from bregma,±0.35 lateral, −1.9 dorsoventral (mm, from brain surface). After 7–14 days, mice were anesthetized by intraperitoneal injection of pentobarbital and transcardially perfused with saline followed by ice-cold 4% paraformaldehyde (PFA)/1% glutaraldehyde in 0.1M PB. Brains were carefully dissected and post-fixed in the same solution overnight at 4°C. The brains were washed extensively in cold 0.1 M PB, and 100 µm coronal slices from the frontal cortex (bregma: +2.10 till +1.54 mm) were cut on a vibrating slicer (Microm HM 650V, Thermo Scientific). Sections were serially stored in cold 0.1M PB and processed for 3–3'-diaminobenzidine (DAB) staining.

Sections were incubated in full concentration DAB (0.1 M PB, 0.66% DAB, 0.033% H_20_2) for 6 h at room temperature in the dark. Sections were washed in cold PB and post-fixed in cold 2% glutaraldehyde in 0.1 M PB for 2 h at 4°C. Regions of interest were manually cut out and processed for electron microscopy. Samples were post-fixed in 1% osmium tetroxide, dehydrated, and embedded in epoxy resin. Ultrathin sections (40–60 nm) were cut on a Leica Ultramicrotome Supercut UCT, contrasted with uranyl acetate and lead citrate and analyzed in a Phillips CM100 electron microscopy (Aachen, Germany) at 80 kV. Multiple non-overlapping regions were imaged at 14kx and analyzed off-line using Fiji image software.

Statistical analysis

Statistical analysis was performed using IBM SPSS (version 23). Data sets were analyzed using Shapiro-Wilk test for normality. No outlier data were identified or removed. Experiments were designed using sample sizes comparable to previously published studies[3,4]. Masking was used for group allocation, data collection, and data analysis whenever possible. Data sets with normal distributions were analyzed for significance using unpaired Student's two-tailed *t*-test or analysis of variance (ANOVA) measures followed by Tukey's *post hoc* test. Data are expressed as mean ± standard error. Data sets with non-normal distributions were analyzed using Mann-Whitney *U* test or Kruskal-Wallis test with Dunn's adjustment for multiple comparisons.

Receiver operating characteristic (ROC) curves were generated using a custom-written algorithm to implement univariate[14] and bivariate[64] methods. Univariate and bivariate thresholds were determined at the corresponding points of maximization of the Youden's *J* statistic[15], represented as the sum of the sensitivity and specificity. Area under the curve (AUC) values were computed as the integral of the univariate or bivariate ROC curves.

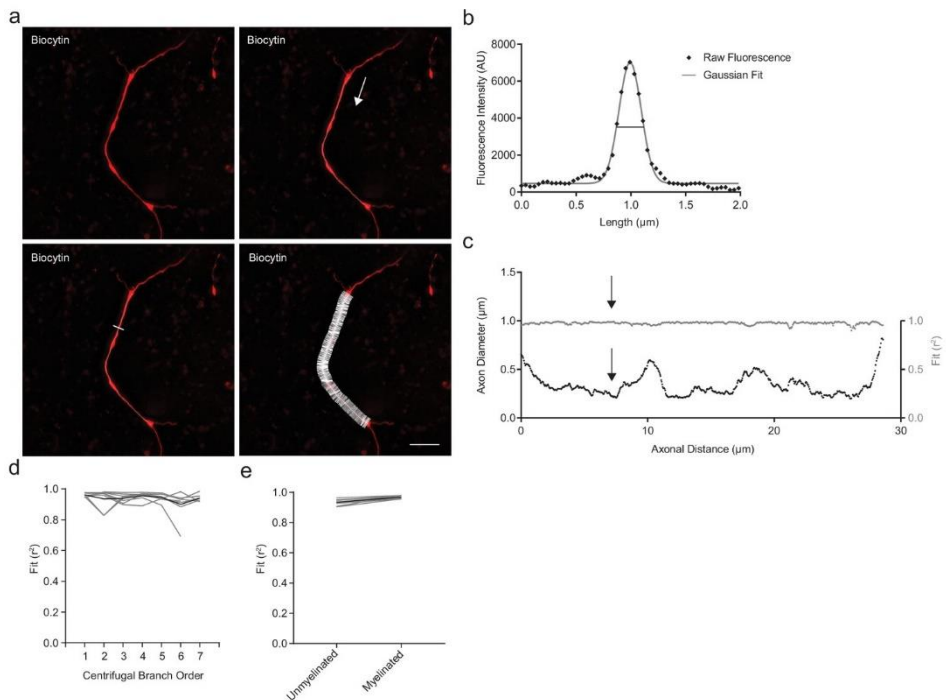Exact *P*-values values are provided in the text, except when p<0.001. Significance threshold was set at p<0.05.

Author contribution

Human PV interneuron electrophysiological recordings, immunohistochemistry, SIM imaging, reconstruction and analysis.

Supplementary data
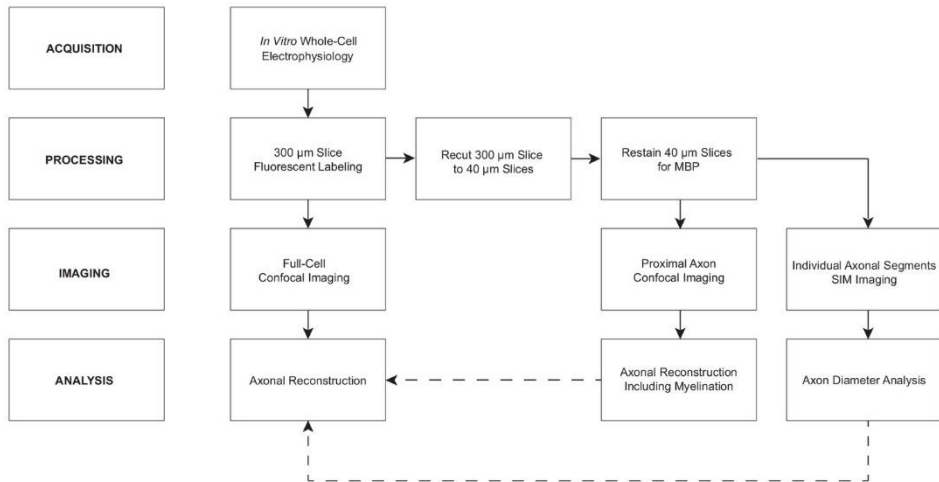
Figure 1 – supplement 1. Experimental flowchart for axonal reconstructions.

Figure 1 – supplement 2. Axonal diameter analysis. Interbranch axonal diameter was sampled at high spatial frequency from branch point to branch point. This representative example based on Figure 1e, depicts a 3rd order branch segment. **a**) Axonal diameter was measured using the

average intensity projection of a *z*-stack series of SIM images (red). A semi-automated, user-guided line was traced from the center of each axonal branch point to the center of the subsequent distal branch point (thin white line). Each segment was analyzed in the direction centrifugally oriented from the soma along the axon, as indicated by the white arrow. For every consecutive 40 nm of axon, a 50-pixel wide line (~2.0 μm) was drawn orthogonally to the tangent line of axonal orientation (white). Scale bar, 5 μm. **b**) Along the orthogonals, pixel fluorescence intensities were extracted (black diamonds) and a Gaussian line was fitted (grey). Fits with r^2 <0.9 were excluded from further analysis. From the Gaussian fit at each consecutive axonal position, the full-width at half-maximum (FWHM) was calculated. In this representative example, the FWHM (axonal diameter) =0.238 μm and r^2 = 0.987. **c**) Left axis: Axonal diameter measurements as a function of centrifugal distance along the axonal segment shown in (a). Right axis: Fit (r^2) of the Gaussian function along the axonal segment. Black arrows indicate the location of the corresponding fit shown in (b). **d**) Distribution over branch order of median Gaussian fit (r^2) prior to exclusion of points with r^2 <0.9. Individual cells in grey, average in black. **e**) Goodness of fit (r^2) is similar between myelinated and unmyelinated segments. Individual cells in grey, average in black. Abbreviations: FWHM, full-with at half-maximum.
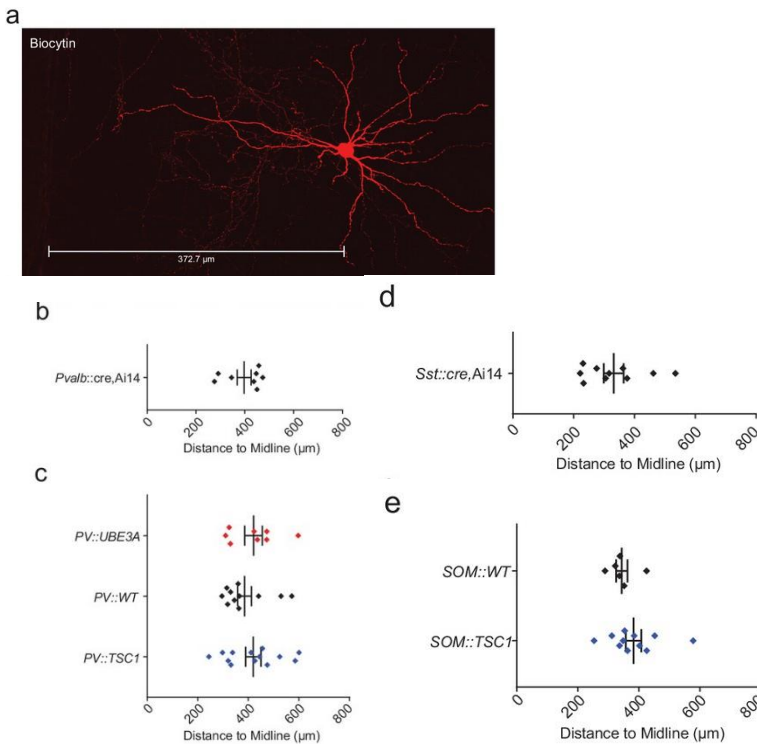

Figure 1 – supplement 3. Locations of biocytin-filled and reconstructed PV+ and SOM+ cells.
**a**) Maximum projection confocal image of a biocytin-filled mPFC SOM+ interneuron (red), with the distance to midline indicated. (b–e) Soma locations of *Pvalb*::cre,Ai14 cells **b**), PV::UBE3A, PV::WT, PV::TSC1 cells **c**), *Sst*::cre,Ai14 cells **d**), and SOM::WT, SOM::TSC1 cells **e**) Black bars indicate mean ± s.e.m.
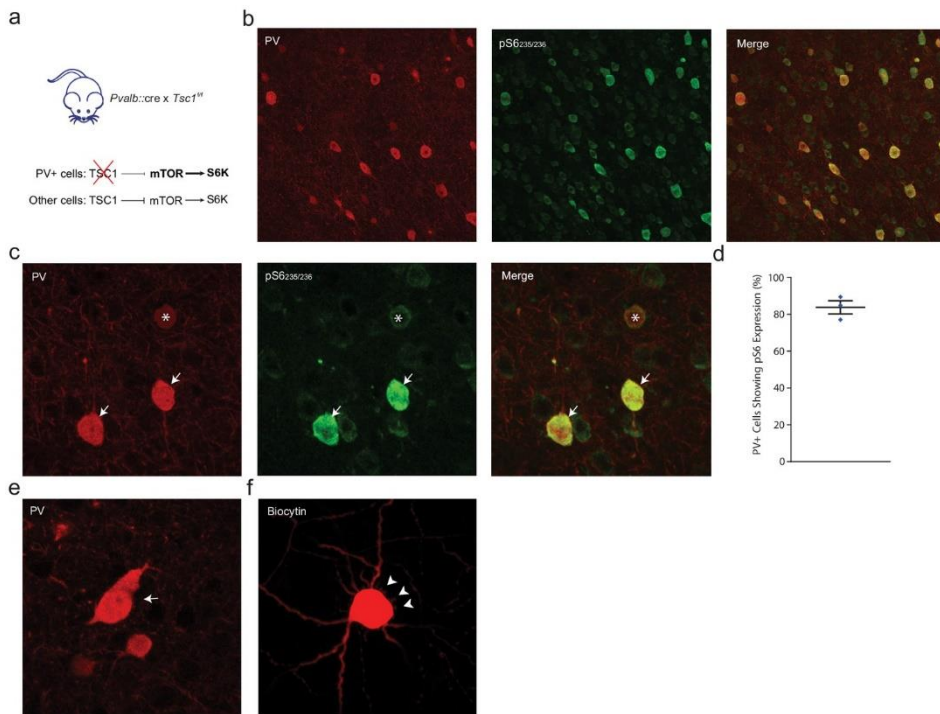
Figure 4 – supplement 1. PV::TSC1 mice exhibit PV-specific deletion of *Tsc1*. a) *Pvalb*::cre mice were crossed with floxed *Tsc1*$^{f/f}$ to obtain heterozygous *Pvalb*::cre x homozygous *Tsc1*$^{-/-}$ mice. In the absence of *Tsc1*, mTOR signaling is disinhibited leading to excessive S6K activity. **b**) Low magnification confocal image from the mPFC showing PV (red) and pS6$^{235/236}$ (green) immunofluorescence in adult mPFC, confirming the PV-specific increased S6K activity. **c**) Maximum projection confocal image showing increased expression of pS6$^{235/236}$ (green) in most (arrows) but not all (asterisk) PV+ cells (red). Uncropped image from Figure 4b. **d**) Corresponding deletion of *Tsc1* was observed in 83.8 ± 3.6% of PV+ cells, *n* = 3 mice. **e**). High magnification confocal image showing a rare instance of an oddly shaped enlarged pS6+ PV::TSC1 cell (red). **f**) Biocytin-filled PV::TSC1 cells (red) show short, thin filopodia (white arrowheads) radiating from the enlarged soma. Black bars indicate mean ± s.e.m.
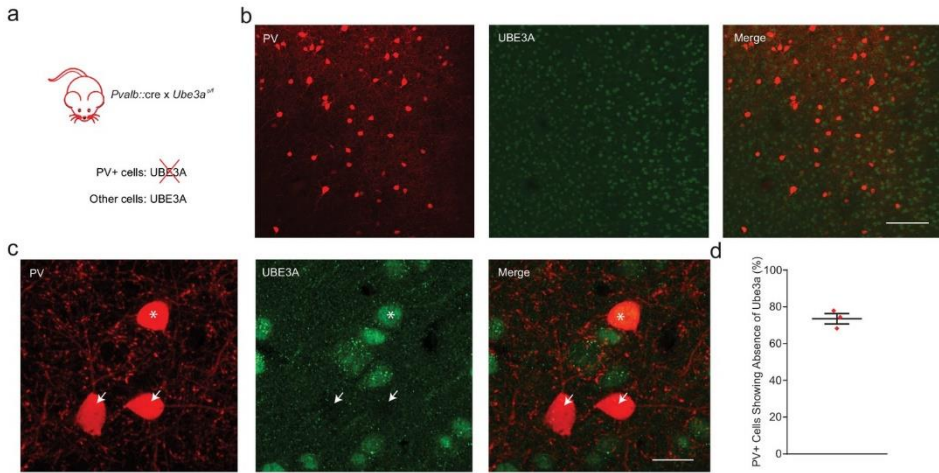
Figure 4 – supplement 2. PV::UBE3A mice exhibit PV+ cell-specific deletion of *Ube3a*. a) PV-specific knockout of *Ube3a*. **b**) Low magnification confocal microscopy image showing immunofluorescence of Ube3a (green) and PV (red) in adult mPFC. Note that the remaining non-PV neuronal cell types still retain intact Ube3a expression. Scale bar, 10 μm. **c**) High magnification confocal image confirming the absence of Ube3a (green) in most (arrows) but not all (asterisk) PV+ cells (red). Uncropped image corresponding to Figure 4b. **d**) *Ube3a* was deleted in 73.6 ± 2.8% of PV+ cells, *n* = 3 mice. Black bars indicate mean ± s.e.m.
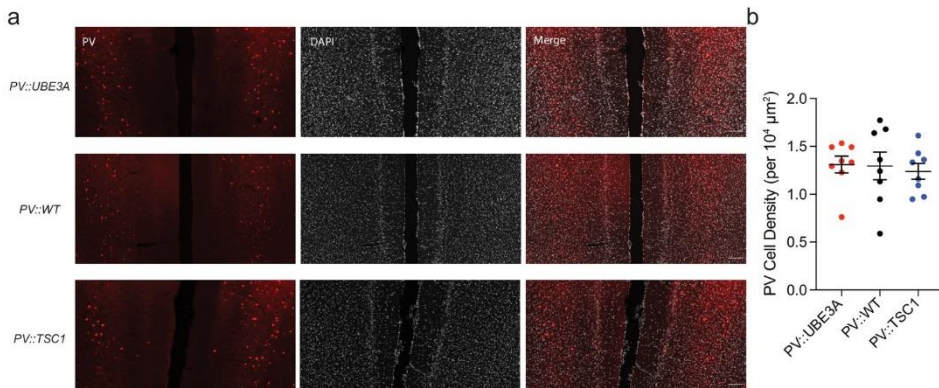

Figure 4 – supplement 3. PV cell-specific mutations of *Ube3a* or *Tsc1* do not alter PV+ cell density in mPFC. a) Confocal microscopy image showing immunofluorescence of PV (red) and DAPI (white) in adult mPFC for PV::UBE3A, PV::WT, and PV::TSC1. Scale bar, 100 μm. **b**) Quantification of PV+ cell density. p=0.780, Kruskal-Wallis test owing to non-normality. Black bars indicate mean ± s.e.m.
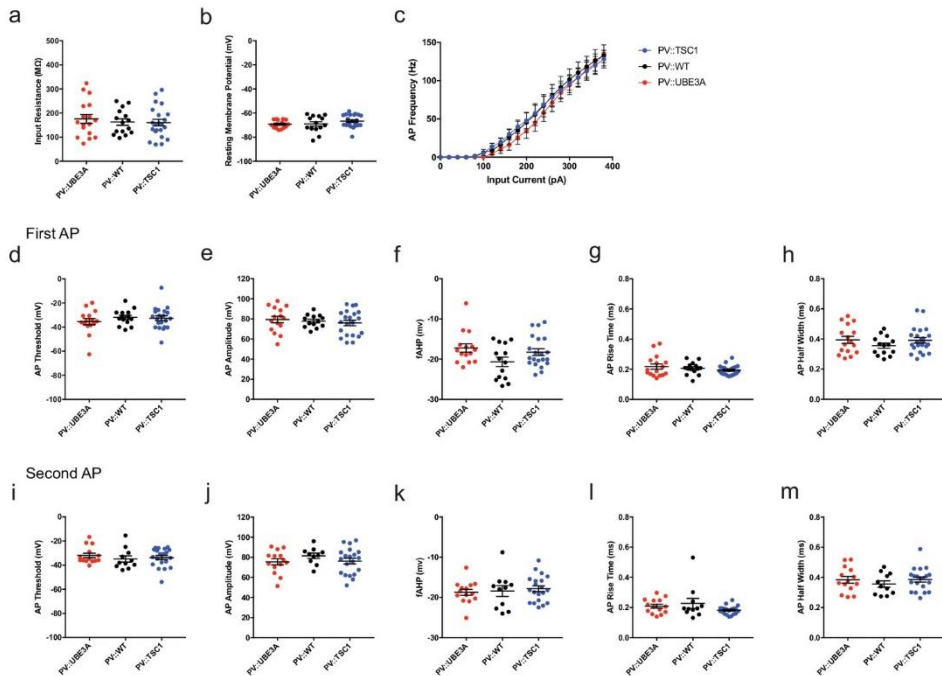
Figure 4 - supplement 4. Electrophysiological properties of PV::TSC1, PV::WT, and PV::UBE3A cells. a) input resistance. p=0.741. **b**) resting membrane potential. p=0.267. (**c**) Frequency-current plot, in response to square-wave current steps. p=0.999. PV::WT, *n* = 14 cells; PV::TSC1, *n* = 22 cells; PV::UBE3A, *n* = 16 cells. **d–h**) Analysis of the first action potential. **d**) AP threshold. p=0.518. **e**) AP amplitude. p=0.410. **f**) fast afterhyperpolarization (fAHP) amplitude. p=0.160. **g**) AP rise time. p=0.309. **h**) AP half-width. p=0.368. **i-m**) Analysis of the first action potential. **i**) AP threshold. p=0.696. **j**) AP amplitude. p=0.855. (**k**) fast afterhyperpolarization (fAHP) amplitude. p=0.073. (**l**) AP rise time. p=0.082. **m**) AP half-width. p=0.475. One-way ANOVA in **a**), **b**), **d**), **e**), **g**), **h**), **i**), **j**), **l**), and **m**). Mann-Whitney *U* test in **f**) and **k**). Repeated measures ANOVA in (**c**). Black bars indicate mean ± s.e.m. Abbreviations: AP, action potential; fAHP, fast afterhyperpolarization).
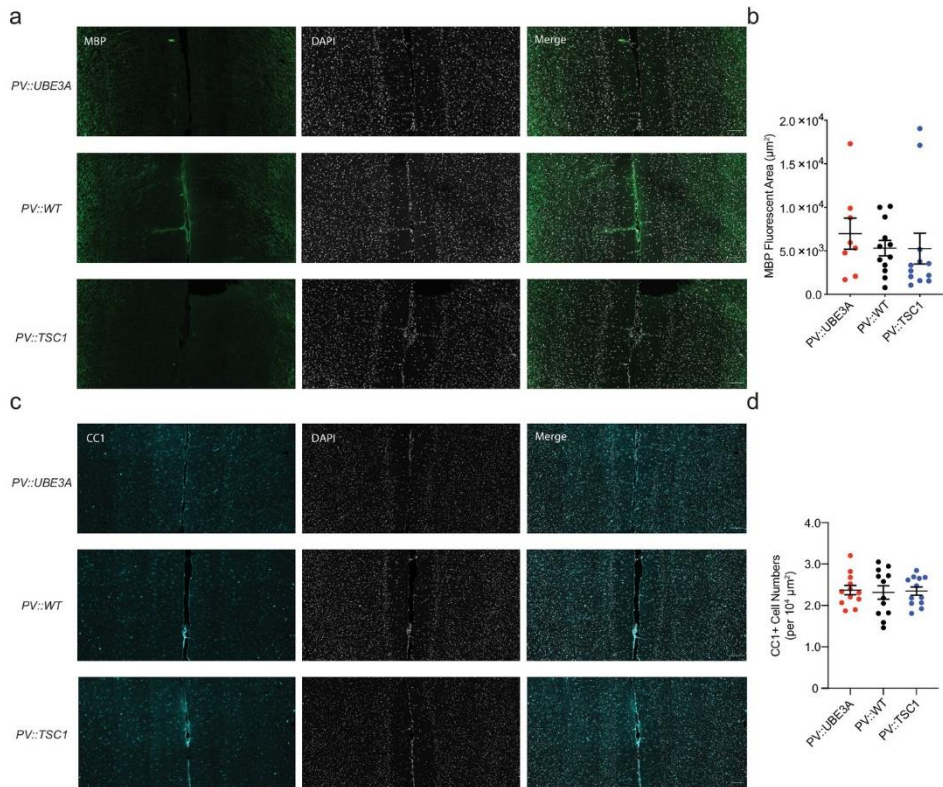
Figure 5 – supplement 1. Intact global myelination and mature oligodendrocyte density in mPFC of mice with PV cell-specific mutations of *Ube3a* or *Tsc1*. a) Confocal microscopy image showing immunofluorescence of MBP (green) and DAPI (white) for PV::UBE3A, PV::WT, and PV::TSC1. Scale bar, 100 μm. **b**) Quantification of MBP+ area. p=0.256, Kruskal-Wallis test owing to non-normality. **c**) Confocal microscopy image showing immunofluorescence of CC1+ mature oligodendrocytes (cyan) and DAPI (white) in adult mPFC for PV::UBE3A, PV::WT, and PV::TSC1. Scale bar, 100 μm. **d**) CC1+ mature oligodendrocyte density. p=0.950. One-way ANOVA. Black bars indicate mean ± s.e.m.
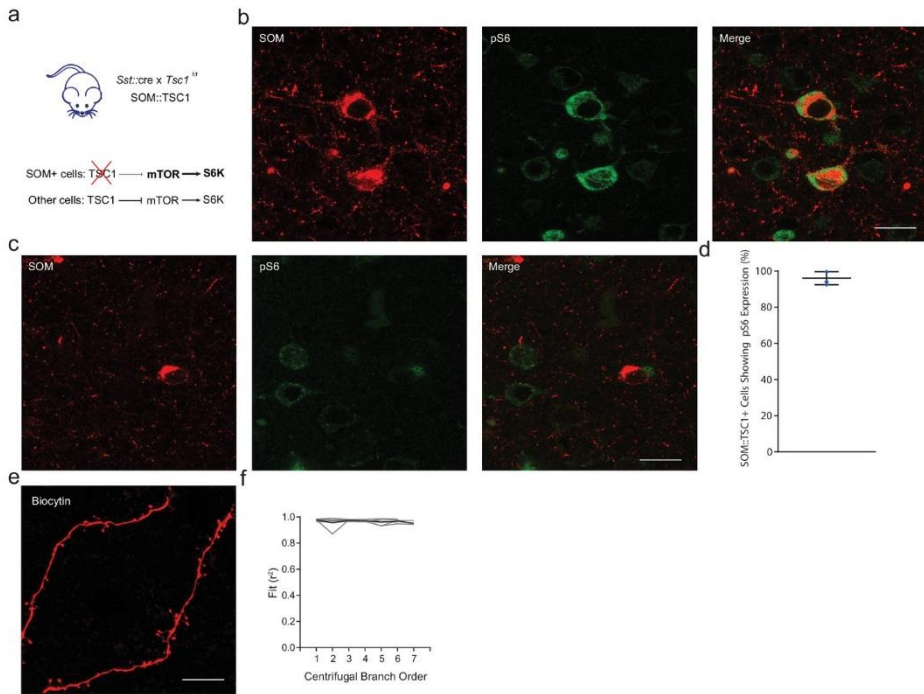
Figure 7 – supplement 1. SOM::TSC1 mice exhibit SOM-specific deletions of Tsc1. a) *Sst*::cre mice were crossed with floxed *Tsc1*$^{f/f}$ to obtain heterozygous *Sst*::cre x homozygous *Tsc1*$^{-/-}$ mice (SOM::TSC1). In the absence of *Tsc1*, mTOR signaling is disinhibited leading to excessive S6K activity. **b**) Maximum projection confocal image showing increased expression of pS6$^{235/236}$ (green) in most SOM::TSC1 cells (red). Uncropped image from Figure 7b. **c**) Maximum projection confocal image showing low expression of pS6$^{235/236}$ (green) in a minority of SOM::WT cells (red). Uncropped image from Figure 7b**. d**) Corresponding deletion of *Tsc1* was observed in 95.8 ± 2.1% of cells, *n* = 3 mice. **e**) High magnification SIM image of a biocytin-filled cell confirming the presence of dendritic spines on SOM+ interneurons. Scale bar, 10 μm. **f**) r^2 for FWHM Gaussian fits of SOM+ cell reconstructions. Median Gaussian fits (r^2) over branch order, prior to exclusion of points with r^2 <0.9. Individual cells in grey, average in black. Black bars denote means ± s.e.m.
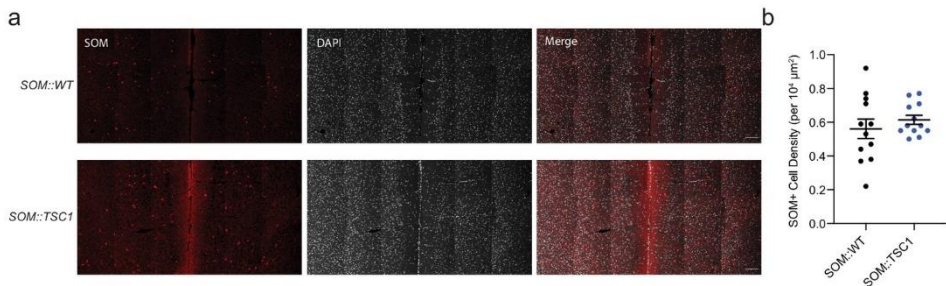
Figure 7 – supplement 2. SOM::TSC1 mice have a normal SOM+ cell density in mPFC. a) Confocal microscopy image showing immunofluorescence of SOM (red) and DAPI (white) in adult mPFC for SOM::WT, and SOM::TSC1. Scale bar, 100 μm. **b**) SOM+ cell density in mPFC of

SOM::TSC1 and SOM::WT mice. p=0.416, Unpaired two-tailed Student's t-test. Black bars indicate mean ± s.e.m.
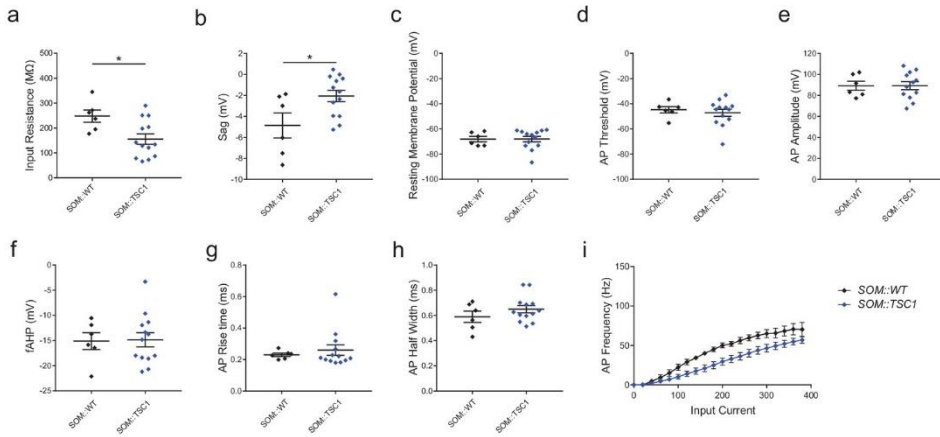
Figure 7 – supplement 3. Electrophysiological properties of SOM::TSC1 and SOM::WT cells.
a) input resistance. p=0.018. **b**) sag potential. p=0.023. **c**) resting membrane potential. p=0.993.
d) AP threshold. p=0.605. **e**) AP amplitude. p=0.994. f) fast afterhyperpolarization (fAHP)
amplitude. p=0.915. **g**) AP rise time. p=0.639. h) AP half-width. p=0.265. **i**) Frequency-current plot,
in response to square-wave current steps. p<0.001. SOM::WT, n = 6 cells; SOM::TSC1, n = 13
cells. *p<0.05 Unpaired two-tailed Student's t-test in **a**) through **f**) and **i**). Mann-Whitney U test in
h). Repeated measures ANOVA in **i**). Black bars denote means ± s.e.m. Abbreviations: AP, action
potential; fAHP, fast afterhyperpolarization.

References

1. Simons, M. & Nave, K.-A. Oligodendrocytes: Myelination and Axonal Support. *Cold Spring Harb. Perspect. Biol.* **8**, a020479 (2016).

2. Micheva, K. D. *et al.* A large fraction of neocortical myelin ensheathes axons of local inhibitory neurons. *Elife* **5**, (2016).

3. Stedehouder, J. *et al.* Fast-spiking Parvalbumin Interneurons are Frequently Myelinated in the Cerebral Cortex of Mice and Humans. *Cereb. Cortex* **27**, 5001–5013 (2017).

4. Stedehouder, J., Brizee, D., Shpak, G. & Kushner, S. A. Activity-Dependent Myelination of Parvalbumin Interneurons Mediated by Axonal Morphological Plasticity. *J. Neurosci.* **38**, 3631–3642 (2018).

5. Duncan, D. The Importance of Diameter as a Factor in Myelination. *Science (80-.).* **79**, 363–363 (1934).

6. Hildebrand, C., Remahl, S., Persson, H. & Bjartmar, C. Myelinated nerve fibres in the CNS. *Prog. Neurobiol.* **40**, 319–384 (1993).

7. Lee, S. *et al.* A culture system to study oligodendrocyte myelination processes using engineered nanofibers. *Nat. Methods* **9**, 917–922 (2012).

8. Bechler, M. E., Byrne, L. & Ffrench-Constant, C. CNS Myelin Sheath Lengths Are an Intrinsic Property of Oligodendrocytes. *Curr. Biol.* **25**, 2411–2416 (2015).

9. Goebbels, S. *et al.* A neuronal PI(3,4,5)P3-dependent program of oligodendrocyte precursor recruitment and myelination. *Nat. Neurosci. 2016 201* **20**, 10–15 (2016).

10. Auer, F., Vagionitis, S. & Czopka, T. Evidence for Myelin Sheath Remodeling in the CNS Revealed by In Vivo Imaging. *Curr. Biol.* **28**, 549-559.e3 (2018).

11. Hippenmeyer, S. *et al.* A Developmental Switch in the Response of DRG Neurons to ETS Transcription Factor Signaling. *PLOS Biol.* **3**, e159 (2005).

12. Madisen, L. *et al.* A toolbox of Cre-dependent optogenetic transgenic mice for light-induced activation and silencing. *Nat. Neurosci. 2012 155* **15**, 793–802 (2012).

13. Chéreau, R., Saraceno, G. E., Angibaud, J., Cattaert, D. & Nägerl, U. V. Superresolution imaging reveals activity-dependent plasticity of axon morphology linked to changes in action potential conduction velocity. *Proc. Natl. Acad. Sci. U. S. A.* **114**, 1401–1406 (2017).

14. Hanley, J. A. & McNeil, B. J. The meaning and use of the area under a receiver operating characteristic (ROC) curve. *Radiology* **143**, 29–36 (1982).

15. Jin, H. & Lu, Y. The ROC region of a regression tree. *Stat. Probab. Lett.* **79**, 936–942 (2009).

16. Karube, F., Kubota, Y. & Kawaguchi, Y. Axon Branching and Synaptic Bouton Phenotypes in GABAergic Nonpyramidal Cell Subtypes. *J. Neurosci.* **24**, 2853–2865 (2004).

17. Nörenberg, A., Hu, H., Vida, I., Bartos, M. & Jonas, P. Distinct nonuniform cable properties optimize rapid and efficient activation of fast-spiking GABAergic interneurons. *Proc. Natl. Acad. Sci. U. S. A.* **107**, 894–899 (2010).

18. Hu, H. & Jonas, P. A supercritical density of Na+ channels ensures fast signaling in GABAergic interneuron axons. *Nat. Neurosci. 2014 175* **17**, 686–693 (2014).

19. Fu, C. *et al.* GABAergic Interneuron Development and Function Is Modulated by the Tsc1 Gene. *Cereb. Cortex* **22**, 2111–2119 (2012).

20. Normand, E. A. *et al.* Temporal and mosaic Tsc1 Deletion in the developing thalamus disrupts thalamocortical circuitry, neural function, and behavior. *Neuron* **78**, 895–909 (2013).

21. Meikle, L. *et al.* A Mouse Model of Tuberous Sclerosis: Neuronal Loss of Tsc1 Causes Dysplastic and Ectopic Neurons, Reduced Myelination, Seizure Activity, and Limited Survival. *J. Neurosci.* **27**, 5546–5558 (2007).

22. Carson, R. P., Van Nielen, D. L., Winzenburger, P. A. & Ess, K. C. Neuronal and glia abnormalities in Tsc1-deficient forebrain and partial rescue by rapamycin. *Neurobiol. Dis.* **45**, 369–380 (2012).

23. Markus, A., Zhong, J. & Snider, W. D. Raf and Akt mediate distinct aspects of sensory axon growth. *Neuron* **35**, 65–76 (2002).

24. Sidorov, M. S. *et al.* Enhanced Operant Extinction and Prefrontal Excitability in a Mouse Model of Angelman Syndrome. *J. Neurosci.* **38**, 2671–2682 (2018).

25. Wallace, M. L., Burette, A. C., Weinberg, R. J. & Philpot, B. D. Maternal Loss of Ube3a Produces an Excitatory/Inhibitory Imbalance through Neuron Type-Specific Synaptic Defects. *Neuron* **74**, 793–800 (2012).

26. Judson, M. C. C. *et al.* GABAergic Neuron-Specific Loss of Ube3a Causes Angelman Syndrome-Like EEG Abnormalities and Enhances Seizure Susceptibility. *Neuron* **90**, 56–69 (2016).

27. Urban-Ciecko, J. & Barth, A. L. Somatostatin-expressing neurons in cortical networks. *Nat. Rev. Neurosci. 2016 177* **17**, 401–409 (2016).

28. Taniguchi, H. *et al.* A Resource of Cre Driver Lines for Genetic Targeting of GABAergic Neurons in Cerebral Cortex. *Neuron* **71**, 995–1013 (2011).

29. Redmond, S. A. *et al.* Somatodendritic Expression of JAM2 Inhibits Oligodendrocyte Myelination. *Neuron* **91**, 824–836 (2016).

30. Jiang, X. *et al.* Principles of connectivity among morphologically defined cell types in adult neocortex. *Science* **350**, aac9462 (2015).

31. Stedehouder, J. & Kushner, S. A. Myelination of parvalbumin interneurons: a parsimonious locus of pathophysiological convergence in schizophrenia. *Mol. Psychiatry* **22**, 4–12 (2017).

32. Tomassy, G. S. *et al.* Distinct Profiles of Myelin Distribution. *Science (80-.).* **344**, 319–324 (2014).

33. Chong, S. Y. C. *et al.* Neurite outgrowth inhibitor Nogo-A establishes spatial segregation and extent of oligodendrocyte myelination. *Proc. Natl. Acad. Sci.* **109**, 1299–1304 (2012).

34. Freeman, S. A. *et al.* Acceleration of conduction velocity linked to clustering of nodal components precedes myelination. *Proc. Natl. Acad. Sci. U. S. A.* **112**, E321–E328 (2015).

35. Kann, O., Papageorgiou, I. E. & Draguhn, A. Highly energized inhibitory interneurons are a central element for information processing in cortical networks. *J. Cereb. Blood Flow Metab.* **34**, 1270–1282 (2014).

36. Lee, Y. *et al.* Oligodendroglia metabolically support axons and contribute to neurodegeneration. *Nature* **487**, 443–448 (2012).

37. Fünfschilling, U. *et al.* Glycolytic oligodendrocytes maintain myelin and long-term axonal integrity. *Nature* **485**, 517–521 (2012).

38. Saab, A. S. *et al.* Oligodendroglial NMDA Receptors Regulate Glucose Import and Axonal Energy Metabolism. *Neuron* **91**, 119–132 (2016).

39. Hu, H., Gan, J. & Jonas, P. Fast-spiking, parvalbumin+ GABAergic interneurons: From cellular design to microcircuit function. *Science (80-.).* **345**, (2014).

40. Strüber, M., Jonas, P. & Bartos, M. Strength and duration of perisomatic gabaergic inhibition depend on distance between synaptically connected cells. *Proc. Natl. Acad. Sci. U. S. A.* **112**, 1220–1225 (2015).

41. Markram, H. *et al.* Interneurons of the neocortical inhibitory system. *Nat. Rev. Neurosci. 2004 510* **5**, 793–807 (2004).

42. Timmler, S. & Simons, M. Grey matter myelination. *Glia* **67**, 2063–2070 (2019).

43. Micheva, K. D. *et al.* Distinctive Structural and Molecular Features of Myelinated Inhibitory Axons in Human Neocortex. *eNeuro* **5**, 297–315 (2018).

44. Schmidt, H. *et al.* Axonal synapse sorting in medial entorhinal cortex. *Nat. 2017 5497673* **549**, 469–475 (2017).

45. Lundgaard, I. *et al.* Neuregulin and BDNF Induce a Switch to NMDA Receptor-Dependent Myelination by Oligodendrocytes. *PLOS Biol.* **11**, e1001743 (2013).

46. Gautier, H. O. B. *et al.* Neuronal activity regulates remyelination via glutamate signalling to oligodendrocyte progenitors. *Nat. Commun. 2015 61* **6**, 1–15 (2015).

47. Habermacher, C., Angulo, M. C. & Benamer, N. Glutamate versus GABA in neuron–oligodendroglia communication. *Glia* **67**, 2092–2106 (2019).

48. Kougioumtzidou, E. *et al.* Signalling through AMPA receptors on oligodendrocyte precursors promotes myelination by enhancing oligodendrocyte survival. *Elife* **6**, (2017).

49. Chen, T. J. *et al.* In Vivo Regulation of Oligodendrocyte Precursor Cell Proliferation and Differentiation by the AMPA-Receptor Subunit GluA2. *Cell Rep.* **25**, 852-861.e7 (2018).

50. Berret, E. *et al.* Oligodendroglial excitability mediated by glutamatergic inputs and Nav1.2 activation. *Nat. Commun. 2017 81* **8**, 1–15 (2017).

51. Makinodan, M., Rosen, K. M., Ito, S. & Corfas, G. A critical period for social experience-dependent oligodendrocyte maturation and myelination. *Science (80-.).* **337**, 1357–1360 (2012).

52. Zonouzi, M. *et al.* Individual Oligodendrocytes Show Bias for Inhibitory Axons in the Neocortex. *Cell Rep.* **27**, 2799-2808.e3 (2019).

53. Fields, R. D. A new mechanism of nervous system plasticity: activity-dependent myelination. *Nat. Rev. Neurosci. 2015 1612* **16**, 756–767 (2015).

54. Gibson, E. M. *et al.* Neuronal activity promotes oligodendrogenesis and adaptive myelination in the mammalian brain. *Science (80-.).* **1252304**, (2014).

55. Mitew, S. *et al.* Pharmacogenetic stimulation of neuronal activity increases myelination in an axon-specific manner. *Nat. Commun.* **9**, 306 (2018).

56. Caputi, A., Melzer, S., Michael, M. & Monyer, H. The long and short of GABAergic neurons. *Curr. Opin. Neurobiol.* **23**, 179–186 (2013).

57. Melzer, S. *et al.* Distinct Corticostriatal GABAergic Neurons Modulate Striatal Output Neurons and Motor

Activity. *Cell Rep.* **19**, 1045–1055 (2017).

58. Rock, C., Zurita, H., Wilson, C. & Apicella, A. J. An inhibitory corticostriatal pathway. *Elife* **5**, (2016).

59. Lee, A. T., Vogt, D., Rubenstein, J. L. & Sohal, V. S. A Class of GABAergic Neurons in the Prefrontal Cortex Sends Long-Range Projections to the Nucleus Accumbens and Elicits Acute Avoidance Behavior. *J. Neurosci.* **34**, 11519–11525 (2014).

60. Dimou, L. & Simons, M. Diversity of oligodendrocytes and their progenitors. *Curr. Opin. Neurobiol.* **47**, 73–79 (2017).

61. Spitzer, S. O. *et al*. Oligodendrocyte Progenitor Cells Become Regionally Diverse and Heterogeneous with Age. *Neuron* **101**, 459-471.e5 (2019).

62. Leyrer, M. L. A genetically encoded marker for light-and electron-microscopic analysis of neuronal cell types. in (2016).

63. Longair, M. H., Baker, D. A. & Armstrong, J. D. Simple neurite tracer: Open source software for reconstruction, visualization and analysis of neuronal processes. *Bioinformatics* **27**, 2453–2454 (2011).

64. Wang, M. C. & Li, S. ROC analysis for multiple markers with tree-based classification. *Lifetime Data Anal. 2012 192* **19**, 257–277 (2012).

Chapter 5

Myelination synchronizes cortical oscillations by consolidating parvalbumin-mediated phasic inhibition

M. Dubey[1] , M. Pascual-García[2] , K. Helmes[1] , D. D. Wever[1] ,
M. S. Hamada[1 3] , S. A. Kushner[2] , M. H. P Kole[1 3]

[1] Department of Axonal Signaling, Netherlands Institute for Neuroscience (NIN), Royal Netherlands
Academy of Arts and Sciences (KNAW), Amsterdam, Netherlands.
[2] Department of Psychiatry, Erasmus Medical Centre, Rotterdam, Netherlands.
[3] Cell Biology, Neurobiology and Biophysics, Department of Biology, Faculty of Science, Utrecht
University, Utrecht, Netherlands.

Abstract

Parvalbumin-positive (PV+) γ-aminobutyric acid (GABA) interneurons are critically involved in producing rapid network oscillations and cortical microcircuit computations, but the significance of PV+ axon myelination to the temporal features of inhibition remains elusive. Here, using toxic and genetic mouse models of demyelination and dysmyelination, respectively, we find that loss of compact myelin reduces PV+ interneuron presynaptic terminals and increases failures, and the weak phasic inhibition of pyramidal neurons abolishes optogenetically driven gamma oscillations in vivo. Strikingly, during behaviors of quiet wakefulness selectively theta rhythms are amplified and accompanied by highly synchronized interictal epileptic discharges. In support of a causal role of impaired PV-mediated inhibition, optogenetic activation of myelin-deficient PV+ interneurons attenuated the power of slow theta rhythms and limited interictal spike occurrence. Thus, myelination of PV axons is required to consolidate fast inhibition of pyramidal neurons and enable behavioral state-dependent modulation of local circuit synchronization.

Introduction

GABAergic interneurons play fundamental roles in controlling rhythmic activity patterns and the computational features of cortical circuits. Nearly half of the interneuron population in the neocortex is parvalbumin-positive (PV[+]) and comprised mostly of the basket cell (BC) type[1,2]. PV[+] BCs are strongly and reciprocally connected with pyramidal neurons (PNs) and other interneurons, producing temporally precise and fast inhibition[3-5]. The computational operations of PV[+] BCs, increasing gain control, sharpness of orientation selectively, and feature selection in the sensory cortex[6-10], are mediated by a range of unique molecular and cellular specializations. Their extensive axon collaterals targeting hundreds of PNs are anatomically arranged around the soma and dendrites, and electrotonically close to the axonal output site. In addition, the unique calcium (Ca2^{+}) sensor in PV[+] BCs terminals, synaptotagmin 2 (Syt2), is tightly coupled to Ca2^{+} channels mediating fast and synchronized release kinetics[11,12], powerfully shunting excitatory inputs and increasing the temporal precision of spike output[1,5,13,14].

Recent findings have shown that the proximal axons of PV[+] interneurons are covered by myelin sheaths[5,13,15-18]. How interneuron myelination defines cortical inhibition remains, however, still poorly understood. Myelination of axons provides critical support for long-range signaling by reducing the local capacitance that results in rapid saltatory conduction and by maintaining the axonal metabolic integrity[19,20]. For PV[+] BCs, however, the average path length between the axon initial segment (AIS) and release sites involved in local circuit inhibition is typically less than ~200 μm[5,21,22], and theoretical and experimental studies indicate the acceleration by myelin may play only a limited role[15,21]. Another notable long-standing hypothesis is that myelination of PV[+] axons may be critical for the security and synchronous invasion of presynaptic terminals[13]. In support of a role in reliability, in Purkinje cell axons of the long Evans shaker (les) rat, which carries a deletion of Mbp, spike propagation shows failures and presynaptic terminals are disrupted[23]. Interestingly, in a genetic model in which oligodendrocyte precursor cells lack the γ2 GABAA receptor subunit, fast-spiking interneuron axons in the neocortex are aberrantly myelinated and feedforward inhibition is impaired[24]. At the network level, PV[+] BC-mediated feedback and feedforward inhibition is critical to produce local synchronization between PNs and interneuron at the gamma (γ) frequency (30–80 Hz), which is a key rhythm binding information from cell assemblies, allowing synaptic plasticity and higher cognitive processing of sensory information[1,7,25-27]. Here, we determined whether PV[+] BC-driven neocortical rhythms require myelination by using de- and dysmyelination models, studying the cellular properties

of genetically labeled PV[+] BCs and examining the functional role of myelin by longitudinally examining the frequency spectrum of cortical oscillations.

Results

Behavioral state-dependent increase in theta power and interictal epileptiform discharges

We investigated in vivo cortical rhythms by recording local field potential (LFP) in layer 5 (L5) together with surface electrocorticogram (ECoG) signals from both primary somatosensory (S1) and visual (V1) areas. Freely moving mice (C57BL/6, 7–9 weeks at the start of the experiment) were recorded in their home cage every second week (18–24 hr/week) across an 8-week cuprizone treatment, inducing toxic loss of oligodendrocytes in white- and gray matter areas[28-30]. Remarkably, after 6 weeks of cuprizone feeding we detected high-voltage spike discharges (approximately five times the baseline voltage and ~50–300 ms in duration, **Figure 1a – c**). These brief spike episodes on the ECoG and LFP (**Figure 1c**) occurred bilaterally and near synchronously in S1 and V1, resembling the interictal epileptiform discharges (also termed interictal spikes) that are a hallmark of epilepsy[31-34]. Automated detection of interictal spikes in the raw ECoG–LFP signal was performed with a machine-based learning classifier (see **Figure 1 – figure supplement 1** and *Materials and methods*), revealing a progressively increasing number of interictal spikes, from ~5/hr at 4 weeks up to ~70/hr at 8 weeks of cuprizone treatment (**Figure 1d**). Interestingly, interictal spikes were highly dependent on vigilance state and present exclusively during quiet wakefulness (30 out of 30 randomly selected LFP segments from awake or quiet wakefulness, chi-square test p<0.0001, n = 6 cuprizone mice), with no other discernible association to specific behaviors (**Figure 1–figure supplement 1b, Figure 1**). Whether the pathological cortical oscillations were specific to certain frequency bands, including gamma (γ, 30–80 Hz), was examined by plotting the power spectrum density of the LFP in S1 during periods of quiet wakefulness or active movement (**Figure 1e**). During quiet wakefulness, LFP power in cuprizone-treated mice was selectively amplified in the theta frequency band (θ, 4–12 Hz, Šidák's multiple comparisons test, p=0.0013, **Figure 1e, f, Figure 1 – figure supplement 1c**). In contrast, during active states when mice were moving and exploring no differences were observed in the power spectrum, in none of the frequency bands (Šidák's multiple comparisons test, p>0.166, **Figure 1e, f, Source data 1**). Finally, to more firmly establish whether interictal epileptiform discharges result from the lack of myelin, we analyzed ECoG signals in the dysmyelinated shiverer mice (MbpShi) lacking compact myelin due to a truncating mutation in Mbp[35]. Shiverer mice suffer progressively increasing number of epileptic seizures beginning at approximately

8 weeks of age[35,36]. ECoG recordings at 8 weeks showed that in addition to ictal discharges interictal spikes were detected with a rate of ~1/min, comparable to cuprizone-treated mice (**Figure 1g and h, Figure 1 – figure supplement 2**). Although the waveform of interictal spikes in shiverer was substantially longer in duration (~100–500 ms), analysis of the power across the four frequency bands around interictal spikes revealed no difference in comparison to the cuprizone-treated mice (two-way analysis of variance [ANOVA] p=0.7875, n = 6 mice for both groups, **Figure 1 – figure supplement 2**).
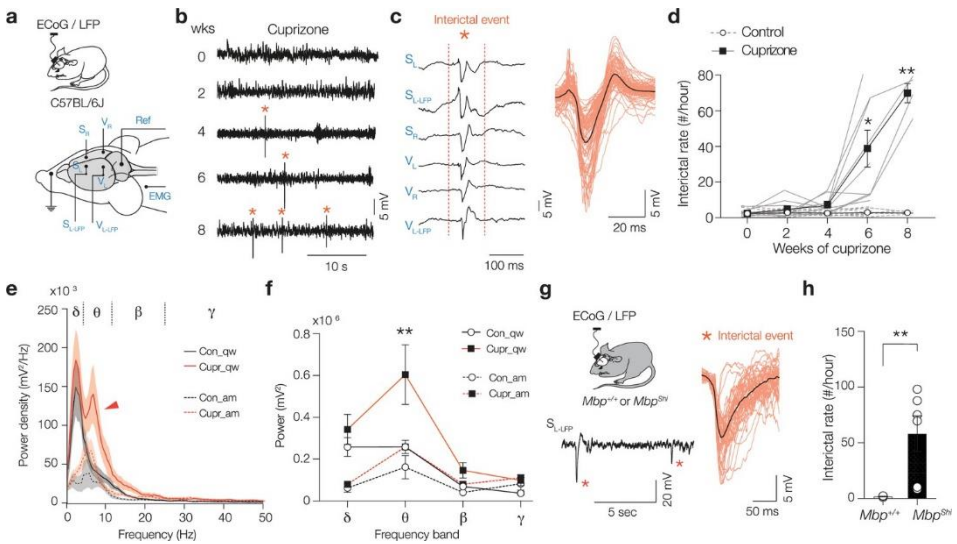
Figure 1. Loss of compact myelin causes interictal spikes and behavioral state-dependent amplification of theta rhythms. a) Schematic of the electrocorticogram (ECoG) and local field potential (LFP) recordings in freely moving mice. Electrodes were placed right (S_R) and left (S_L) in the primary somatosensory cortex, and a left LFP electrode (S_{L-LFP}) into layer 5 (L5). A similar array of electrodes was positioned in the primary visual cortex (V_R, V_L, and V_{L-LFP}). One electrode was placed around neck muscle recording electromyography (EMG) and one used as reference (Ref). **b**) Interictal spikes (*) appear from 4-week cuprizone and onward. Example raw LFP traces (S_{L-LFP}). **c**) Representative interictal spike example showing spatiotemporal synchronization of the spike across cortical areas and hemispheres. Higher magnification of interictal spikes (red, ~50–300 ms duration) overlaid with the average (black). **d**) Cuprizone treatment caused a progressively increasing frequency of interictal spikes (mixed-effects two-way ANOVA). Time × treatment interaction p<0.0001, Šidák's multiple comparisons tests, cupri vs. con; 4 weeks p=0.121, 6 weeks *p=0.0406 and 8 weeks **p=0.0054. **e**) Power spectral content during two different brain states, awake and moving (am, dotted lines) and quiet wakefulness (qw, solid lines) in control (black) and cuprizone (red). Red arrow marks amplified theta band power (θ) during quite wakefulness in cuprizone mice (Cupr_qw). **f**) Cuprizone amplifies selectively θ power during quiet wakefulness (two-way ANOVA treatment p<0.0001, Šidák's multiple comparisons cupr vs. con; for δ, p=0.8118; θ, p=0.0013; β, p=0.8568 and for γ, p=0.9292) but not during moving (two-way ANOVA treatment p=0.0575). **g**) Left: schematic of ECoG and LFP recordings from $Mbp^{+/+}$ and Mbp^{Shi} mice with

example trace showing interictal spikes (*). Right: overlaid individual interictal spikes in Mbp^{Shi} mice (red) combined with the population average (black). **h**) Bar plot of interictal rate in Mbp^{Shi} mice. Two-tailed Mann–Whitney test **p=0.0095. Data shown as mean ± SEM with gray lines d) or open circles h) individual mice.

Loss of myelin impairs fast PV+ BC-mediated inhibition

Increased power of sensory-driven slow oscillations and epileptiform activity in the neocortex of normally myelinated brains is also observed when PV[+] interneurons are optogenetically silenced[9,27,37]. To investigate how myelin loss affects the PV[+] interneuron morphological and functional properties, we crossed the PvalbCre mouse line, having Cre recombinase targeted to Pvalb-expressing cells, with a tdTomato fluorescence (Ai14) Cre reporter line (hereafter called PV-Cre; Ai14 mice). The cytoplasmic fluorescence allowed quantification of PV[+] cell bodies and their processes in the primary somatosensory cortex (**Figure 2a, b, Figure 2 – figure supplement 1a**), and immunofluorescent labeling with myelin basic protein (MBP) revealed substantial myelination of large-diameter PV[+] axons (mean ± SEM, 80.15% ± 9.95% along 83 mm of PV[+] axons analyzed, n = 3 slices from two mice, z-stack with a volume of 7.66 × 105 µm3, **Figure 2b, Figure 2 – figure supplement 1a**). Electron microscopy (EM) immunogold-labeled tdTomato showed that PV[+] axons possessed multilamellar compact myelin sheaths (on average, 6.33 ± 0.80 myelin lamella) with 10.8 ± 0.76 nm distance between the major dense lines and a mean g-ratio (axon diameter/fiber diameter) of 0.74 ± 0.01 (n = 6 sheaths, **Figure 2c**). PV-Cre; Ai14 mice fed with 0.2% cuprizone for 6 weeks showed strongly reduced MBP in S1 and PV[+] axons were largely devoid of myelin (**Figure 2a, b, Figure 2 – figure supplement 1b**) while the total number of PV[+] cell bodies across cortical layers remained constant (control density, 326 ± 14 cells mm–2 vs. cuprizone density, 290 ± 48 cells mm–2, n = 6 sections from N = 6 animals/group, Mann–Whitney test p=0.1649, **Figure 2d**). Further, single-cell analysis was performed on biocytin-filled PV-Cre[+] interneurons that were re-sectioned and stained for MBP to identify the location of myelin and the axon morphology (**Figure 2e, Figure 2 – figure supplement 1c, d**). Myelin was present on multiple proximal axonal segments of all control BCs (4/4 fully reconstructed axons, on average 2.8% ± 1.2% myelination). In contrast, none of the BCs from cuprizone-treated mice showed myelinated segments (0/6 axons). Furthermore, the total number of axon segments (~80 per axon, Mann–Whitney test p=0.3032, **Figure 2f**) as well as the total path length were unaffected by cuprizone treatment (on average ~4.5 mm in both groups, range 2.0–9.5 mm, Mann–Whitney test p=0.9871, **Figure 2g, Figure 2 – figure supplement 1c-f**).

To examine whether myelin loss changes the intrinsic excitability of PV$^+$ BCs, we made whole-cell recordings in slices from PV-Cre; Ai14 mice (**Figure 2h**). Recording of steady-state firing properties by injecting increasing steps of currents injections revealed an increase in the rheobase current (~90 pA, **Figure 2i, j**) and an ~50 Hz reduced firing frequency during low-amplitude current injections (two-way ANOVA, treatment p=0.0441, Šidák's multiple comparisons post hoc test at 200 pA; p=0.0382, 250 pA; p=0.0058, 300 pA; p=0.0085) without a change in the maximum instantaneous firing rate (two-way ANOVA, Šidák's multiple comparisons post hoc test, p=0.92, data not shown). However, neither the AP half-width (control, 290 ± 10 µs, n = 34 cells from 12 mice vs. cuprizone, 295 ± 10 µs, n = 15 cells from 7 mice, two-tailed Mann–Whitney U-test p=0.7113) nor AP amplitude was affected by cuprizone treatment (control 78.12 ± 1.66 mV, n = 34 cells from 12 mice vs. cuprizone, 80.13 ± 2.48 mV, n = 15 cells from 7 mice, p=0.4358). In contrast, the resting membrane potential (VRMP) of PV$^+$ interneurons was on average ~4 mV significantly more hyperpolarized (**Figure 2k**) without a change in the apparent input resistance (control, 133.3 ± 8.55 MΩ, n = 42 cells from 21 mice vs. cuprizone 125 ± 8.96 MΩ, 27 cells out of 13 mice, p=0.5952). In addition to the hyperpolarization in VRMP, demyelinated PV$^+$ interneurons also had an ~3 mV more hyperpolarized AP voltage threshold (control, –40.51 ± 0.97 mV, n = 34 cells from 12 mice) and cuprizone –43.65 ± 1.29 (n = 15 cells from 7 mice, Mann–Whitney test p=0.0269). Taken together, the results indicate that cuprizone treatment completely demyelinates proximal branches of PV$^+$ interneuron axons, and while not affecting axon morphology, causes a net decrease in the intrinsic PV$^+$ interneuron excitability.

Is myelin required for PV$^+$ BC-mediated inhibition? Single PV$^+$ BCs typically make 5–15 synapses with a PN in a range of <200 µm, forming highly reliable, fast, and synchronized release sites[5,14,21,38]. Intercellular variations in both myelin distribution and aberrant myelin patterns have been associated with conduction velocity changes[21,24]. To examine the role of myelin on inhibitory transmission, we made paired recordings of PV$^+$ BCs and L5 PNs with and without myelination, in control or cuprizone-treated PV-Cre; Ai14 mice, respectively (**Figure 3**). We evoked APs in PV$^+$ BCs while recording unitary inhibitory postsynaptic currents (uIPSCs) under conditions of physiological Ca^{2+}/ Mg^{2+} (2.0/1.0 mM in n = 78 pairs, **Figure 3a, b**). Concordant with optogenetic mapping of PV$^+$ inputs onto L5 PNs in mouse S1 (Packer and Yuste, 2011), in control slices the probability of a given PV$^+$ cell being connected to a nearby PN was high (~0.48, **Figure 3c**). In contrast, the connection probability was significantly lower in cuprizone-treated mice (~0.23, p=0.0182, **Figure 3b, c**). In 13 stable connected pairs, we examined unitary IPSC properties including failure rate and amplitude, as well as rise- and decay time, using automated fits of the uIPSCs (n > 80 trials per

connection, **Figure 3d**). Cuprizone treatment led to a significant increase in the number of failures (from 0.05 to 0.26, **Figure 3e**) and an ~2.5-fold reduction in the average uIPSC peak amplitude (**Figure 3f**). To obtain an estimate of propagation speed, we determined on successful trials the latency between the AP peak and uIPSCs at 10% peak amplitude (**Figure 3d**). Interestingly, both the mean latency and the trial-to-trial latency variability remained unchanged (average ~800 µs; Mann–Whitney test p>0.999; SD in cuprizone 319 ± 65 µs, n = 7 pairs, SD in control, 276 ± 38 µs, n = 5 pairs, p>0.60, **Figure 3g**).
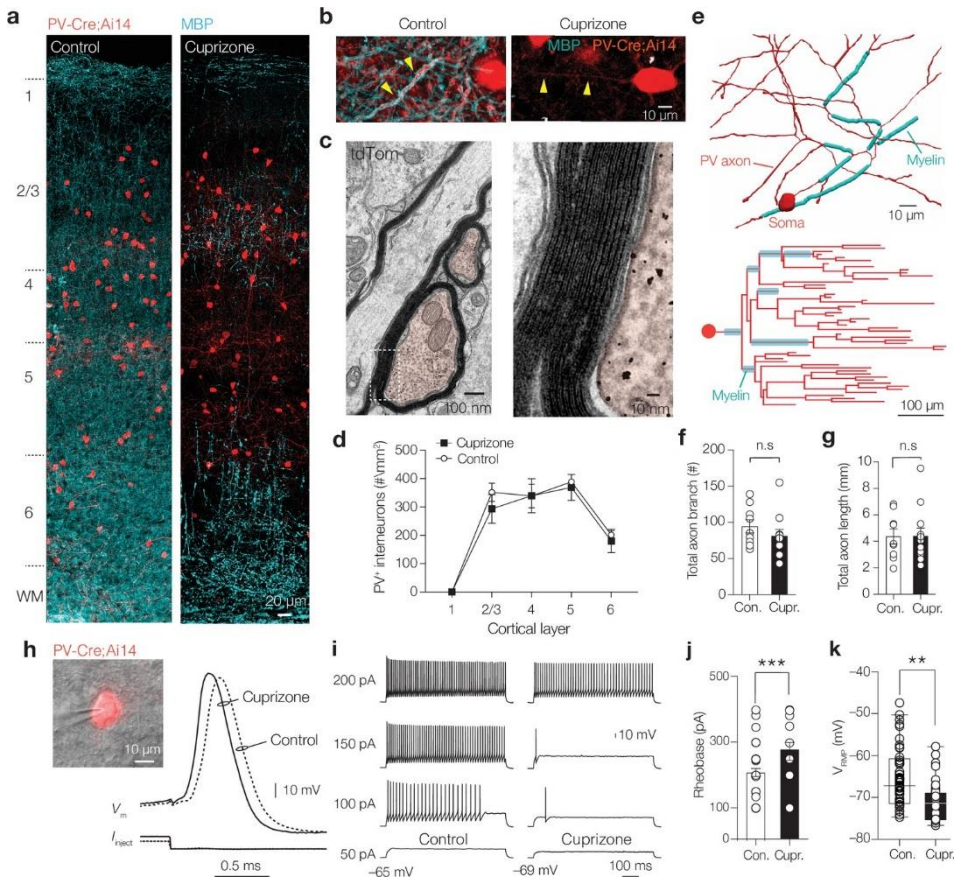
Figure 2. Demyelination preserves parvalbumin-positive (PV⁺) interneuron number and morphology but reduces excitability. a) Left: confocal z-projected overview image of S1 in a PV-Cre; Ai14 mouse (tdTomato⁺, red) overlaid with myelin basic protein (MBP, cyan). Right: overview image showing loss of MBP after + weeks cuprizone. **b**) Myelinated PV⁺ axons in control (left) and PV⁺ axons demyelination with cuprizone treatment (right). **c**) Electron microscopy (EM) of transverse cut tdTomato⁺ immunogold-labeled axons (false-colored red). Right: higher magnification of immunogold particles and ultrastructure of the PV interneuron myelin sheath. **d**)

140

PV[+] interneuron number across the cortical lamina was not affected by cuprizone treatment (two-way ANOVA, treatment effect p=0.6240). **e**) Top: example of a high-resolution 3D reconstruction of a biocytin-labeled PV axon (red) labeled with MBP (cyan) of a control mouse, showing the first approximately six axonal branch orders. Bottom: control axonogram showing axon branch order and myelinated segments (cyan). **f, g**) Total axon branch number and length are not changed by demyelination (Mann–Whitney tests p=0.3032 and p=0.8822, respectively). n.s., not significant. **h**) Left: brightfield/fluorescence overlay showing patch-clamp recording from a tdTomato[+] interneuron. Right: example PV[+] interneuron APs from control (dotted line) and cuprizone-treated mice (continuous lines). **i**) Steady-state sub- and suprathreshold voltage responses during 700 ms current injections. Firing rates near threshold reduced and the **j**) rheobase current significantly increased in cuprizone (***p=0.0003). **k**) PV^{+} basket cells (BCs) showed an ~4 mV hyperpolarized resting membrane potential (**p=0.0036). Data shown as mean ± SEM and open circles individual cells.

To further examine the properties of GABA release in demyelinated PV-BCs, we recorded uIPSCs during a train of five APs at 100 Hz (averaging >50 trials, **Figure 3h**). Consistent with the temporary facilitation in IPSCs of adult Purkinje cells[39], uIPSC recordings in control PV BCs showed that paired-pulse ratios were on the second spike facilitated by 20% (uIPSC2/uIPSC1 1.20 ± 0.060) and gradually depressed on the subsequent spikes (spikes 3–5). In contrast, in cuprizone-treated mice uIPSCs were depressed during the second and subsequent pulses (two-way repeated-measures ANOVA pulse × treatment effect p<0.021, Šidák's multiple comparisons tests for uIPSC2/uIPSC1 0.89 ± 0.041, p=0.0339, **Figure 3h**).

The uIPSC failures and impairment of temporary facilitation may reflect failure of AP propagation along demyelinated PV axons, changes in the GABA release probability or a lower number of active release sites (<5[5,14]). To further examine the properties of inhibition at L5 PNs, we recorded miniature inhibitory postsynaptic currents (mIPSCs). In line with the uIPSC findings, the results showed that mIPSCs were significantly reduced in peak amplitude (from ~20 to ~7 pA, p=0.002) without a change in frequency (**Figure 3 – figure supplement 1c**). Furthermore, using PV immunofluorescence staining with biocytin-filled L5 PNs the number of PV[+] puncta was 40% reduced both at the soma and the primary apical dendrite, correlating with the overall reduction in immunofluorescent signals in cuprizone treatment (**Figure 3 – figure supplement 1g – i**). Interestingly, in contrast to the loss of perisomatic PV[+] BC puncta, putative PV[+] chandelier cell inputs, identified by co-staining with the AIS marker ßIV-spectrin, were preserved (~8 puncta/AIS, Mann–Whitney test p=0.96, **Figure 3 – figure supplement 2**). Furthermore, staining for Syt2, a Ca2^{+} sensor protein selective for PV[+] presynaptic terminals[12,40] confirmed an ~35% reduction (**Figure 3 – figure supplement 3a, b**). Together with the reduction in uIPSC peak amplitudes (**Figure 3f**), these data suggest that cuprizone-induced demyelination causes a loss of presynaptic

PV[+] terminal sites. Interestingly, Syt2^{+} puncta analysis in the dysmyelinated shiverer mouse line also showed a reduced number of Syt2^{+} puncta at L5 PN somata and a reduced frequency of mIPSCs (p=0.019, **Figure 3 – figure supplement 3c-g**), indicating that compact myelin is not only required for maintaining PV[+] interneuron inputs but also for PV[+] BC presynaptic terminal development.

Cuprizone treatment did not affect PV[+] axon length (**Figure 2 – figure supplement 1f**), suggesting that the density of presynaptic terminals should be reduced. To test this idea, we performed Syt2 immunolabeling of individually biocytin-filled PV[+] BCs (**Figure 3i**). Consistent with the hypothesis, cuprizone treatment significantly reduced the density of Syt2^{+} puncta by twofold (cuprizone, ~1 Syt2^{+} puncta per 10 μm vs. 1 Syt2^{+} puncta per 5 μm in control, Mann–Whitney test p<0.0001, **Figure 3j, k**). Interestingly, recordings of miniature excitatory postsynaptic currents (mEPSCs) from PV[+] interneurons of control and cuprizone-treated mice showed no changes in peak amplitude nor frequency (**Figure 3 – figure supplement 4**), in keeping with the preservation of excitatory inputs onto L5 PNs following cuprizone-induced demyelination[29] and suggesting that myelin loss has a significant impact on inhibitory synapse stabilization and maintenance.
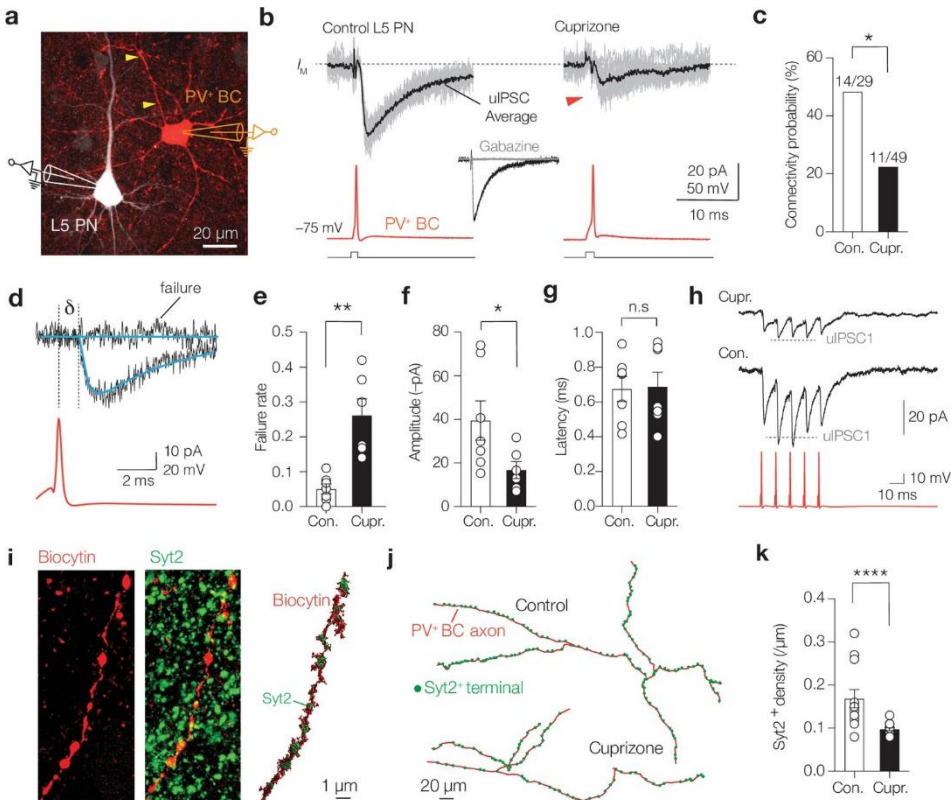
Figure 3. Demyelination decreases connectivity, reliability, and rapid facilitation of parvalbumin-positive (PV⁺) unitary inhibitory postsynaptic currents (uIPSCs). a) Immunofluorescence image of a connected control PV⁺ basket cell (BC) (red) and layer 5 (L5) pyramidal neuron (PN) (white). **b**) Example traces of 10 single-trial uIPSC traces (gray) overlaid with mean average (>60 trials, black). Inset: uIPSCs abolished by gabazine (GABA$_A$ blocker, 4 µM). **c**) Cuprizone-treated mice show significantly lower connection probability between PV⁺ BC and L5-PN (chi-square test *p=0.0182, n = 78 pairs). **d**) Example fits (blue) of uIPSCs for rise- and decay time, amplitude, failure rate, amplitude, and latency analyses (δ, AP to 10% uIPSC peak amplitude). **e**) Cuprizone increased failures by fivefold and the average peak amplitude by ~2.5-fold (Mann–Whitney test **p=0.012) and **f**) reduces the mean amplitude (Mann–Whitney test *p=0.0256). **g**) uIPSCs latency remained unchanged (Mann–Whitney test n.s., p>0.999). **h**) Cuprizone impairs short-term facilitation. Dotted line indicates expected amplitude for uIPSC$_2$ (scaled from uIPSC$_1$). **i**) Left: confocal z-projected image of a control PV⁺ axon (red) immunostained with Syt2 (green). Right: surface-rendered 3D image of the same axon. **j**) Example sections of 3D reconstructions. **k**) Cuprizone increased the Syt2⁺ puncta spacing by approximately twofold (Mann–Whitney test ****p<0.0001, n = 12). Data shown as mean ± SEM and open circles individual axons or pairs. n.s., not significant.

Thus, myelin loss reduces the number of presynaptic sites, causing an increase of GABA release failures and a frequency-dependent depression, ultimately limiting the fast component of BC to PN inhibitory transmission.

PV+ activation rescues interictal spikes and theta oscillations, but not the loss of gamma

To understand how myelin deficits and loss of fast PV-mediated inhibition of PNs impacts network dynamics, we used AAV1-mediated delivery of Cre-dependent channelrhodopsin-2 (ChR2) into L5 of PV-Cre; Ai14 mice (**Figure 4a**). The ChR2 transduction rate was comparable between control and cuprizone mice (~70%, **Figure 4b, c**). In acute slices, we voltage-clamped L5 PNs and optogenetically evoked IPSC (oIPSC) with full-field blue light illumination (**Figure 4d**). Consistent with S1 L5 PNs receiving converging input from >100 PV⁺ interneurons[38], control oIPSCs rapidly facilitated to a peak amplitude of ~700 pA followed by rapid synaptic depression (**Figure 4f, g**). In slices from cuprizone mice, however, the oIPSC peak amplitude was significantly reduced (approximately twofold) while neither the steady-state amplitude during vesicle replenishment nor the total charge transfer reached a significant difference (control, –99.58 ± 28.5 pC vs. cuprizone, –54.3 ± 20.57 pC, p=0.236, n = 9 control and n = 8 cuprizone neurons, **Figure 4f, h**).
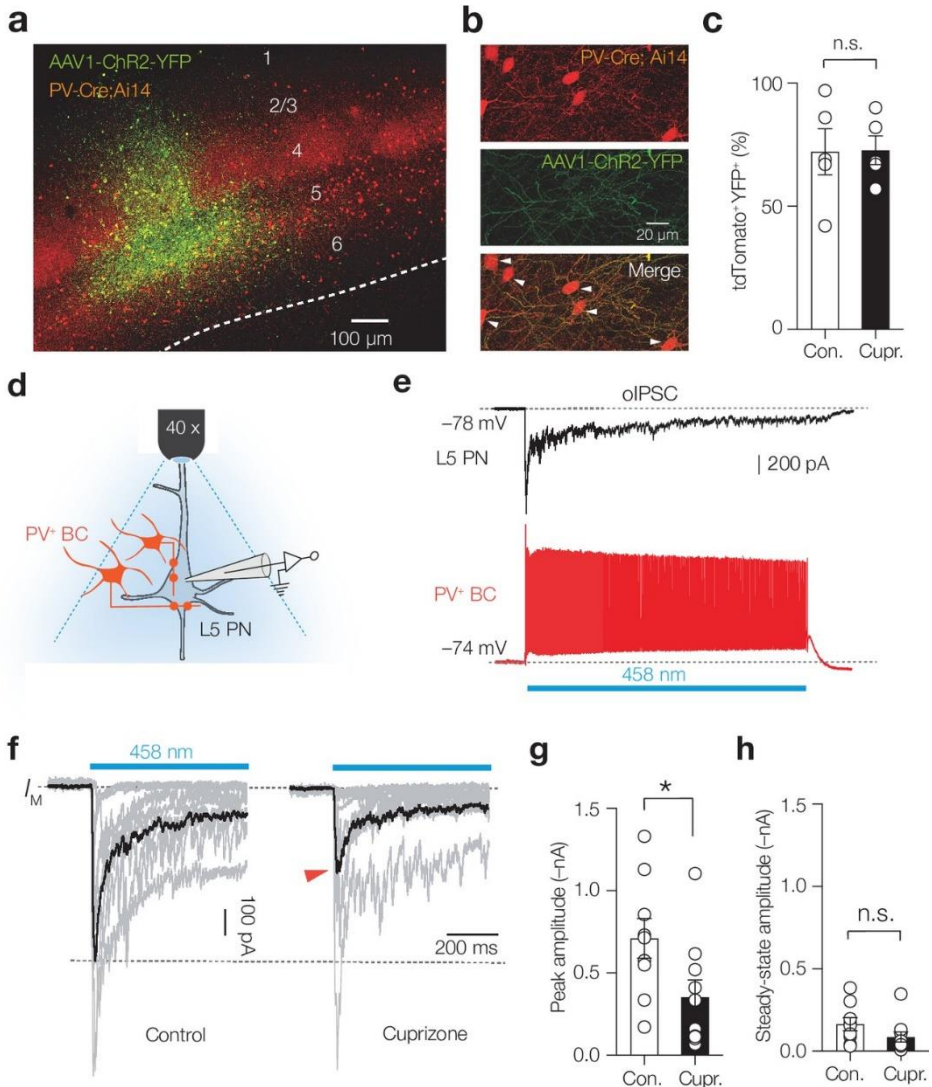
Figure 4. Demyelination impairs phasic parvalbumin-positive (PV+) basket cell (BC) inhibition of layer 5 (L5) pyramidal neurons (PNs). a) Immunofluorescent image of AAV1-hChR2-YFP expression (green) injected into L5 of S1. **b**) Confocal images of separate fluorescent channels showing td-Tomato+ cell bodies and neurites (red, top), the localization of AAV1-hChR2-YFP (green, middle), and the merge image (bottom). The majority of tdTomato+ cells were YFP+ (white arrows). **c**) Average transfection rate of AAV1-hChR2-YFP in the L5 (>70%) is comparable in control and cuprizone conditions (Mann–Whitney test p=0.889, n = 5). **d**) Schematic showing full-field blue light optogenetically evoked postsynaptic inhibitory currents (oIPSCs) in L5 PNs. **e**) Example trace of a whole-cell current-clamp recording from a PV+ interneurons (bottom red) compared to a separate whole-cell voltage-clamp recordings from an L5 PN. A 1 s blue light field illumination (blue bar) produces sustained firing in *PV-Cre AAV1-ChR2* interneurons. **f**) Single trial oIPSCs (gray) from different experiments (1 s duration pulses) overlaid with the average oIPSC

(black) revealing a lower peak amplitude in cuprizone (red arrow). **g**) Population data revealed an approximately twofold reduction in oIPSCs' peak amplitude (Mann–Whitney test p=0.0172). **h**) Steady-state oIPSCs' amplitude did not reach significance, n.s., Mann–Whitney test p=0.0789.

Impaired phasic PV[+] interneuron-mediated inhibition predicts a disrupted γ-rhythm. Experimental and computational studies show that in most cortical areas γ-rhythms are strongly shaped by electrically and synaptically coupled PV[+] interneurons, which, by temporally synchronizing firing rates, synaptic inhibitory time constants ($\cong$ 9 ms), and the recurrent excitatory feedback from PNs, give rise to network resonance in the 30–80 Hz bandwidth[3,7,26,41,42]. To test the cellular and circuit properties of the γ-rhythm, we examined the extent of evoked γ-modulation by leveraging optogenetic activation of PV[+] interneurons with AAV1-hChR2-YFP and introducing a laser fiber into L5 and recording the LFP (**Figure 5a**). Evoking brief pulses of blue light (1 ms at a low gamma frequency of 30 Hz) showed that local circuit currents were modulated and highly phase-locked in slices from control mice (bandpass filter 25 and 40 Hz, **Figure 5b, c, Figure 5 – figure supplement 1**). In striking contrast, no modulation or entrainment was observed in cuprizone-treated mice, neither when using high laser power (up to 6.5 mW, **Figure 5b – e, Figure 5 – figure supplement 1**).

Could the diminished PV[+] BC activity cause the emergence of θ rhythm and interictal spikes during quiet behavioral states of wakefulness? To test the direct contribution of PV[+] BCs, we activated ChR2 for 1 s duration pulses in PV-Cre; Ai14 mice to generate tonic GABA release (**Figure 6a**). In cuprizone-treated mice, we found that optically driving PV[+] interneurons normalized the LFP power in the θ band to control levels, without affecting δ, β, and γ rhythms (two-way ANOVA treatment × light p=0.0124, Šidák's multiple comparisons tests in cuprizone, light on vs. off; for δ, p=0.9975; θ, p=0.0076; β, p=0.9481; γ, p=0.9998, **Figure 6a – c, Source data 1**). Furthermore, activation of blue light significantly reduced the frequency of interictal epileptic discharge frequency (p=0.0089, **Figure 6d, e , Figure 6**). The normalization of cortical rhythms by elevating sustained PV[+]-mediated activity suggests that GABAA receptors are insufficiently activated in the demyelinated cortex. Finally, to directly examine the role of GABAA receptors agonism in dampening global interictal spikes we administered a nonsedative dose of diazepam (2 mg/kg i.p.), an allosteric modulator of postsynaptic GABAA receptors, in cuprizone-treated mice (7-week treatment). The results showed that diazepam significantly suppressed the interictal epileptiform discharges in cuprizone mice, indicating a prominent role of GABA in the deficits of circuit excitability (**Figure 6f, Figure 6 – figure supplement 1**).
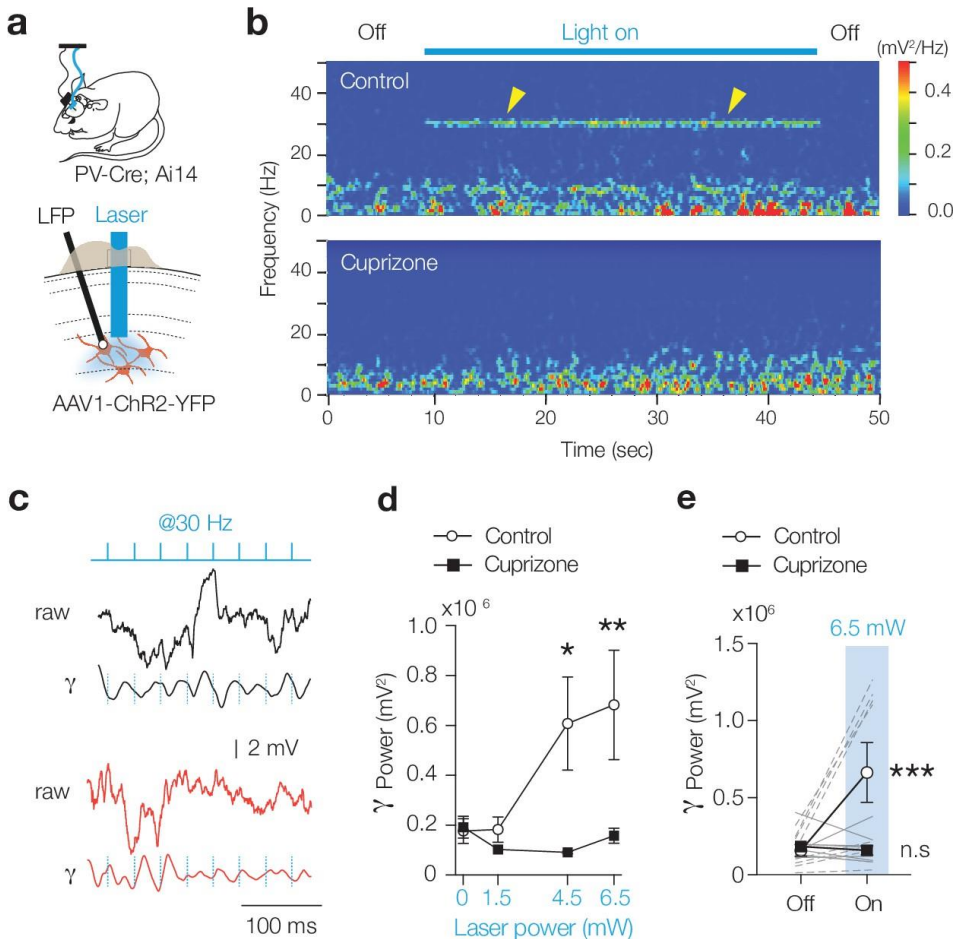
Figure 5. Demyelination impairs optogenetically evoked γ entrainment. a) Schematic for chronic local field potential (LFP) recordings and in vivo optogenetic stimulation in freely moving PV-Cre; Ai14 mice. **b**) Time frequency plot showing low gamma frequency (γ) entrainment (40 blue light pulses of 1 ms duration at 30 Hz) in control but not in cuprizone mice. **c**) Raw LFP (top) and bandpass-filtered trace (25–40 Hz, bottom) from control and cuprizone during low-γ entrainment. **i**) Population data of γ power with increasing laser power reveals impaired γ in cuprizone-treated mice. **d**) Myelin-deficient mice low-γ band entrainment to optogenetic stimuli (two-way ANOVA followed by Šidák's multiple comparisons cuprizone vs. control, 0 mW, p>0.999; 1.5 mW, p=0.979; 4.5 mW, *p=0.0221, 6.5 mW, **p=0.0046). **e**) Data are shown as mean ± SEM with gray lines individual cells, gray lines individual mice. n.s., not significant.
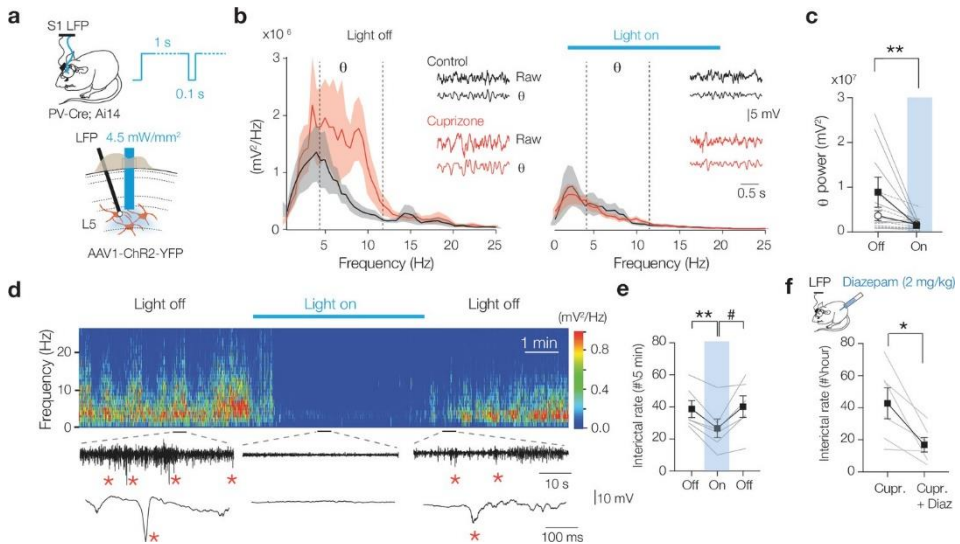
Figure 6. Optogenetic activation of myelin-deficient parvalbumin-positive (PV⁺) interneurons rescues theta rhythm and interictal epileptiform discharges. a) Schematic drawing for chronic local field potential (LFP) and optogenetic stimulation in freely moving mice. A 1 s blue light pulse with 100 ms off periods activated PV⁺ interneurons. Blue light was switched on during high interictal activity (>10 spikes/min). **b**) Power spectral content collected from 2 s epoch windows in control (black) and cuprizone (red) before (left) and during 3 min (right) optogenetic activation of PV⁺ interneurons. Insets: raw LFP signals (top) and θ content (bottom) in control (black) and cuprizone (red) condition. **c**) Population data showing optogenetic activation of PV⁺ cells attenuated the amplified θ frequency in cuprizone mice to control levels (Šidák's multiple comparisons test in cuprizone, light on vs. light off for θ, **p=0.0076). **d**) Example time frequency plot (top) and raw LFP traces (below) showing suppression of interictal spikes during light on conditions. **e**) Population data of transient optogenetic suppression of the interictal activity in 8-week cuprizone-treated mice (one-way ANOVA p=0.0165, Tukey's multiple comparisons tests; off vs. on, **p=0.0089; on vs. off, p=0.0539; off vs. off, p=0.928). **f**) 2 mg/kg i.p. injection of diazepam in cuprizone-treated mice reduces interictal rate for at least 10 hr (two-tailed Student's *t*-test *p=0.024). Data shown as mean ± SEM and gray lines individual mice.

Discussion

In this study, we identified that the cellular microarchitecture of myelination of PV+ BCs is required for stimulus-induced fast gamma frequencies, limiting the power of slow cortical oscillations and interictal spikes during quiet wakefulness. Interictal discharges identified as spikes on the EEG are an important diagnostic criterium in epilepsy and reflect hypersynchronized burst firing of PNs and interneurons[31,34,43]. The brief episodic and generalized nature of ECoG spikes we recorded in both demyelinated and dysmyelinated cortex (~50–500 ms in duration and ~1/min) resemble interictal spikes reported in epilepsy models[43,44] and are concordant with recordings in the

hippocampus of cuprizone-treated mice by Hoffmann et al., 2008[33]. Here, we fundamentally extend the insights into interictal spikes by showing their spatiotemporal synchronization across cortical areas and hemispheres and a selective manifestation during the vigilance state of quiet wakefulness. During brain states of quiescence, for example, when whiskers are not moving, whole-cell in vivo recordings in the barrel cortex reveal low-frequency (<10 Hz) highly synchronized membrane potential fluctuations of PNs and interneurons, during which fast-spiking PV+ interneurons are dominating action potential firing[45,46]. Consistent with the state-dependent increased activity of cortical interneuron firing, we found a selective amplification of the LFP theta power during quiet wakefulness, which may be explained by the reduced intrinsic excitability of PV+ BCs and deficiency of fast inhibitory transmission in the demyelinated cortex (**Figures 2** and **3**). In support of this conjecture, optogenetic inhibition of PV+ interneurons in the normally myelinated cortex is sufficient to increase PN firing rates, elevating the power of slow oscillations and triggering epileptiform activity[9,27,37]. While our optogenetic activation of demyelinated PV+ BCs normalized the power in the theta bandwidth, these interneurons are not critical for generating theta[7,26]. Physiological theta oscillations are strongly driven by the long-range corticothalamic circuitry and cortical PN firing during non-rapid eye movement (NREM), also called thalamocortical spindles[47]. Interestingly, recordings in epilepsy patients showed that interictal discharges occur frequently during NREM sleep stages and coupled with the spindle activity[48,49]. Whether interictal spike-spindle coupling occurs in cuprizone-treated mice or specific sleep stages are affected is not known, but the present results warrant investigation of the corticothalamic loop in the generation of interictal discharges during demyelination.

A major limitation of the experimental toolbox available to experimentally study myelination is the lack of axon- or cell-type selectivity. Whether amplified theta- and abolished gamma-frequency oscillations are the consequence of PV+ axon demyelination, the loss of excitatory axon myelination or the combination thereof, remains to be further examined when more refined genetic or molecular methods become available to interrogate oligodendroglial myelination of specific cell types. In the absence of such strategies, however, our in vivo experiments optogenetically driving selectively PV+ interneurons or activating GABAA receptors (**Figure 5**) uncover important converging evidence for a role of interneurons in the amplification and synchronization of slow oscillations and epileptic discharges. Interestingly, while tonically driving action potential firing in myelin-deficient PV+ interneurons with optogenetic activation was able to rescue theta hypersynchrony, using a 30 Hz stimulation regime failed to entrain the LFP in the low-gamma frequency. This may suggest that for gamma, precisely timed spike generation of PV+ BCs alone is

insufficient and may require in addition synchronized inhibitory synaptic transmission, which is selectively reduced in demyelinated PV[+] BCs. Alternatively, a specific circuit connectivity or presynaptic GABA release dynamics may be lost in cuprizone-treated mice. In future studies, the role of myelination could be further examined by exploring whether remyelination restores the ability of PV[+] interneurons to modulate gamma oscillations.

Myelination of PV+ axons determines synapse assembly and maintenance

The requirement of myelination of PV[+] BCs to generate gamma rhythms is surprising in view of its sparse distribution in patches of ~25 μm across <5% of the total axon length[15,21,50] (**Figure 2, Figure 2 – figure supplement 1**). The sparseness of interneuron myelination previously raised the question whether myelin speeds conduction velocity in these axon types[15,50,51]. In a genetic mouse model with aberrant myelin patterns along fast-spiking interneuron axons, the inferred conduction velocity was reduced[24]. In contrast, we found that the average uIPSC latency (~800 μs) in completely demyelinated axons was normal and well within the range of previous paired recordings between myelinated PV[+] BC and PNs (700–900 μs[52,53]). Assuming a typical axonal path length of ~200 μm between the AIS and presynaptic terminals connected with a PN, combined with an ~250 μs delay for transmitter release, the calculated conduction velocity would be 0.4 m/s, consistent with optically recorded velocities in these axons (~0.5 m/s[54]). Our paired recordings, made near physiological temperature (34–36°C), may have had a limited resolution to detect temporal differences and are not excluding changes in the order of microseconds. To study submillicecond changes, it may be necessary to employ simultaneous somatic and axonal whole-cell recording[55] and/or high-resolution anatomical analysis of myelin along the axon path, which recently showed a small albeit positive correlation between percentage of myelination and conduction velocity[21]. Furthermore, conduction velocity tuning by myelination of GABAergic axons may become more readily apparent for long-range projections. Another constraint of the present study is the lack of information on the nodes of Ranvier along demyelinated PV[+] BC axons. Aberrant interneuron myelin development, causing myelination of branch points, impairs the formation of nodes of Ranvier[24]. Reorganization of nodal voltage-gated ion channel clustering also occurs with the loss of myelin or oligodendroglial-secreting factors causing deficits in action potential propagation[56,57]. How PV[+] BC interneuron myelin loss changes the nodal ion channel distribution remains to be examined.

Converging evidence from the two distinct models (shiverer and cuprizone) showed that interneuron myelination critically determines PV[+] release site number, dynamics, and connection probability (**Figure 3, Figure 3 – figure supplement 3**), concordant

with the observed synapse loss in Purkinje axons of the les rat[23]. The molecular mechanisms how compact myelination of proximal axonal segments establishes and maintains GABAergic terminals in the higher-order distal axon collaterals are not known but may relate to its role in supplying metabolites to the axon[58]. The PV[+] interneuron myelin sheath contains high levels of noncompact 2′,3′-cyclic nucleotide 3′-phosphodiesterase (CNP) protein[15,59], which is part of the inner cytoplasmic inner mesaxon[60]. In the absence of inner cytoplasmic loops of oligodendroglial myelin the interneuron axons may lack sufficient trophic support to maintain GABAergic presynaptic terminals. Another possibility is pruning of the presynaptic terminals by microglia[61-63]. Microglia become increasingly activated during sub-demyelinating stages within the first week of cuprizone treatment[64,65] and in aged Mbp[+]/– mice[66]. In future studies, it needs to be examined whether attenuation of microglia activation could protect against PV[+] synapse loss and interictal epileptiform discharges.

Implications for cognitive impairments in gray matter diseases

The identification of a cellular mechanism for interictal spikes may shed light on the role of PV[+] axon myelination in cognitive impairments in MS[67] and possibly other neurological disorders. In preclinical models of epilepsy and epilepsy patients, interictal spikes have been closely linked to disruptions of the normal physiological oscillatory dynamics such as ripples required to encode and retrieve memories[31,44,68,69]. Interictal epileptic discharges are also observed in other neurodegenerative diseases, including Alzheimer[70]. Notably, reduced gray matter myelination and oligodendroglia disruption are reported in multiple epilepsy models and recently in Alzheimer[71,72]. Therefore, the cellular and circuit functions controlled by PV[+] interneurons may represent a common mechanism for memory impairments in neurological disease encompassing myelin pathology. In support of this idea, neuropathological studies in MS show a specific loss of PV[+] interneuron synapses in both cortex and hippocampus[63,73]. In MS patients, increased connectivity and synchronization in delta and theta band rhythms during resting state or task-related behavior have been reported[74,75] and low GABA levels in sensorimotor and hippocampal areas are correlated with impairments of information processing speed and memory[76,77]. Taken together with the present work, promoting PV[+] interneuron myelination, and thereby strengthening fast inhibition, may provide important new therapeutic avenues to improve cognition.

Materials and methods

Key Resources Table				
Reagent type (species) or resource	**Designation**	**Source or reference**	**Identifiers**	**Additional information**
strain, strain background (*Mus musculus* male/female)	C57BL6	Janvier Labs	Cat# 2670020, RRID:MGI:2670020	
strain, strain background (*Mus musculus* male/female)	B6;129P2-*Pvalb*$^{tm1(cre)Arbr}$/J	Jackson laboratories	Stock No: 008069 RRID:IMSR_JAX:008069	
strain, strain background (*Mus musculus* male/female)	B6;129S6-*Gt(ROSA)26Sor*$^{tm14(CAG-tdTomato)Hze}$/J	Jackson laboratories	Stock No: 007908 RRID:IMSR_JAX:007908	
strain, strain background (*Mus musculus* male/female)	C3Fe.SWV-*Mbp*^{shi}/J	Jackson laboratories	Stock No: 001428 RRID:IMSR_JAX:001428	
Transfected construct (*Mus musculus*)	pAAV-EF1a-double-floxed-hChR2(H134)-EYFP-WPRE-HGHpA	Addgene.org	#20298 RRID:Addgene_20298	
antibody	Rabbit monoclonal, anti-MBP	Santa Cruz	Cat# sc-13564, RRID:AB_675707	(1:300)
antibody	Mouse monoclonal, anti-PV	Swant	Cat#: 235 RRID:AB_10000343	(1:1000)
antibody	Rabbit polyclonal, anti-syt2	Synaptic Systems	Cat# 105 223, RRID:AB_10894084	(1:500)
antibody	Rabbit polyclonal, anti-ßIV-spectrin	M. Ransband (BCM)	N/A	(1:200)
peptide, recombinant protein	Alexa 488 - streptavidin	Thermofisher	Cat#: S32354 RRID:AB_2315383	(1:500)
peptide, recombinant protein	Alexa 633-streptavidin	Thermofisher	Cat#: S21375 RRID:AB_2313500	(1:500)
chemical compound, drug	Bis(cyclohexanone)oxaldihydrazone	Merck	Cat#: C9012	
chemical compound, drug	Diazepam	Centrafarm Nederland B.V	Cat#: RVG56691	
chemical compound, drug	Biocytin	Sigma	Cat#: B4261	

chemical compound, drug	D-AP5	HelloBio	Cat#: 0225	
chemical compound, drug	Gabazine	Sigma	Cat#: S106	
chemical compound, drug	CNQX	HelloBio	Cat#: HB0205	
chemical compound, drug	Tetrodotoxin (TTX) citrate	Tocris	Cat#: 1069	
software, algorithm	Neurolucida 360 Neurolucida Explorer	MBF Bioscience	V2018.02 RRID:SCR_001775	
software, algorithm	Synaptic puncta quantification	FIJI (ImageJ)	V2.0, V.2.0.0-rc-65/1.5w RRID:SCR_002285	
software, algorithm	Neuroarchiver tool	Open source Instruments Dubey et al., 2018	LWDAQ_8.5.29	
software, algorithm	Igor pro 8	WaveMetrics	V8.04 RRID:SCR_000325	
software, algorithm	Axograph	Axograph	RRID:SCR_014284	
software, algorithm	GraphPad	Prism 8 and 9	RRID:SCR_002798	
software, algorithm	SP8 X (DM6000 CFS)	Leica application Suite	AF v3.2.1.9702 RRID:SCR_013673	
other	Electrode (90% Pt, 10% Ir)	Science Products	Cat#: 101R-5T	
other	Optical fiber	Thorlabs	Cat#: FP200URT	
other	Ceramic ferrule	Thorlabs	Cat#: CFLC230-10	
other	Fiber coupled blue laser	Shanghai Laser & Optics Co.	Cat#: 473 nm, DPSS Laser with fiber coupled (T3)	
other	Cyclops LED driver	Open-ephys.org	Cat#: Cyclops LED driver 3.7	
other	Patch-clamp amplifier	Dagan Corporates	BVC-700A	
other	Patch-clamp amplifier	Molecular device	Axon Axopatch 200B	
other	In-vivo multichannel systems (Portable-ME-systems) amplifier	Multi channels systems	ME16-FAO-uPA	

Animals

We crossed PvalbCre mice (B6;129P2-Pvalbtm1(cre)Arbr/J, stock no: 008069, Jackson Laboratory, RRID:IMSR_JAX:008069) with the Ai14 Cre reporter line B6;129S6-

Gt(ROSA)26Sortm14(CAG-tdTomato)Hze/J (stock no: 007908, Jackson Laboratory, RRID:IMSR_JAX:007908). For other experiments, we used C57BL/6 mice (Janvier Labs, Saint-Berthevin Cedex, France, RRID:MGI:2670020). Shiverer mice were obtained from Jackson (C3Fe.SWV-Mbpshi/J, stock no: 001428, RRID:IMSR_JAX:001428) and backcrossed with C57BL/6 mice for >10 generations. All mice were kept on a 12:12 hr light-dark cycle (lights on at 07:00, lights off at 19:00) with ad libitum food and water. For cuprizone treatment, either PV-Cre; Ai14 or C57BL/6 male or female mice, from 7 to 9 weeks of age, were fed ad libitum with normal chow food (control group) or were provided 0.2% (w/w) cuprizone (Bis(cyclohexanone)oxaldihydrazone, C9012, Merck) added either to grinded powder food or to freshly prepared food pellets (cuprizone group). Cuprizone-containing food was freshly prepared during every second or third day for the entire duration of the treatment (6–9 weeks). The average maximum weight loss during cuprizone feeding was ~11% (n = 31). All animal experiments were done in compliance with the European Communities Council Directive 2010/63/EU effective from 1 January 2013. The experimental design and ethics were evaluated and approved by the national committee of animal experiments (CCD, application number AVD 80100 2017 2426). The animal experimental protocols were designed to minimize suffering and approved and monitored by the animal welfare body (IvD, protocol numbers NIN17.21.04, NIN18.21.02, NIN18.21.05, NIN19.21.04, and NIN20.21.02) of the Royal Netherlands Academy of Arts and Science (KNAW).

In vitro electrophysiology

Mice were briefly anesthetized with 3% isoflurane and decapitated or received a terminal dose of pentobarbital natrium (5 mg/kg) and were transcardially perfused with ice-cold artificial CSF (aCSF) of the composition (in mM): 125 NaCl, 3 KCl, 25 glucose, 25 NaHCO3, 1.25 Na2H2PO4, 1 CaCl2, 6 MgCl2, 1 kynurenic acid, saturated with 95% O2 and 5% CO2, pH 7.4. After decapitation, the brain was quickly removed from the skull and parasagittal sections (300 or 400 µm) containing the S1 cut in ice-cold aCSF (as above) using a vibratome (1200S, Leica Microsystems). After a recovery period for 30 min at 35°C, brain slices were stored at room temperature. For patch-clamp recordings, slices were transferred to an upright microscope (BX51WI, Olympus Nederland) equipped with oblique illumination optics (WI-OBCD; numerical aperture, 0.8). The microscope bath was perfused with oxygenated (95% O2, 5% CO2) aCSF consisting of the following (in mM): 125 NaCl, 3 KCl, 25 D-glucose, 25 NaHCO3, 1.25 Na2H2PO4, 2 CaCl2, and 1 MgCl2. L5 PNs were identified by their typical large triangular shape in the infragranular layers and in slices from PV-Cre; Ai14 mice the PV⁺ interneurons expressing tdTomato were identified using X-Cite series 120Q (Excelitas) with a bandpass filter (excitation maximum 554 nm, emission maximum 581

nm). Somatic whole-cell current-clamp recordings were made with a bridge current-clamp amplifier (BVC-700A, Dagan Corporation, USA) using patch pipettes (4–6 MΩ) filled with a solution containing (in mM): 130 K-gluconate, 10 KCl, 4 Mg-ATP, 0.3 Na2-GTP, 10 HEPES, and 10 Na2-phosphocreatine, pH 7.4, adjusted with KOH, 280 mOsmol/kg, to which 10 mg/mL biocytin was added. Voltage was analog low-pass filtered at 10 kHz (Bessel) and digitally sampled at 50–100 kHz using an analog-to-digital converter (ITC-18, HEKA Electronic) and data acquisition software AxoGraph X (v.1.7.2, AxoGraph Scientific, RRID:SCR_014284). The access resistance was typically <20 MΩ and fully compensated for bridge balance and pipette capacitance. All reported membrane potentials were corrected for experimentally determined junction potential of –14 mV. Analysis for the electrophysiological properties includes PV^+ interneuron recordings from cells in normal ACSF and in the presence of CNQX and d-AP5 with high chloride intracellular solution (see below).

mIPSC and mEPSC recordings

Whole-cell voltage-clamp recordings were made with an Axopatch 200B amplifier (Molecular Devices). Patch pipettes with a tip resistance of 3–5 MΩ were pulled from thins wall borosilicate glass. During recording, a holding potential of –74 mV was used. Both the slow- and fast pipette capacitance compensation were applied, and series resistance compensated to ~80–90%. Patch pipettes were filled with high chloride solution containing (in mM) 70 K-gluconate, 70 KCl, 0.5 EGTA, 10 HEPES, 4 MgATP, 4 K-phosphocreatine, 0.4 GTP, pH 7.3 adjusted with KOH, 285 mOsmol/kg and IPSCs isolated by the presence of the glutamate receptor blockers 6-cyano-7-nitroquinoxaline-2,3-dione (CNQX, 20 µM), d-2-amino-5-phosphonovaleric acid (d-AP5, 50 µM) and the sodium (Na^+) channel blocker tetrodotoxin (TTX, 1 µM Tocris). Individual traces (5 s duration) were filtered with a high-pass filter of 0.2 Hz and decimated in AxoGraph software (RRID:SCR_014284). Chart recordings of mIPSCs were analyzed with a representative 30 ms IPSC template using the automatic event detection tool of AxoGraph. Detected events were aligned and averaged for further analysis of inter-event intervals (frequency) and peak amplitude. For mEPSC recordings from PV^+ interneurons, we filled patch pipettes with a solution containing (in mM) 130 K-gluconate, 10 KCl, 4 Mg- ATP, 0.3 Na2-GTP, 10 HEPES, and 10 Na2-phosphocreatine, pH 7.4, adjusted with KOH, 280 mOsmol/kg and both gabazine (4 µM) and TTX (1 µM) were added to the bath solution. The mEPSCs were analyzed using events detection tool in AxoGraph. The recorded signals were bandpass filter (0.1 Hz to 1 kHz) and recordings analyzed with a representative 30 ms EPSC template, after which selected EPSCs aligned and averaged for further analysis of inter-event intervals (frequency) and peak amplitude.

uIPSC recording and analysis

PV[+] interneurons (visually identified in PV-Cre; Ai14 mice based on tdTomato fluorescence expression) were targeted for whole-cell current-clamp recording within a radius of 50 µm from the edge of the L5 soma recorded in voltage-clamp configuration. APs in PV[+] interneurons were evoked with a brief current injection (1–3 ms duration) and uIPSCs recorded in the L5 PN from a holding potential of –74 mV. Only responses with 2× S.D. of baseline noise were considered being connected. Both fast and slow capacitances were fully compensated, series resistance compensation was applied to ~80–90%, and the current and voltage traces acquired at 50 kHz. For stable recordings with >50 uIPSCs, the episodes were temporally aligned to the AP and the uIPSCs were fit with a multiexponential function in Igor Pro. The curve fitting detected the baseline, uIPSC onset, rise time, peak amplitude, and decay time and was manually monitored. Fits were either accepted or rejected (e.g., when artifacts were present) and the number of uIPSC failures was noted for each recording.

In vitro optogenetics

50 nL of AAV1 particles (titer 1 × 1012 cfu/mL) produced from pAAV-EF1a-double-floxed-hChR2(H134)-EYFP-WPRE-HGHpA (Addgene.org #20298, RRID:Addgene_20298) was injected into L5 of S1 (coordinates from bregma; AP 0.15 mm, ML 0.30 mm, and DL 0.75 mm) of 6–9-week-old PV-Cre; Ai14 mice. About 7 days after the injection, a subset of mice was placed on 0.2% cuprizone diet for 8–9 weeks. PV[+] interneurons expressing hChR2 were identified using td-tom and YFP co-expression. Whole-cell voltage-clamp recordings were made from L5 PNs and oIPSCs were evoked with a X-cite 120Q, fluorescent lamp using filter BA460-510 (Olympus) in the presence of CNQX (50 µM) and dAP5 (20 µM) in the bath solution. The oIPSCs were evoked by illumination of large field with five light pulses of each 1 ms and 100 ms apart. Peak amplitude and area under the curve (charge) of oIPSC were quantified using AxoGraph. Only the first pulse was used for the quantification.

In vivo electrophysiology and automated event detection

Chronic ECoG and LFP recordings were performed using in-house-made electrodes of platinum-iridium wire (101R-5T, 90% Pt, 10% Ir, complete diameter of 200 µm with 127 µm metal diameter, Science Products). The perfluoroalkoxy alkanes (PFA)-coated wire platinum-iridium wire was only exposed at the tip to record the LFP. For placement of the recording electrode, animals were anesthetized with isoflurane (3%, flow rate 0.8 L/min with maintenance 1.5–1.8%, flow rate 0.6 L/min). A 1 cm midline sagittal incision was made starting above the interaural line and extending along the neck to create a

pocket for subcutaneous placement of the transmitter along the dorsal flank of the animal. The recording electrodes in each hemisphere (stereotaxic coordinates relative to bregma: S1; –0.15 mm anterior and ±0.30 mm lateral; for LFP; ventral 0.75 mm, V1; 0.40 mm anterior and ±0.30 mm lateral; for LFP; ventral 0.75 mm) and ground electrode (6 mm posterior and 1 mm lateral) were implanted subdurally through small holes drilled in the skull, held in place with stainless steel screws (A2-70, Jeveka), and subsequently sealed with dental cement. Mice were provided with Metachem analgesic (0.1 mg per kg) after surgery and allowed to recover for 4–7 days before recordings. To obtain multiple hours recordings of ECoG-LFP at multiple weeks, mice remained in their home cage during an overnight recording session. ECoG-LFP data were collected using a ME2100-system (Multi Channel Systems); ECoG-LFP data were acquired at a sampling rate of 2 kHz using the multi-channel experimenter software (Multi Channel Systems). An additional 0.1–200 Hz digital bandpass filter was applied before data analysis. Large noise signals, due to excessive locomotion or grooming, were manually removed from the data. The ECoG and LFP recordings were processed offline with the Neuroarchiver tool (Open-Source Instruments, www.opensourceinstruments.com/Electronics/A3018/Seizure_Detection.html). To detect interictal spikes, an event detection library was built as described previously (Dubey et al., 2018). During the initial learning phase of the library, the observer, if needed, overruled the identity of each new event by the algorithm until automated detection reached a false positive rate <1%. Subsequently, the ECoG-LFP data were detected by using a single library across all ECoG-LFP recordings. For determining the interictal rate, only S1 LFP signals were used for quantification.

In vivo optogenetics with simultaneous ECoG-LFP recordings

50 nL of AAV1 particles (titer 1 × 1012 cfu/mL) produced from pAAV-EF1a-double-floxed-hChR2(H134)-EYFP-WPRE-HGHpA (Addgene #20298, RRID:Addgene_20298) was injected unilaterally into the L5 of S1 (coordinates from bregma; AP 0.15 mm, ML 0.30 mm, and DL 0.75 mm) of 6–9-week-old PV-Cre; Ai14 mice. ECoG-LFP electrode (stereotaxic coordinates relative to bregma: –0.15 mm anterior and ±0.30 mm lateral; for LFP; ventral 0.75 mm) and ground electrode (6 mm posterior and 1 mm lateral) were implanted through small holes drilled in the skull, held in place with stainless steel screws (A2-70, Jeveka). Through the drilled hole, a polished multimode optical fiber (FP200URT, Thorlabs) held in ceramic ferrule (CFLC230-10, Thorlabs) was driven into layer 5 and ~50 μm above virus injection site. Once optical fiber and electrode were correctly placed, the drilled hole subsequently sealed with dental cement. A blue fiber-coupled laser (473 nm, DPSS Laser T3, Shanghai Laser & Optics Co.) was used to activate the ChR2. Cyclops LED Driver (Open Ephys), together with customized

program, was used to design the on and off state of the laser. The driving signal from LED driver was also recorded at one of the empty channels in multichannel systems. This signal was used to estimate the blue light on or off condition. For gamma entrainment in S1, 40 pulses of blue light were flashed with 1 ms on and 28 ms off pulse.

To inhibit interictal spikes, 300 pulses of blue light were flashed with 1 s on and 100 ms off by manual activation of light pulses when periods of high interictal spikes were observed (>10 interictals/min). Aged-matched control mice were stimulated during the resting phase of the EEG, which was estimated using online EMG signal and video observation. For interictal counts, 5 min LFP signals were used from before light stimulation, during, and post light stimulation. Interictals were detected using event detection library. For analysis of the cortical rhythms, epochs were extracted using 2 s window at the start and after 180 pulses of blue light. Epoch-containing interictals were not included in the analysis.

For pharmacology experiment, continuous LFP recordings of >10–12 hr duration from the circadian quiet phase (from 19:00 to 09:00) of six cuprizone mice (7-week treatment) and three control mice were used for the analysis. To activate GABAA receptors in cuprizone-treated mice, we used diazepam (Centrafarm Nederland B.V) prepared in a 10% solution of (2-hydroxypropyl)-β-cyclo-dextrin (Sigma-Aldrich). A nonsedative dose of 2 mg/kg diazepam was injected intraperitoneally, and data was acquired for a period of 10 hr, starting 15 min after injection of drug in control and cuprizone mice. The automated event detection library (Figure 1–figure supplement 1) was used to determine the event frequency before and after diazepam injection.

In vivo power spectrum analysis

Power spectral density (PSD) analysis was done using multitaper PSD toolbox from Igor Pro 8.0 (RRID:SCR_000325). The absence of high-voltage activity in the EMG electrode was classified as quiet wakefulness (Figure 1–figure supplement 1, Figure 1). For PSD analysis during interictal activity, a 2 s window was used to extract LFP signal epochs. Epochs from control animals were selected comparing the EMG activity with cuprizone EMG activity. The interictal activity itself was excluded from the analysis. Selected LFP epochs were bandpass filtered between different frequency bands; delta, δ (0.5–3 Hz), theta, θ (4–12 Hz), beta, β (12.5–25 Hz), and gamma, γ (30–80 Hz). Multitaper PSD function (Igor Pro 8.0) was applied to the filtered data to plot the power distribution within each frequency band. Area under the curve was measured for each frequency band to compare power density between the control and cuprizone groups.

Immunohistochemistry

L5 PNs were filled with 10 mg/mL biocytin during whole-cell patch-clamp recording for at least 30 min. Slices were fixed for 30 min with 4% paraformaldehyde (PFA) and stored in 0.1 M phosphate buffered saline (PBS; pH 7.4) at 4°C. Fixed 400 µm slices were embedded in 20% gelatin (Sigma-Aldrich) and then sectioned with a Vibratome (VT1000 S, Leica Microsystems) at 80 µm. Sections were preincubated with blocking 0.1 M PBS containing 5% normal goat serum (NGS), 5% bovine serum albumin (BSA; Sigma-Aldrich), and 0.3% Triton-X (Sigma) during 2 hr at 4°C to make the membrane permeable. For biocytin-labeled cells, streptavidin biotin-binding protein (Streptavidin Alexa 488, 1:500, Invitrogen, RRID:AB_2315383) was diluted in 5% BSA with 5% NGS and 0.3% Triton-X overnight at 4°C. Sections including biocytin-filled cells were incubated again overnight at 4°C with primary antibody rabbit anti-ßIV-spectrin (1:200; gift from M.N. Rasband, Baylor College of Medicine), mouse anti-MBP (1:250; Covance), mouse anti-PV (1:1000; Swant, RRID:AB_10000343), rabbit anti-syt2 (1:500, Synaptic Systems, RRID:AB_108 94084) in PBS blocking solution containing 5% BSA with 5% NGS and 0.3% Triton-X. Secondary antibody were used to visualize the immunoreactions: Alexa 488-conjugated goat anti-rabbit (1:500; Invitrogen), Alexa 488 goat anti-mouse (1: 500; Sanbio), Alexa 488 goat anti- guinea pig, Alexa 555 goat anti-mouse (1:500; Invitrogen), Alexa 555 goat anti-rabbit (1:500; Invitrogen), Alexa 633 goat anti-guinea pig (1:500; Invitrogen), Alexa 633 goat anti-mouse (1:500; Invitrogen), and Alexa 633 goat anti-rabbit (1:500; Invitrogen). Finally, sections were mounted on glass slides and cover slipped with Vectashield H1000 fluorescent mounting medium (Vector Laboratories, Peterborough, UK) and sealed.

Confocal imaging

A confocal laser-scanning microscope SP8 X (DM6000 CFS; acquisition software, Leica Application Suite AF v3.2.1.9702, RRID:SCR_013673) with a ×63 oil-immersion objective (1.3 NA) and with 1× digital zoom was used to collect images of the labeled L5 neurons and the abovementioned proteins. Alexa fluorescence was imaged using corresponding excitation wavelengths at 15 units of intensity and a z-step of 0.3 µm. Image analysis was performed with Fiji (ImageJ) graphic software (v.2.0.0-rc-65/1.5w, National Institutes of Health, RRID:SCR_002285).

Synaptic puncta counting and image analysis

The intensity of PV^+ or Syt2 immunostaining was measured with a z-axis profile, calculating the mean RGB value for each z-plane. When quantifying the axosomatic puncta, the soma was defined to extend into the apical dendrite maximally ~4 µm and a boundary was drawn around the maximum edges (ROI). For counting apical dendritic puncta, a 200 µm length of apical dendrite was selected as ROI. Linear

immunofluorescent signals from ßIV-spectrin were identified as AIS and used as ROI. For all analyses, the RGB images were separated into single-color channels using the color deconvolution plugin in ImageJ. The single-color channel containing boutons signals was subjected to thresholding and particle filter of 0.5 µm. The threshold was saved and applied to all images in the same staining group. The boutons were selected by scanning through the 3D projection of ROI with 0.35 µm z-steps. Trained experimenters identified the boutons either by colocalization of the ROI and PV/Syt2 or direct contact of the two. The boutons were characterized as round spots with a minimal radius of 0.5 µm ranging to almost 2 µm. Three experimenters blinded to the identity of the experiment group independently replicated the results. All image analyses were done in Fiji (ImageJ) graphic software (v.2.0.0-rc-65/1.5w, National Institutes of Health, RRID:SCR_002285).

PV+ axon reconstruction and quantification

For immunolabeling of biocytin-filled PV[+] interneuron, 400 µm electrophysiology slices were incubated overnight at 4°C in PFA. Slices were rinsed with PBS followed by staining using streptavidin 488 (1:300, Jackson) diluted in PBS containing 0.4% Triton-X and 2% normal horse serum (NHS; Gibco) overnight at 4°C. Confocal images of 400-µm-thick slices were taken (see 'Confocal imaging') and immediately after thoroughly rinsed with 0.1 M PB and 30% sucrose at 4°C overnight. Next, slices were sectioned into 40 µm thick and preserved in 0.1 M PB before staining. Sections were preincubated in PBS blocking buffer containing 0.5% Triton-X and 10% NHS during 1 hr at room temperature. Sections were stained with primary mouse anti-MBP (1:300, Santa Cruz, RRID:AB_675707), rat anti-syt2 (RRID:AB_10894084) in 0.4% Triton-X, and 2% NHS with PBS solution for 72 hr. Alexa 488-conjugated secondary antibodies (1:300, Invitrogen) were added in PBS containing 0.4% Triton-X and 2% NHS, posterior to washing steps with PBS. Then, sections were mounted on slides and cover slipped with Vectashield H1000 fluorescent mounting medium, sealed, and imaged. Biocytin-labeled PV^{+} neurons were imaged using upright Zeiss LSM 700 microscope (Carl Zeiss) with ×10 and ×63 oil-immersion objectives (0.45 NA and 1.4 NA, respectively) and 1× digital zoom with step size of 0.5 µm. Alexa 488 and Alexa 647 were imaged using 488 and 639 excitation wavelengths, respectively. The 10× image was taken to determine the exact location of biocytin-filled cells. Subsequently, axonal images were taken at ×63 magnification. Axons were analyzed as described previously (Stedehouder et al., 2019) and identified by their thin diameter, smoothness, obtuse branching processes, and occasionally by the presence of the axon bleb. Images were opened in Neurolucida 360 software (v2018.02, MBF Bioscience, RRID:SCR_001775) for reconstruction using the interactive user-guided trace with the Directional Kernels method. Axon and myelinated

segments were analyzed using Neurolucida Explorer (MBF Bioscience, RRID:SCR_001775). Axonal segments were accepted as myelinated when at least one MBP-positive segment colocalized with streptavidin across the internode length.

Statistics

All statistical tests were performed using Prism 8 or 9 (GraphPad Software, LLC, San Diego, CA, RRID:SCR_014284). For comparisons of two independent groups, we used two-tailed Mann–Whitney U-tests. For multiple group comparisons, data were initially assessed for normality and subsequently we either used ordinary one-way ANOVA followed by Tukey's multiple comparisons or two-way ANOVA with repeated measures followed by Šidák's multiple comparisons tests to correct for multiple comparisons. The level of significance was set to 0.05 for rejecting the null hypothesis. A detailed overview of the statistical analyses performed in this study, together with the numbers used for figures and statistical testing, is provided in Source data 1.

Author contribution

Synaptic puncta counting and image analysis; PV axonal and myelin reconstruction; PV electrophysiological properties analysis.

Supplementary data
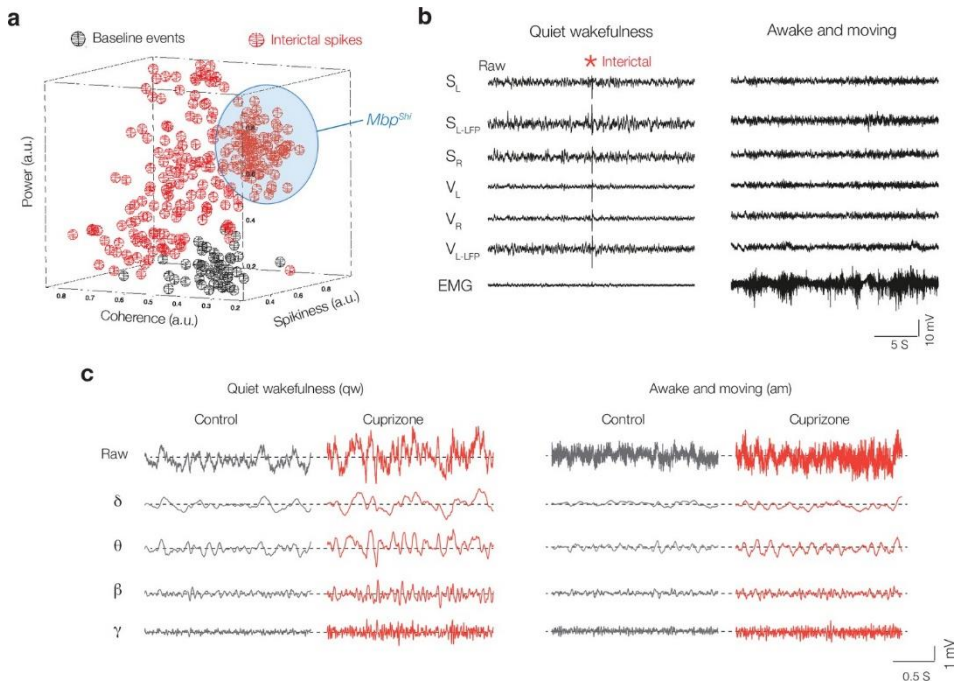
Figure 1 – figure supplement 1. State-dependent interictal activity in cuprizone mice and automated interictal event detection library. a) Automated event detection library used for interictal classification. Three-dimensional projection metric space, showing coherence, spikiness, and signal power (a.u. = arbitrary units), with colors corresponding to interictal (red) and baseline/normal (black) events. The event library was constructed by an operator who classified events as 'normal' or interictal events. The blue domain represents the population of interictal events from Mbp^{Shi} mice. **b**) Example of a 30 s recording from multiple electrodes from 6-week cuprizone-treated mouse. Left: traces during the awake state, note the high-voltage electromyography (EMG) activity. Right: same mouse during quiet wakefulness with low EMG activity. Interictal discharge indicated with red asterisk (*). **c**) Example traces showing raw local field potential (LFP) signals from S1 (top) and bandpass-filtered traces (bottom) at different brain states in control (black) and cuprizone (red) for delta (δ, 0.5–3.5 Hz), theta (θ, 4–12 Hz), beta (β, 12.5–25 Hz), and gamma (γ, 30–80 Hz).
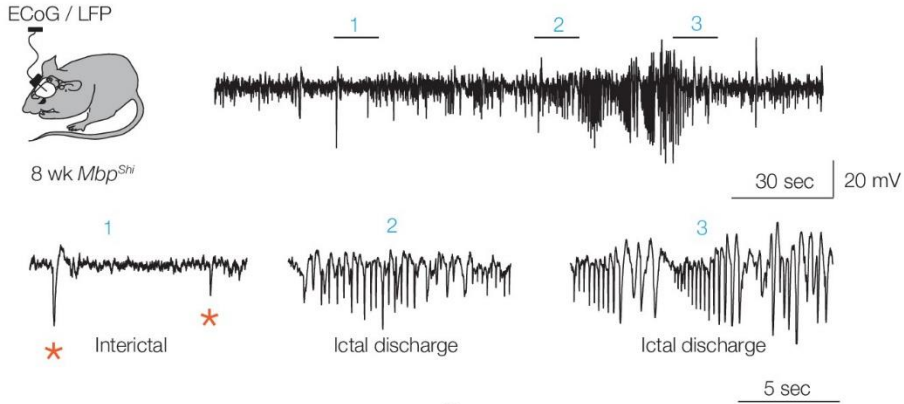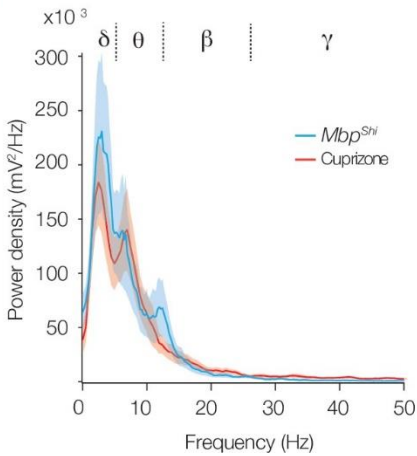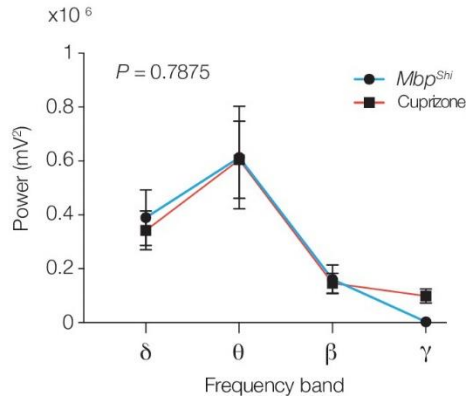
Figure 1 – figure supplement 2. Ictal, interictal activity, and power spectrum in *Mbp*Shi mice.
a) Schematic drawing showing electrocorticogram (ECoG) and local field potential (LFP) recordings from S1 of *Mbp*+/+ and *Mbp*Shi mice. Example LFP trace showing pre-ictal and ictal discharge from 8-week-old *Mbp*Shi mouse (top). Bottom: higher temporal resolution of the top LFP trace showing ECoG activity with interictals (1) and ictal discharge (2 and 3). **b, c**) Comparable power spectral content during interictal activity in cuprizone (red) and *Mbp*Shi (blue) (two-way ANOVA myelin models p<0.0001, Šidák's multiple comparisons cuprizone vs. *Mbp*Shi; for δ, p=0.9952; θ, p>0.9999; β, p>0.9999 and for γ, p=0.9346). Data shown as mean ± SEM.
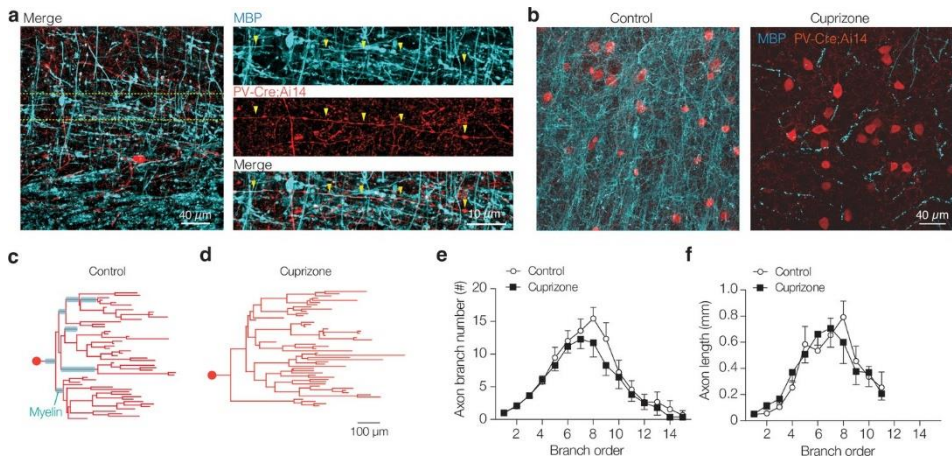
Figure 2 – figure supplement 1. Cuprizone treatment causes loss of parvalbumin-positive (PV⁺) axon myelination but preserves axon length and complexity. a) Left: confocal image of control staining in layer 5 (L5) of S1 showing a PV⁺ interneuron. Right: higher magnification of the image in right, illustrating the trajectory of a myelinated PV⁺ interneuron axon (yellow arrows). Note that also PV⁺ axon swellings are frequently myelinated. **b**) A confocal z-stack image examples of the L5 region in control (left) and cuprizone (right)-treated mice. **c**) Axonograms of a control and **d**) a cuprizone axon. Myelinated segments indicated with cyan. **e, f**) Segment number and length per branch order. Both number and length of axon segments were not significantly affected by cuprizone-induced demyelination (two-way ANOVA treatment × branch order interaction p=0.8028 and p=0.6236, respectively). Data shown as mean ± SEM.
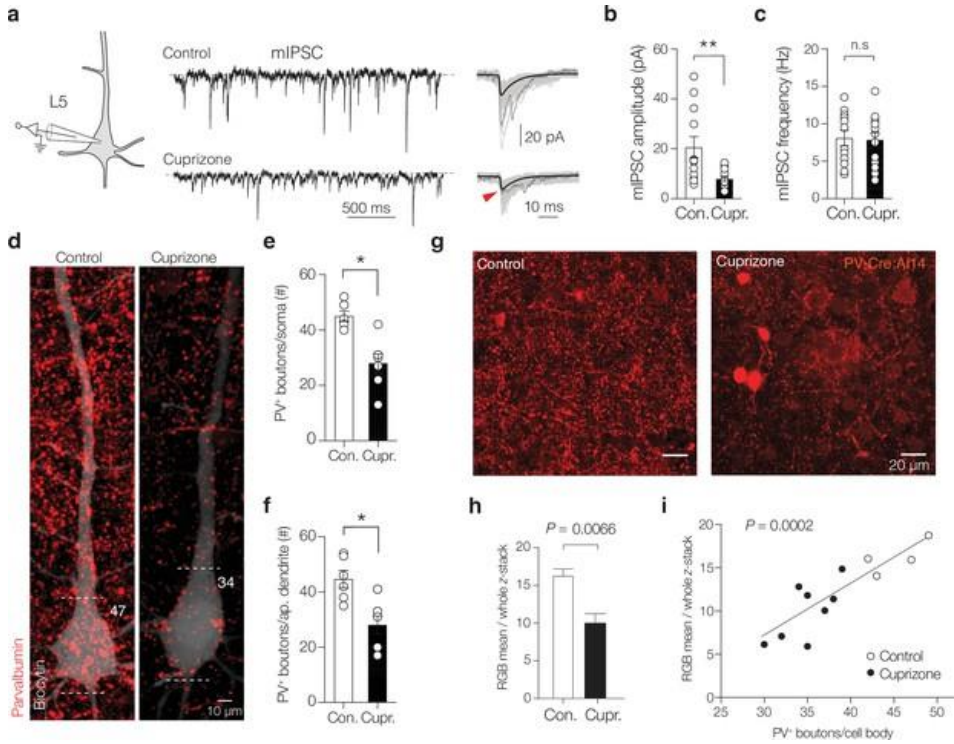
Figure 3 – figure supplement 1. Cuprizone decreases miniature inhibitory postsynaptic currents (mIPSCs) and somatodendritic parvalbumin (PV) puncta. **a**) Left: example traces of miniature inhibitory postsynaptic currents (mIPSCs) at the soma of layer 5 (L5) pyramidal neurons in the presence of CNQX, d-AP5, and TTX in control (top) and demyelinated conditions (bottom). **b, c**) Population data showing an approximately threefold mIPSC peak amplitude but not frequency reduction (Mann–Whitney test **p=0.0025; n.s., p=0.728). (d) Example images of maximum z-projection of a biocytin-filled L5 pyramidal neurons (PNs) (white) overlaid with PV immunofluorescence (red). Dotted lines indicate the soma borders with number indicating counted PV+ puncta. **e, f**) Population analysis reveals a significant loss in the number of PV+ puncta at the L5 soma (Mann–Whitney test *p=0.0035) and the primary proximal apical dendrite (<200 μm, *p=0.0044). **g, h**) Example confocal z-stack images of L5 in control (left) and cuprizone-treated mice (right) reveal a global significant reduction in PV immunofluorescence intensity. **i**) Regression plot reveals the mean PV immunofluorescence intensity correlates with the number of PV+ boutons on large NeuN+ pyramidal neurons cell bodies (r^2 = 0.755). NeuN+ immunofluorescent signals are not shown. The soma diameters of pyramidal neurons were unchanged (cuprizone 18.23 ± 0.99 μm, n = 6 vs. 18.37 ± 0.68 μm, Mann–Whitney U-test p=0.954, n = 9).
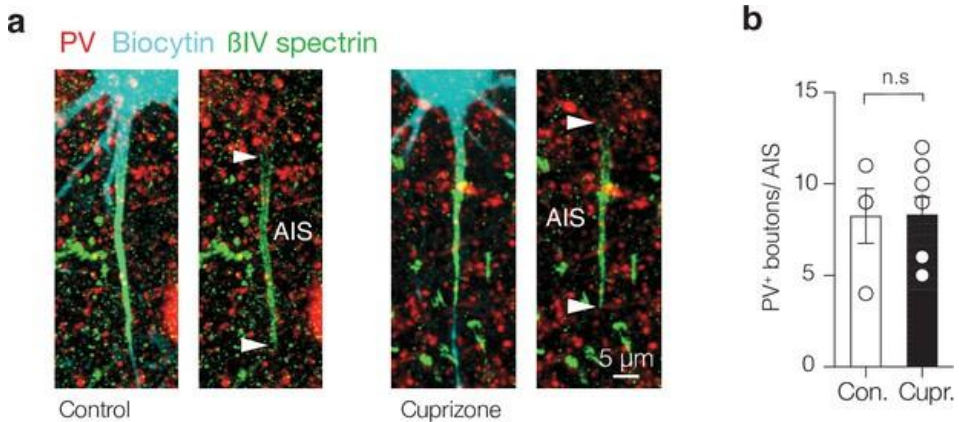
Figure 3 – figure supplement 2. Putative parvalbumin-positive (PV+) chandelier inputs at the axon initial segment (AIS) are unaffected by cuprizone-induced demyelination. a) A confocal z-projection of a biocytin-filled (cyan) layer 5 (L5) pyramidal neuron overlaid with βIV spectrin (green) and parvalbumin (+). **b**) The number of putative chandelier PV+ boutons was preserved in cuprizone-treated mice (Mann–Whitney test p=0.96). Data are shown as mean ± SEM and open circles individual neurons. n.s., not significant.
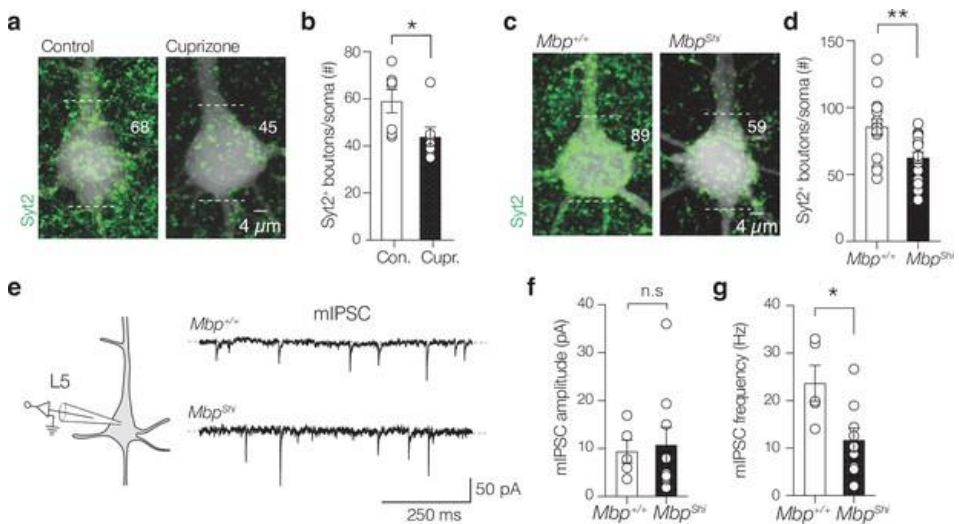
Figure 3 – figure supplement 3. Demyelination and dysmyelination reduces miniature inhibitory postsynaptic currents (IPSCs) and perisomatic Syt2+ puncta. a) Maximum z-projection of biocytin-filled layer 5 (L5) pyramidal neuron (PN) (white) overlaid with Syt2+ immunofluorescence (green). Numbers indicate the Syt2+ puncta counted at the soma. **b**) Population analysis reveals a significant Syt2+ puncta loss (two-tailed Mann–Whitney U-test *p=0.0216). **c**) Maximum z-projection of a biocytin-filled L5 soma (white) overlaid with Syt2+ immunofluorescence (green) from Mbp+/+ and MbpShi mice. **d**) Population analysis shows a

significant loss of Syt2^{+} puncta in the *Mbp*[Shi] mice (**p=0.0013). **e**) Example traces of miniature inhibitory postsynaptic currents (mIPSCs) of L5 PNs in the presence of CNQX, d-AP5, and TTX in *Mbp*^{+/+} (top) and *Mbp*[Shi] mice (bottom). **f, g**) mIPSCs' peak amplitude was unaffected but frequency is reduced in *Mbp*[Shi] (n.s., p=0.797 and *p=0.019, respectively). Data are shown as mean ± SEM and open circles individual neurons. n.s., not significant.
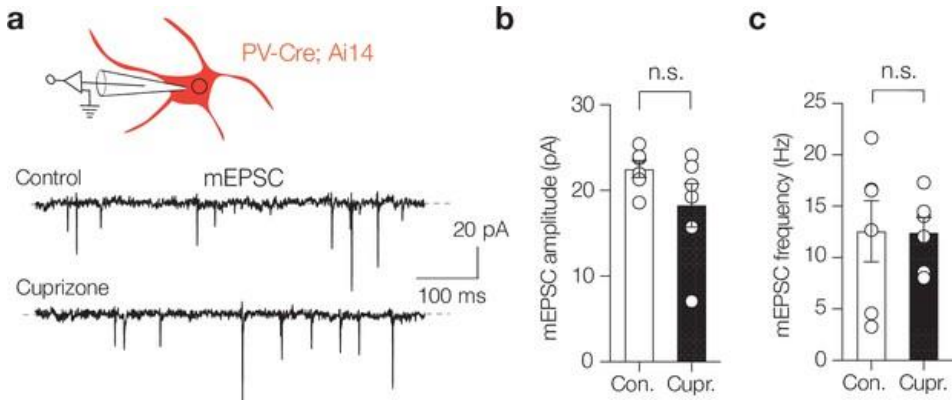
Figure 3 – figure supplement 4. Demyelination does not affect excitatory drive of parvalbumin-positive (PV^{+}) basket cells (BCs). a) Left: schematic of whole-cell voltage-clamp recording for mEPSCs in identified parvalbumin interneurons in the PV-Cre; Ai14 mouse line. mEPSCs were recorded in control mice and mice with 6-week cuprizone feeding. **b, c**) Population data of mEPSC recordings revealed no difference in amplitude (Mann–Whitney test, n.s., p=0.240) nor mEPSC frequency (Mann–Whitney test, n.s., p=0.937). Data are shown as mean ± SEM and open circles individual neurons. n.s., not significant.
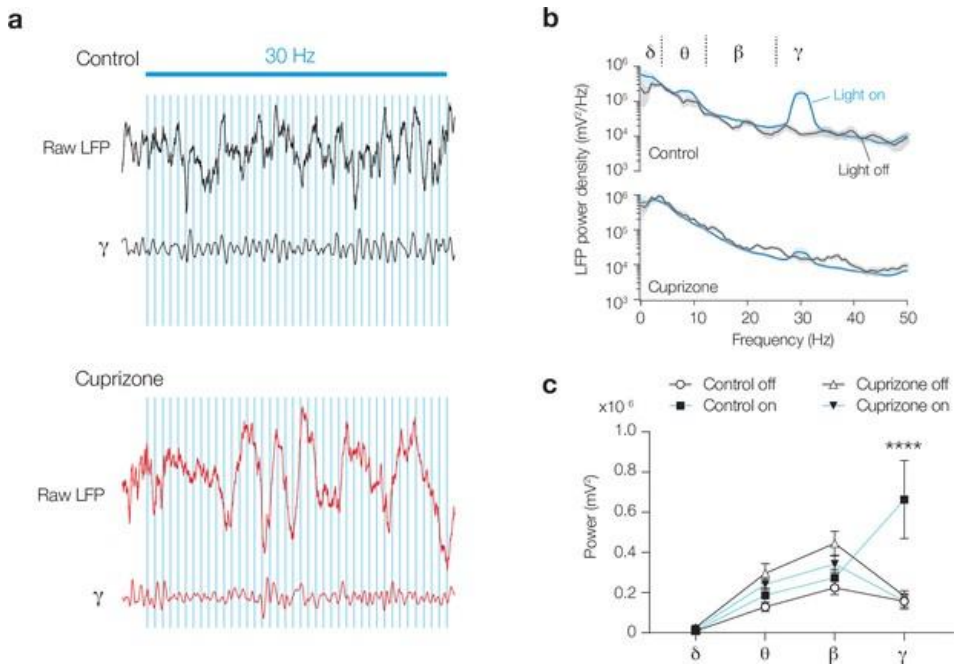
Figure 5 – figure supplement 1. **Myelin loss abolishes optogenetically evoked entrainment of γ rhythm, a**) Raw local field potential (LFP) and low gamma (γ) 25–40 Hz bandpass-filtered trace during 30 Hz blue light stimulation in control (black) and cuprizone (red) mice. Blue light shifted the phase or extended the γ cycle in control mice. **b**) Averaged power spectral density content of low-γ entrainment during *light on* (blue lines) or *off* (black lines). (**c**) 30 Hz blue light stimulation (blue lines) showed a lack of γ band entrainment in cortex of demyelinated mice (closed triangles) in comparison to the control mice (closed squares). Two-way ANOVA frequency × treatment p=0.0002, Šidák's multiple comparisons tests; γ, ****p<0.0001; all other bands p>0.910. Data shown as mean ± SEM.
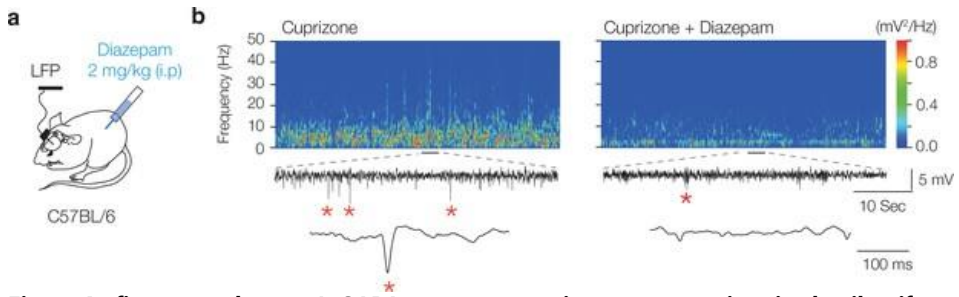
Figure 6 – figure supplement 1. **GABA$_A$ receptor agonism suppresses interictal epileptiform discharge frequency. a**) The GABA$_A$ receptor agonist, diazepam, was injected i.p. at 7 weeks of cuprizone treatment, and local field potential (LFP) recordings performed 10 hr post diazepam injection. **b**) Example time frequency plot before (left) and after diazepam injection (right) showing suppression of interictal epileptiform discharges in cuprizone-treated mice.

References

1. Hu, H., Gan, J. & Jonas, P. Fast-spiking, parvalbumin+ GABAergic interneurons: From cellular design to microcircuit function. *Science (80-.).* **345**, (2014).

2. Tremblay, R., Lee, S. & Rudy, B. Review GABAergic Interneurons in the Neocortex: From Cellular Properties to Circuits. (2016).

3. Bartos, M. *et al.* Fast synaptic inhibition promotes synchronized gamma oscillations in hippocampal interneuron networks. *Proc. Natl. Acad. Sci. U. S. A.* **99**, 13222–13227 (2002).

4. Gonchar, Y. & Burkhalter, A. Three distinct families of GABAergic neurons in rat visual cortex. *Cereb. Cortex* **7**, 347–358 (1997).

5. Tamás, G., Buhl, E. H. & Somogyi, P. Fast IPSPs elicited via multiple synaptic release sites by different types of GABAergic neurone in the cat visual cortex. *J. Physiol.* **500**, 715–738 (1997).

6. Atallah, B. V., Bruns, W., Carandini, M. & Scanziani, M. Parvalbumin-Expressing Interneurons Linearly Transform Cortical Responses to Visual Stimuli. *Neuron* **73**, 159–170 (2012).

7. Cardin, J. A. *et al.* Driving fast-spiking cells induces gamma rhythm and controls sensory responses. *Nat. 2009 4597247* **459**, 663–667 (2009).

8. Lee, S., Chong, S. Y. C., Tuck, S. J., Corey, J. M. & Chan, J. R. A rapid and reproducible assay for modeling myelination by oligodendrocytes using engineered nanofibers. *Nat. Protoc.* **8**, 771–82 (2013).

9. Yang, J. W. *et al.* Optogenetic Modulation of a Minor Fraction of Parvalbumin-Positive Interneurons Specifically Affects Spatiotemporal Dynamics of Spontaneous and Sensory-Evoked Activity in Mouse Somatosensory Cortex in Vivo. *Cereb. Cortex* **27**, 5784–5803 (2017).

10. Zucca, S. *et al.* An inhibitory gate for state transition in cortex. *Elife* **6**, (2017).

11. Chen, C., Arai, I., Satterfield, R., Young, S. M. & Jonas, P. Synaptotagmin 2 Is the Fast Ca2+ Sensor at a Central Inhibitory Synapse. *Cell Rep.* **18**, 723–736 (2017).

12. Sommeijer, J. P. & Levelt, C. N. Synaptotagmin-2 Is a Reliable Marker for Parvalbumin Positive Inhibitory Boutons in the Mouse Visual Cortex. *PLoS One* **7**, e35323 (2012).

13. Somogyi, P., Kisvárday, Z. F., Martin, K. A. C. & Whitteridge, D. Synaptic connections of morphologically identified and physiologically characterized large basket cells in the striate cortex of cat. *Neuroscience* **10**, 261–294 (1983).

14. Thomson, A. M., West, D. C., Hahn, J. & Deuchars, J. Single axon IPSPs elicited in pyramidal cells by three classes of interneurones in slices of rat neocortex. *J. Physiol.* **496**, 81–102 (1996).

15. Micheva, K. D. *et al.* A large fraction of neocortical myelin ensheathes axons of local inhibitory neurons. *Elife* **5**, (2016).

16. Peters, A. & Proskauer, C. Smooth or sparsely spined cells with myelinated axons in rat visual cortex. *Neuroscience* **5**, 2079–2092 (1980).

17. Stedehouder, J. *et al.* Fast-spiking Parvalbumin Interneurons are Frequently Myelinated in the Cerebral Cortex of Mice and Humans. *Cereb. Cortex* **27**, 5001–5013 (2017).

18. Yang, S. M., Michel, K., Jokhi, V., Nedivi, E. & Arlotta, P. Neuron class-specific responses govern adaptive myelin remodeling in the neocortex. *Science (80-.).* **370**, (2020).

19. Cohen, C. C. H. *et al.* Saltatory Conduction along Myelinated Axons Involves a Periaxonal Nanocircuit. *Cell* (2019).

20. Nave, K.-A. & Werner, H. B. Myelination of the nervous system: mechanisms and functions. *Annu. Rev. Cell Dev. Biol.* **30**, 503–533 (2014).

21. Micheva, K. D., Kiraly, M., Perez, M. M. & Madison, D. V. Conduction Velocity Along the Local Axons of Parvalbumin Interneurons Correlates With the Degree of Axonal Myelination. *Cereb. Cortex* **31**, 3374–3392 (2021).

22. Schmidt, H. *et al.* Axonal synapse sorting in medial entorhinal cortex. *Nat. 2017 5497673* **549**, 469–475 (2017).

23. Barron, T., Saifetiarova, J., Bhat, M. A. & Kim, J. H. Myelination of Purkinje axons is critical for resilient synaptic transmission in the deep cerebellar nucleus. *Sci. Reports 2018 81* **8**, 1–12 (2018).

24. Benamer, N., Vidal, M., Balia, M. & Angulo, M. C. Myelination of parvalbumin interneurons shapes the function of cortical sensory inhibitory circuits. *Nat. Commun.* **11**, 5151 (2020).

25. Buzsáki, G. Rhythms of the Brain. *Rhythm. Brain* 1–464 (2006).

26. Sohal, V. S., Zhang, F., Yizhar, O. & Deisseroth, K. Parvalbumin neurons and gamma rhythms enhance cortical circuit performance. *Nat. 2009 4597247* **459**, 698–702 (2009).

27. Veit, J., Hakim, R., Jadi, M. P., Sejnowski, T. J. & Adesnik, H. Cortical gamma band synchronization through somatostatin interneurons. *Nat. Neurosci. 2017 207* **20**, 951–959 (2017).

28. Clarner, T. *et al.* Myelin debris regulates inflammatory responses in an experimental demyelination animal model and multiple sclerosis lesions. *Glia* **60**, 1468–1480 (2012).

29. Hamada, M. S. & Kole, M. H. P. Myelin Loss and Axonal Ion Channel Adaptations Associated with Gray Matter Neuronal Hyperexcitability. *J. Neurosci.* **35**, 7272–7286 (2015).

30. Kipp, M., Clarner, T., Dang, J., Copray, S. & Beyer, C. The cuprizone animal model: new insights into an old story. *Acta Neuropathol. 2009 1186* **118**, 723–736 (2009).

31. Cohen, I., Navarro, V., Clemenceau, S., Baulac, M. & Miles, R. On the Origin of Interictal Activity in Human Temporal Lobe Epilepsy in Vitro. *Science (80-.).* **298**, 1418–1421 (2002).

32. Dubey, M. *et al.* Seizures and disturbed brain potassium dynamics in the leukodystrophy megalencephalic leukoencephalopathy with subcortical cysts. *Ann. Neurol.* **83**, 636–649 (2018).

33. Hoffmann, K., Lindner, M., Gröticke, I., Stangel, M. & Löscher, W. Epileptic seizures and hippocampal damage after cuprizone-induced demyelination in C57BL/6 mice. *Exp. Neurol.* **210**, 308–321 (2008).

34. Tóth, K. *et al.* Hyperexcitability of the network contributes to synchronization processes in the human epileptic neocortex. *J. Physiol.* **596**, 317–342 (2018).

35. Readhead, C. *et al.* Expression of a myelin basic protein gene in transgenic shiverer mice: Correction of the dysmyelinating phenotype. *Cell* **48**, 703–712 (1987).

36. Chernoff, G. F. Shiverer: an autosomal recessive mutant mouse with myelin deficiency. *J. Hered.* **72**, 128–128 (1981).

37. Brill, J., Mattis, J., Deisseroth, K. & Huguenard, J. R. LSPS/Optogenetics to Improve Synaptic Connectivity Mapping: Unmasking the Role of Basket Cell-Mediated Feedforward Inhibition. *eNeuro* **3**, 2190–2203 (2016).

38. Packer, A. M. & Yuste, R. Dense, Unspecific Connectivity of Neocortical Parvalbumin-Positive Interneurons: A Canonical Microcircuit for Inhibition? *J. Neurosci.* **31**, 13260–13271 (2011).

39. Turecek, J., Jackman, S. L. & Regehr, W. G. Synaptic Specializations Support Frequency-Independent Purkinje Cell Output from the Cerebellar Cortex. *Cell Rep.* **17**, 3256–3268 (2016).

40. Xu, J., Mashimo, T. & Südhof, T. C. Synaptotagmin-1, -2, and -9: Ca2+ Sensors for Fast Release that Specify Distinct Presynaptic Properties in Subsets of Neurons. *Neuron* **54**, 567–581 (2007).

41. Traue, R. D., Jefferys, J. G. R. & Whittington, M. A. Simulation of Gamma Rhythms in Networks of Interneurons and Pyramidal Cells. *J. Comput. Neurosci. 1997 42* **4**, 141–150 (1997).

42. Wang, X. J. & Buzsáki, G. Gamma Oscillation by Synaptic Inhibition in a Hippocampal Interneuronal Network Model. *J. Neurosci.* **16**, 6402–6413 (1996).

43. Zhou, J. L., Lenck-Santini, P. P., Zhao, Q. & Holmes, G. L. Effect of Interictal Spikes on Single-Cell Firing Patterns in the Hippocampus. *Epilepsia* **48**, 720–731 (2007).

44. Kleen, J. K., Scott, R. C., Holmes, G. L. & Lenck-Santini, P. P. Hippocampal interictal spikes disrupt cognition in rats. *Ann. Neurol.* **67**, 250–257 (2010).

45. Gentet, L. J., Avermann, M., Matyas, F., Staiger, J. F. & Petersen, C. C. H. Membrane Potential Dynamics of GABAergic Neurons in the Barrel Cortex of Behaving Mice. *Neuron* **65**, 422–435 (2010).

46. Poulet, J. F. A. & Petersen, C. C. H. Internal brain state regulates membrane potential synchrony in barrel cortex of behaving mice. *Nat. 2008 4547206* **454**, 881–885 (2008).

47. Steriade, M. Synchronized activities of coupled oscillators in the cerebral cortex and thalamus at different levels of vigilance. *Cereb. Cortex* **7**, 583–604 (1997).

48. Dahal, P. *et al.* Interictal epileptiform discharges shape large-scale intercortical communication. *Brain* **142**, 3502–3513 (2019).

49. Ujma, P. P., Halász, P., Kelemen, A., Fabó, D. & Erőss, L. Epileptic interictal discharges are more frequent during NREM slow wave downstates. *Neurosci. Lett.* **658**, 37–42 (2017).

50. Stedehouder, J. *et al.* Local axonal morphology guides the topography of interneuron myelination in mouse and human neocortex. *Elife* **8**, (2019).

51. Stedehouder, J. & Kushner, S. A. Myelination of parvalbumin interneurons: a parsimonious locus of pathophysiological convergence in schizophrenia. *Mol. Psychiatry* **22**, 4–12 (2017).

52. Miles, R. Variation in strength of inhibitory synapses in the CA3 region of guinea-pig hippocampus in vitro. *J. Physiol.* **431**, 659–676 (1990).

53. Rossignol, E., Kruglikov, I., Van Den Maagdenberg, A. M. J. M., Rudy, B. & Fishell, G. CaV2.1 ablation in cortical interneurons selectively impairs fast-spiking basket cells and causes generalized seizures. *Ann. Neurol.* **74**, 209–222 (2013).

54. Casale, A. E., Foust, A. J., Bal, T. & McCormick, D. A. Cortical Interneuron Subtypes Vary in Their Axonal Action Potential Properties. *J. Neurosci.* **35**, 15555–15567 (2015).

55. Hu, H. & Jonas, P. A supercritical density of Na+ channels ensures fast signaling in GABAergic interneuron axons. *Nat. Neurosci. 2014 175* **17**, 686–693 (2014).

56. Freeman, S. A. *et al.* Acceleration of conduction velocity linked to clustering of nodal components precedes myelination. *Proc. Natl. Acad. Sci. U. S. A.* **112**, E321–E328 (2015).

57. Lubetzki, C., Sol-Foulon, N. & Desmazières, A. Nodes of Ranvier during development and repair in the CNS. *Nat. Rev. Neurol. 2020 168* **16**, 426–439 (2020).

58. Fünfschilling, U. *et al.* Glycolytic oligodendrocytes maintain myelin and long-term axonal integrity. *Nature* **485**, 517–521 (2012).

59. Micheva, K. D. *et al.* Distinctive Structural and Molecular Features of Myelinated Inhibitory Axons in Human Neocortex. *eNeuro* **5**, 297–315 (2018).

60. Edgar, J. M. *et al.* Early ultrastructural defects of axons and axon–glia junctions in mice lacking expression of Cnp1. *Glia* **57**, 1815–1824 (2009).

61. Chen, Z. *et al.* Microglial displacement of inhibitory synapses provides neuroprotection in the adult brain. *Nat. Commun. 2014 51* **5**, 1–12 (2014).

62. Favuzzi, E. *et al.* GABA-receptive microglia selectively sculpt developing inhibitory circuits. *Cell* **184**, 4048-4063.e32 (2021).

63. Ramaglia, V. *et al.* Complement-associated loss of CA2 inhibitory synapses in the demyelinated hippocampus impairs memory. *Acta Neuropathol.* **142**, 643–667 (2021).

64. Caprariello, A. V. *et al.* Biochemically altered myelin triggers autoimmune demyelination. *Proc. Natl. Acad. Sci. U. S. A.* **115**, 5528–5533 (2018).

65. Skripuletz, T. *et al.* Astrocytes regulate myelin clearance through recruitment of microglia during cuprizone-induced demyelination. *Brain* **136**, 147–167 (2013).

66. Poggi, G. *et al.* Cortical network dysfunction caused by a subtle defect of myelination. *Glia* **64**, 2025–2040 (2016).

67. Benedict, R. H. B., Amato, M. P., DeLuca, J. & Geurts, J. J. G. Cognitive impairment in multiple sclerosis: clinical management, MRI, and therapeutic avenues. *Lancet Neurol.* **19**, 860–871 (2020).

68. Henin, S. *et al.* Spatiotemporal dynamics between interictal epileptiform discharges and ripples during associative memory processing. *Brain* **144**, 1590–1602 (2021).

69. Kleen, J. K. *et al.* Hippocampal interictal epileptiform activity disrupts cognition in humans. *Neurology* **81**, 18–24 (2013).

70. Lam, A. D. *et al.* Silent hippocampal seizures and spikes identified by foramen ovale electrodes in Alzheimer's disease. *Nat. Med. 2017 236* **23**, 678–680 (2017).

71. Chen, J. F. *et al.* Enhancing myelin renewal reverses cognitive dysfunction in a murine model of Alzheimer's disease. *Neuron* **109**, 2292-2307.e5 (2021).

72. Drenthen, G. S. *et al.* On the merits of non-invasive myelin imaging in epilepsy, a literature review. *J. Neurosci. Methods* **338**, 108687 (2020).

73. Zoupi, L. *et al.* Selective vulnerability of inhibitory networks in multiple sclerosis. *Acta Neuropathol.* **141**, 415–429 (2021).

74. Schoonheim, M. M. *et al.* Functional connectivity changes in multiple sclerosis patients: A graph analytical study of MEG resting state data. *Hum. Brain Mapp.* **34**, 52–61 (2013).

75. Tewarie, P. *et al.* Disruption of structural and functional networks in long-standing multiple sclerosis. *Hum. Brain Mapp.* **35**, 5946–5961 (2014).

76. Cawley, N. *et al.* Reduced gamma-aminobutyric acid concentration is associated with physical disability in progressive multiple sclerosis. *Brain* **138**, 2584–2595 (2015).

77. Gao, F. *et al.* Altered hippocampal GABA and glutamate levels and uncoupling from functional connectivity in multiple sclerosis. *Hippocampus* **28**, 813–823 (2018).

Chapter 9

General discussion

The plasticity of the brain enables us to learn, adapt and modify our behaviour according to the environment. Brain plasticity is not solely dependent on synaptic rearrangements and neuronal changes, but other players, such as glial cells, are also responsible for adjustments of neuronal networks[1]. Oligodendrocytes are the myelinating cells in the central nervous system (CNS). They modulate neuronal circuit function though dynamic regulation of myelin, altering the number, thickness and location of myelin sheaths in response to neural activity[1,2]. Therefore, myelin plasticity contributes to the fine-tuning of cellular conduction in neural networks, enabling the remodelling of the brain to the milieu.

In this general discussion, I examine the correlation between neuronal cell type - their function, their location and their axonal morphology – and their myelination status (*Chapters 2, 3* and *4*). I also discuss the evolution of myelin among vertebrates, divergence across species and the implications of these differences. Next, I delve into the molecular mechanisms that might underlie neuropsychiatric disorders by analysing myelin developmental and maturation deficiencies and their effects on neuronal connectivity (*Chapters 5* and *6*) and schizophrenia-related genes that might have an impact on oligodendrocytes or myelination (*Chapters 7* and *8*).

Evolutionary adaptation of myelin

Saltatory conduction and metabolic support

The acquisition of myelin by vertebrates has been historically proposed as one of the keys to success. This phenomenon suggests that the evolution of myelin was an optimization process of pre-historic animals and evolved from improving energetic efficiency to increase action potential (AP) velocity[3]. At present, myelin is widely considered an electrical insulator that enhances AP propagation by restricting the Na^+ and K^+ channels responsible of the AP generation to unmyelinated regions. This process is known as saltatory conduction of APs. In this manner, myelin reduces metabolic consumption for neurons[4]. But proper coordination between the myelin sheath and the axon – essential to prevent ion leakage – also restricts the passage of nutrients from the extracellular space into the axon. Thus, a metabolic supporting role of oligodendrocytes in the CNS has also emerged as a critical mechanism in this neuronal-glial interaction[5].

Axo-glia interaction

Extrinsic and intrinsic cues are responsible for inducing oligodendrocyte precursor cell maturation and differentiation, and to select which axonal surfaces to ensheath[6].

Permissiveness to myelination seems to be also given by the biophysical properties of the axonal fibre[6-8]. Axons in the CNS differ in morphology; some are long while other have multiple branches. Some are thin while others are thicker. Axonal calibres have a wide spectrum ranging from 0.1-10 μm[9]. Axonal diameter is important for the propagation of the AP, as thicker axons increase current flow by decreasing internal resistance[10]. Axon diameter varies linearly with firing rate, which in turn corresponds to a higher information rate with an increasing number of synaptic contacts[9]. However, it is not always possible to increase the diameter of an axon due to physical restrictions. Vertebrates have overcome this issue by myelinating axons that have a larger calibre. Furthermore, energy capacity – manifest as the increase in volume of mitochondria - increases exponentially with axonal calibre[9] to maintain the energetic demand. To minimize the power costs of a greater information supply, myelin acts as an energy saviour. Together, axonal morphology variability responds to the need of the system to reduce power consumption while at the same time increasing information rate, with myelin reinforcing this efficient mechanism.

Strengthened connections or other changes in the environment promote structural rearrangements in axonal morphology. This process is known as axonal plasticity. Axonal plasticity may come in different forms, for example after injury or as a homeostatic mechanism. In this chapter, I will discuss the latter. The reorganisation of the axonal shaft involves the cytoskeleton, in particular actin filaments[11]. Axonal calibre is dynamic and controlled by neuronal activity. Indeed, data support that axons grow wider after high-frequency AP firing[12]. In *Chapters 2 and 4* we found that other mechanisms may impact axonal calibre. TSC complex plays an essential role in cell growth and proliferation[13]. Deletion of *Tsc1* at four weeks of age in mice produced a shift of the axonal diameter in all neuronal types investigated (pyramidal cells, PV+ cells and SOM+ cells). Conversely, deletion of *Tsc1* did not cause an increase in firing frequency that could explain axonal growth, suggesting that TSC1 controls axonal morphology through another mechanism, possibly through interactions with the actin cytoskeleton. Moreover, axonal shaft growth resulted in an increase of myelin for all neuronal subtypes investigated (**Figures 2.4, 4.5** and **4.7**), corroborating the importance of axonal calibre for myelination[14], and implying homeostatic mechanisms to overcome the alterations in membrane resistance and sustain metabolic demand.

It is complicated to talk about axonal morphology without mentioning neuronal subtypes. Axonal morphology is highly dependent on cellular function and its connections. Whilst pyramidal cells have long-range projection axons that connect both hemispheres and cortical columns, interneurons expand their axons in a local manner, protruding towards neighbouring columns or layers. In pyramidal cells, where

myelination profiles have been extensively studied[15], myelin fluctuations can be explained by the fast dynamics necessary to transfer information to far distances, and the trophic support necessary for long-range axons[16]. Intriguingly, not all pyramidal cells are myelinated. In *Chapter 2*, we found a subset of pyramidal neurons in the prefrontal cortex that lack myelination, in contrast to 80% of pyramidal cells myelinated in the somatosensory cortex at the same developmental stage. Axonal segment length and calibre measured through super-resolution microscopy were similar in both regions (**Figures 2.1, 2.2**). However, myelinated segments were thicker and longer than unmyelinated ones (**Figure 2.2**). The hypothesis that the joint combination of axonal thickness and length is predictive of segmental myelination was consistent across neuronal subtypes, such as PV$^+$ interneurons, as seen in *Chapter 4*. Nonetheless, the calibre threshold for PV$^+$ interneuron was higher than in pyramidal cells (334 nm and 236 nm, respectively). Several possibilities may explain these findings: (1) different subsets of oligodendrocytes are responsible for excitatory versus inhibitory myelination[17]. These oligodendrocytes might sense different morphological thresholds that enable them to initiate axonal ensheathment. (2) Variability in pyramidal cells is greater than in PV$^+$ interneurons, therefore the threshold is lower due to a lower specificity of the analysis. (3) Pyramidal cells are myelinated along the principal axon, including higher branch order segments, whereas PV$^+$ interneurons restrict myelin to local branches around the soma, usually of lower order. Lower order branch segments are thicker than consecutive orders, indicating a bias towards thicker axons in PV$^+$ interneurons.

In *Chapter 3* we observed that non-fast-spiking (NFS) interneurons, another subclass of interneurons, were scarcely myelinated in mice (~7%), in contrast to PV$^+$ interneurons (~98%). It should be born in mind that NFS interneurons are a heterogeneous group including late-spiking cells (LS; corresponding to neurogliaform cells), regular-spiking non-pyramidal cells (RSNP; mix group mostly composed by SOM$^+$ and VIP$^+$ cells) and burst-spiking non-pyramidal cells (BSNP; mix group of SOM$^+$, VIP$^+$, CCK$^+$, etc.)[18], and therefore, extrapolation of results between groups should be done cautiously. PV$^+$ interneurons are fast-spiking interneurons (FS), which means they fire at high frequencies. As above-mentioned, firing frequency is linear with axonal calibre[9], which may explain why FS interneurons have bigger axonal diameters (**Figure 4.1**). The energetic consumption in FS is much higher due to the maintenance of firing rate[19]. Altogether, these parameters increase the probability and necessity of FS interneurons to become myelinated. None of these characteristics can be attributed to NFS, where firing frequency is in general much lower and the resistance of the membrane is higher, possibly due to thinner axons (**Figure 3.2**). However, a subset of RSNP cells exhibited one myelinated segment. It had been previously reported that some SOM$^+$ segments

exhibit myelination[20,21]. Both myelinated cells had a first branch order myelinated segment, possibly also related to the thinner calibre of higher order branches. What the implications of myelinated NFS are has not been addressed in this thesis. Since we did not observe different results across regions, we can assume that the myelination rate of NFS in mice is similar among cortical regions, although major differences could be encountered in deeper cortical layers. We can speculate, however, that certain SOM+ interneurons increase their activity rate to regulate the excitation of the network, and this increase in activity leads to an increment of axonal thickness and length[22,23]. Subsequently, oligodendrocytes wrap the segments of those cells with higher activity. Altogether, we can conclude that NFS interneurons are much less myelinated and in general have thinner axons than FS interneurons, which may partially explain the divergence of myelination.

To sum up, *Chapters 2, 3* and *4* examined myelination across different neuronal types (**Figure 1**). We found that axonal morphology seems to be a fundamental parameter to predict myelination in all three neuronal subtypes (pyramidal, NFS and FS interneurons), although with somewhat different metrics between each cellular type. This suggests that there are common mechanisms for myelination that are maintained across species and cellular subclasses, and that differences across neuronal subtypes probably depend on their function and location.
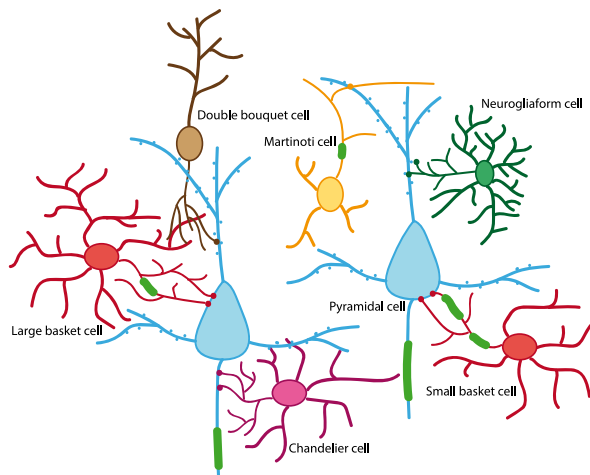
Figure 1. Scheme of the neuronal network. Pyramidal cells (blue), PV+ interneurons (red) and some BSNP interneurons, mostly SST+ interneurons (yellow) are myelinated (green segment). For interneurons, most of the myelinated segments are found in the proximal axon, whereas in pyramidal cells the profile of myelination is always found in the main axon and is dependent on the area in the brain and the layer where they are located.

Diverse myelin extent across species

To study myelin disorders, mouse models are commonly employed. However, it is important to know that myelin composition[24] and extent varies across species, although transcriptomic profiles revealed that the majority of the genes are common to both species[24,25]. In our study, we also found similarities, but also differences between mouse

and human myelination. In *Chapters 2* and *4*, we found that the predictive thresholds for calibre and axonal length in pyramidal and PV⁺ cells yielded similar values in mice and human, suggesting a common mechanism for oligodendrocytes to myelinate the axonal segments of these cells. Finally, in *Chapter 3*, we unexpectedly found that human NFS interneurons were myelinated in roughly 50% of the cases (**Figure 4.4**), in contrast to only ~7% of murine NFS. This finding suggests a novel advance in our understanding of interneuron myelination, showing differences across species.

White matter accounts for almost 60% of human brain volume, whereas this percentage is considerably smaller in other species, such as rodents, where it is only ~20%[26]. Increases in g-ratio due to lower myelin thickness further confirms that rodents have less myelin content than higher order primates[27]. Consistently, our studies indicate as well that pyramidal cells and interneurons show more myelinated segments in human than in mice. But why do primates have more myelin than rodents? Several hypotheses other than biophysical characteristics may explain the functional and thereby molecular reasons that underlie this fact. In the first place, different cellular types may exist. Glial cells underwent the most evolutionary changes among several studied species[28]. An assorted population of oligodendroglia is found within mice and human species. Transcriptomic analyses showed that both species display similar profiles but with distinct gene expression[24]. But not only non-neuronal population can diverge. Whilst homologous neuronal types are comparable between species, the diversity in human cells is greater[28]. Genetic comparison between species also yielded divergent expression[28], suggesting that a smaller neuronal population was not found in either of the species. Hence, all this variability can concur into differences in myelination.

Secondly, a strong correlation between memory and myelination may govern the increase in white matter in human versus mice. Memory is one of the central executive processes of the brain. Many types of learning and memory have been studied in the context of myelination. Myelin is important for the synchronicity and connectivity of the brain, and there is a strong correlation between myelination of cortical areas and life stages of intense learning, such as infancy or adolescence[29]. Evidence indicates that white matter plasticity is necessary for memory formation and maintenance[30]. For example, individuals learning a new language or a new motor skill undergo rearrangements in white matter[31-33]. This remodelling occurs at an axonal level, with myelin sheaths that retract and grow during the learning phase, or new myelin sheaths that are added and are an indication that such changes are necessary to maintain long-term memory[34]. What is yet to be determined, is whether this remodelling of myelin is secondary to axonal plasticity[35]. Adaptations of neuronal activity during learning may impact axonal structure and morphology[35] as well as increase the proliferation and

activation of mature oligodendrocytes[22]. In this manner, myelin also acts as a stabiliser of new axonal modifications, that may occur in more than one cellular type[23,35].

Thirdly, enriched environments combining social, sensory, motor and cognitive stimuli have an important effect on glial cells, and in particular, oligodendrocytes[36]. Sensory enrichment promotes new myelination and strengthens existing myelin sheaths by oligodendrogenesis[37], and the opposite, early social isolation, has a negative impact on myelination of the prefrontal cortex[38,39]. Social experience stimulates myelination of prefrontal areas and it is of great importance to acquire sophisticated cognitive skills in humans[40,41]. This feedback loop between sensory enrichment and cognition boosts myelin levels and presumably accentuates the difference among species. Although in our experiments, mice were not socially isolated, they did not enjoy an enriched environment. Thus, experience-dependent myelination is an added mechanism to the observation of myelin in the human brain.

Lastly, another hypothesis to explain the expansion of myelin in the human brain is the relationship between myelination and intelligence. This theory maintains that individuals with a higher IQ possess higher levels of myelination, therefore reducing overall energy consumption and enhancing communication between regions[42]. MRI methods have addressed this hypothesis and found that general intelligence was associated with white matter microstructure[43]. Intelligence is a highly heritable trait. White matter and intelligence converge into common genetic factors, which suggest that myelin and intelligence are interrelated[44,45]. Thence, the intelligence hypothesis of myelination assumes that the extent of human, and possibly rodent, myelination is partially determined by cognitive processing.

A form of myelin has also been described in other phyla, such as annelids and arthropods[46]. This convergence in evolution suggests the importance of myelination. Few studies in primates have proposed that their myelination levels are a step in between rodents and human[26,27]. However, the reasons underlying the differences in myelination across species is yet to be determined. Our results in *Chapters 2, 3* and *4* are a clear example of differences across species and increased myelination in human tissue at a cellular level. Altogether, the phylogeny of myelin suggests its neurobiological evolution plays a crucial role in the development of higher-order cognitive functions and that it is associated with enriched environment and learning processes.

Myelination in neuropsychiatric disorders

Numerous neuroimaging studies have reported white matter abnormalities in patients suffering from Alzheimer's disease[47], Huntington's chorea[48] and some other neuropsychiatric disorders such as schizophrenia[49] and mood disorders[50]. In *Chapters 5* to *8* we aimed to uncover different myelin mechanisms to understand the pathophysiology of demyelinating disorders in the context of schizophrenia.

Schizophrenia is a complex disorder, in which a myriad of intertwined mechanisms – both genetic and environmental – play a part. Several imaging techniques, genetic studies and animal models have been utilized to understand the pathophysiology of this disorder. However, no single mechanism seems to be associated with the disease. In this thesis, we have employed three different animal models to target demyelinating causes that may lead to neuropsychiatric disorders and two genetic mutations that are linked to schizophrenia, all of them from the perspective of PV⁺ interneuron myelination.

Demyelination behind psychiatric disturbances

Cuprizone-induced demyelination is a well-established technique to study the effects of oligodendrocyte damage and myelin sheath loss, and subsequent remyelination. In *Chapters 5* and *6*, we employed this copper chelator to investigate demyelination at two different stages of life. The developmental stage is relevant to mark the onset of a disease and integrates the results of both chapters. Early demyelination caused alterations in firing pattern and AP shape. These differences were highly correlated with the lack of autapses in these cells, possibly linked to a smaller axonal tree (**Figure 6.1-6.3**). The *shiverer* model of dysmyelination also exhibited a reduced number of autapses linked to high frequency impairments and deficiencies in PV⁺ interneurons, very similar to the ones observed when demyelination starts at early stages (**Figure 6.11, 6.12**). In contrast, adult demyelination caused impairments in the firing frequency and hyperpolarisation of PV⁺ interneurons without apparent impact on axonal arborisation or the number of autapses (**Figure 5.2, 6.10**). The demyelination onset seems, therefore, to be crucial to understand the implications in cellular connectivity and function. Furthermore, these results indicate that myelination shapes cortical activity through modulation of synaptic inhibition, and that the consequences are directly related to the onset of myelin loss.

Cortical myelination in normal conditions is dynamic over the lifespan starting with myelogenesis, continuing with a transient but stable period and finishing with demyelination at older stages of life[51]. Myeloarchitecture is important from a developmental point of view to understand how cortical circuits are built. PV⁺

interneurons are well-known to regulate the gamma-frequency oscillatory network[52]. Gamma oscillations develop along with the maturation of PV[+] interneurons[53,54], and parallel to their myelination. Myelin plasticity is imperative to regulate brain waves and synchronise brain regions[55]. The reason for this is that coupling of oscillatory networks requires temporal precision, and any changes in conduction velocity might disrupt their synchrony[55]. Disturbances of brain synchrony has been associated with schizophrenia[56], and other demyelinating disorders such as multiple sclerosis, where slow-wave oscillations are also altered[57]. Besides, PV[+] interneuron myelination also contributes to the fine-tuning of cortical networks through feedforward inhibition[58]. PV[+] interneurons also form autapses to regulate spike-time precision and fine-tuning of oscillatory waves[59,60]. The number of autapses is also correlated with the strength of connectivity to other neurons[61]. Thence, myelin is tightly associated with the regulation of neuronal connectivity and the strength of inhibitory synapses[62] through the formation of autaptic connections in PV[+] interneurons. Loss of myelination provokes a reduction in connectivity between PV[+] interneurons and pyramidal[63] cells that leads to network hyperexcitability[64], which has been widely observed in clinical demyelinating diseases.

Cognitive impairments are a hallmark of diseases with disturbances in myelination, such as schizophrenia or multiple sclerosis[65,66]. To ensure the correct functioning of brain dynamics, white matter rewires itself in an activity-dependent manner that enables neural synchronisation[67] through gamma oscillations and synaptic inhibition[55]. Partial or complete loss of myelination along PV[+] interneurons, which are responsible for these mechanisms, suggests a common pathway that results in memory impairments and other cognitive decline, observed in schizophrenia or multiple sclerosis patients[68,69]. Correspondingly, we observed an increase of theta oscillation power and accompanied by interictal spikes mediated by the deficit of PV[+] inhibition (**Figure 5.1**). These results suggest another important task of PV[+] interneurons in consolidating fast inhibition of local field oscillations. For this reason, enhancing or restoring myelination of inhibitory PV[+] interneurons at the right developmental stage might lessen the symptoms of diseases in which dysmyelination is a prominent feature.

Genetic mouse models linking myelin alterations and schizophrenia

Schizophrenia is a polygenetic disorder, in which hundreds of genomic loci have been revealed to be highly involved with the onset and development of the disease[70]. In this thesis, two genetic mutations were studied, one of them linked to oligodendroglia and the other one involving a microdeletion containing several genes.

In *Chapter 7*, we studied a mouse model harbouring a mutation in the Formin-binding protein 1 (FNBP1), previously found to be disrupted in carriers of the 22q11.2

mutation[71]. FNBP1 is important for membrane curvature, and our hypothesis relied on whether mutations in this protein highly expressed in oligodendrocytes would have a detrimental effect over myelination of PV^{+} cells. Our results showed that FNBP1 is not crucial for myelination of interneurons and that other mechanisms might be involved on this process (**Figure 7.5**). Actin filaments are essential for ensheathment of the axon by oligodendrocytes, and disassembly of these filaments is required for the spreading of the myelin sheath[72]. For this dynamic process, associated Arp2/3 proteins are necessary, among which F-BAR proteins mediate membrane changes[73]. Our most sensible theory is that FNBP1, a type of F-BAR protein, is not specific for the myelinating process of PV[+] interneurons, and might be involved in other adjustments of the membrane of oligodendrocytes, but further protein-interaction analysis and functionality experiments should be conducted. Another hypothesis is that proteins other than F-BAR, such as Juxtanodin, are involved in the rearrangement of actin processes important for myelination[74]. Eventually, F-actin and G-actin have been found to be decreased in schizophrenia patients together with a decrease of myelin basic protein, suggesting that cytoskeletal deficiencies, despite not involving FNBP1, are a hallmark of schizophrenia[75,76].

Our second study focused on 22q11 deletion syndrome (22q11DS). Contrary to what most of the previous literature had reported[77,78], we found that PV[+] interneurons were hyperexcitable, showing increased firing frequency and lower current depolarisations, reduced AP threshold and rheobase (**Figure 8.1**). Notably, potassium channels $K_v1.1$ were underexpressed in these cells. Potassium channels restore the equilibrium of the AP; therefore, they hold an important role to control neuronal excitability. Many alterations in potassium-channel genes have been associated with schizophrenia or information processing in this disorder[79,80]. Voltage-gated potassium channels are in close relationship with myelin as they sit next to the internodes to initiate and propagate the AP. Disruption of the myelin sheath may lead to the reorganisation of potassium channels in the nodes and to aberrant potassium current[81,82].

Voltage-gated K_v1 and K_v3 channels are of great importance in PV[+] interneurons, as they control the latency, threshold and the high-frequency repetitive pattern[83-85], characteristic of these cells. In *Chapter 8*, we observed a decrease in the expression of $K_v1.1$ channels, together with a reduction in $K_v1.1$-specific potassium currents and application of activators partially recovered some of the features of these cells, similar to what we discovered in *Chapter 6* and $K_v3.1$ channels (**Figure 6.7, 8.4**). However, the involvement of other potassium channels, such as TREK[86,87] or even $K_v3.1$ channels, that have been implicated in 22q11DS, were not addressed in our studies. Additionally, other intermediary molecules can intervene in the excitability of neurons. Neuroregulin-

1 (NRG1) is a neurotrophic factor that activates ErbB receptors and has been widely linked to schizophrenia[88]. NRG1-ErbB signalling pathway plays a fundamental role in CNS myelination by supporting oligodendrocyte differentiation and myelination[89,90]. Notably, NRG1 is also strongly expressed in PV$^+$ interneurons[91,92] and, more interestingly, it also regulates their excitability through $K_v1.1$ channels[93]. Thus, NRG1-ErbB signalling could be a potential strategy to further understand PV-linked diseases and a potential therapeutic target for regulating network excitability of diseases such as schizophrenia.

Overall, among the animals that model 22q11DS or its related proteins, only TBX1 has been directly linked to myelin impairments. Nonetheless, PV$^+$ interneurons and potassium channels have been repeatedly reported to be affected by the deletion. This permits the development of new specific targets that modulate network excitability, and possibly downregulate the neural deficits associated with schizophrenia.

Conclusion

Myelination is an important characteristic of pyramidal cells and subtypes of interneurons. The axon of these cells needs to fulfil certain morphological requirements, besides some other possible molecular cues, to become myelinated. Such morphological traits are maintained across species, though slightly divergent between cell types, suggesting that the myelination process has been preserved through evolution.

When myelination is lost or cells in the CNS are abnormally myelinated by pathological causes, network activity becomes imbalanced. PV$^+$ interneurons - which can regulate neuronal network excitability through inhibitory synapses onto pyramidal cells, other interneurons or contacting themselves through autapses - lose this ability when they do not develop properly due to the lack of myelination. In this context, the neuronal network becomes disrupted and pathological mechanisms arise. Similarly, when PV$^+$ excitability is altered due to intrinsic abnormalities in their channel composition or performance, excitation/inhibition balance is interrupted. These disturbances in the excitation/inhibition equilibrium have been widely linked with neuropsychiatric disorders.

Hence, understanding the fundamental mechanisms of myelination and, in particular, myelination of inhibitory GABAergic interneurons, can shed light into novel therapeutic targets that can correct or reverse abnormalities of myelination and enhance the associated cognitive decline and other positive and negative symptoms that afflict patients with schizophrenia.

References

1. Allen, N. J. & Lyons, D. A. Glia as Architects of Central Nervous System Formation and Function. Science 362, 181 (2018).
2. Suminaite, D., Lyons, D. A. & Livesey, M. R. Myelinated axon physiology and regulation of neural circuit function. Glia 67, 2050 (2019).
3. Stiefel, K. M., Torben-Nielsen, B. & Coggan, J. S. Proposed evolutionary changes in the role of myelin. Front. Neurosci. 7, (2013).
4. Crotty, P., Sangrey, T. & Levy, W. B. Metabolic energy cost of action potential velocity. J. Neurophysiol. 96, 1237–1246 (2006).
5. Stadelmann, C., Timmler, S., Barrantes-Freer, A. & Simons, M. Myelin in the Central Nervous System: Structure, Function, and Pathology. Physiol Rev 99, 1381–1431 (2019).
6. Almeida, R. G. The rules of attraction in central nervous system myelination. Front. Cell. Neurosci. 12, 367 (2018).
7. Redmond, S. A. et al. Somatodendritic Expression of JAM2 Inhibits Oligodendrocyte Myelination. Neuron 91, 824–836 (2016).
8. Bechler, M. E., Byrne, L. & Ffrench-Constant, C. CNS Myelin Sheath Lengths Are an Intrinsic Property of Oligodendrocytes. Curr. Biol. 25, 2411–2416 (2015).
9. Perge, J. A., Niven, J. E., Mugnaini, E., Balasubramanian, V. & Sterling, P. Why Do Axons Differ in Caliber? J. Neurosci. 32, 626–638 (2012).
10. Goldstein, S. S. & Rall, W. Changes of Action Potential Shape and Velocity for Changing Core Conductor Geometry. Biophys. J. 14, 731 (1974).
11. Costa, A. R., Pinto-Costa, R., Sousa, S. C. & Sousa, M. M. The Regulation of Axon Diameter: From Axonal Circumferential Contractility to Activity-Dependent Axon Swelling. Front. Mol. Neurosci. 11, 319 (2018).
12. Chéreau, R., Saraceno, G. E., Angibaud, J., Cattaert, D. & Nägerl, U. V. Superresolution imaging reveals activity-dependent plasticity of axon morphology linked to changes in action potential conduction velocity. Proc. Natl. Acad. Sci. U. S. A. 114, 1401–1406 (2017).
13. Marygold, S. J. & Leevers, S. J. Growth Signaling: TSC Takes Its Place. Curr. Biol. 12, R785–R787 (2002).
14. Duncan, D. The Importance of Diameter as a Factor in Myelination. Science (80-.). 79, 363–363 (1934).
15. Tomassy, G. S. et al. Distinct Profiles of Myelin Distribution. Science (80-.). 344, 319–324 (2014).
16. Nave, K.-A. Myelination and the trophic support of long axons. Nat. Rev. Neurosci. 2010 114 11, 275–283 (2010).
17. Zonouzi, M. et al. Individual Oligodendrocytes Show Bias for Inhibitory Axons in the Neocortex. Cell Rep. 27, 2799-2808.e3 (2019).
18. Kawaguchi, Y. & Kubota, Y. GABAergic cell subtypes and their synaptic connections in rat frontal cortex. Cereb. Cortex 7, 476–486 (1997).
19. Stedehouder, J. et al. Fast-spiking Parvalbumin Interneurons are Frequently Myelinated in the Cerebral Cortex of Mice and Humans. Cereb. Cortex 27, 5001–5013 (2017).
20. Stedehouder, J. et al. Local axonal morphology guides the topography of interneuron myelination in mouse and human neocortex. Elife 8, (2019).
21. Call, C. L., Bergles, D. E. & Snyder, S. H. Remyelination restores myelin content on distinct neuronal subtypes in the cerebral cortex.
22. Gibson, E. M. et al. Neuronal activity promotes oligodendrogenesis and adaptive myelination in the mammalian brain. Science (80-.). 1252304, (2014).
23. Stedehouder, J., Brizee, D., Shpak, G. & Kushner, S. A. Activity-Dependent Myelination of Parvalbumin Interneurons Mediated by Axonal Morphological Plasticity. J. Neurosci. 38, 3631–3642 (2018).
24. Gargareta, V. I. et al. Conservation and divergence of myelin proteome and oligodendrocyte transcriptome profiles between humans and mice. Elife 11, 77019 (2022).
25. Ishii, A. et al. Human myelin proteome and comparative analysis with mouse myelin. Proc. Natl. Acad. Sci. U. S. A. 106, 14605–14610 (2009).
26. Krafft, P. R. et al. Etiology of stroke and choice of models. Int. J. Stroke 7, 398 (2012).
27. Poulen, G. et al. Coherent Anti-Stokes Raman Scattering Microscopy: A Label-Free Method to Compare Spinal Cord Myelin in Different Species. Front. Phys. 9, 438 (2021).
28. Hodge, R. D. et al. Conserved cell types with divergent features in human versus mouse cortex. Nat. 2019 5737772 573, 61–68 (2019).
29. Miller, D. J. et al. Prolonged myelination in human neocortical evolution. Proc. Natl. Acad. Sci. U. S. A. 109, 16480–16485 (2012).

30. Xin, W. & Chan, J. R. Myelin plasticity: sculpting circuits in learning and memory. Nat. Rev. Neurosci. 21, 682 (2020).

31. Scholz, J., Klein, M. C., Behrens, T. E. J. & Johansen-Berg, H. Training induces changes in white matter architecture. Nat. Neurosci. 12, 1370 (2009).

32. Schlegel, A. A., Rudelson, J. J. & Tse, P. U. White matter structure changes as adults learn a second language. J. Cogn. Neurosci. 24, 1664–1670 (2012).

33. Steele, C. J., Bailey, J. A., Zatorre, R. J. & Penhune, V. B. Early Musical Training and White-Matter Plasticity in the Corpus Callosum: Evidence for a Sensitive Period. J. Neurosci. 33, 1282–1290 (2013).

34. Bacmeister, C. M. et al. Motor learning promotes remyelination via new and surviving oligodendrocytes. Nat. Neurosci. 2020 237 23, 819–831 (2020).

35. Xin, W. & Chan, J. R. Motor learning revamps the myelin landscape. Nat. Neurosci. 2022 2510 25, 1251–1252 (2022).

36. Gao, Z. K. et al. Enriched Environment Effects on Myelination of the Central Nervous System: Role of Glial Cells. Neural Plast. 2022, (2022).

37. Hughes, E. G., Orthmann-Murphy, J. L., Langseth, A. J. & Bergles, D. E. Myelin remodeling through experience-dependent oligodendrogenesis in the adult somatosensory cortex. Nat. Neurosci. 21, 696–706 (2018).

38. Makinodan, M., Rosen, K. M., Ito, S. & Corfas, G. A critical period for social experience-dependent oligodendrocyte maturation and myelination. Science (80-.). 337, 1357–1360 (2012).

39. Liu, J. et al. Impaired adult myelination in the prefrontal cortex of socially isolated mice. Nat. Neurosci. 2012 1512 15, 1621–1623 (2012).

40. Herrmann, E., Call, J., Hernández-Lloreda, M. V., Hare, B. & Tomasello, M. Humans have evolved specialized skills of social cognition: the cultural intelligence hypothesis. Science 317, 1360–1366 (2007).

41. Toritsuka, M., Makinodan, M. & Kishimoto, T. Social Experience-Dependent Myelination: An Implication for Psychiatric Disorders. Neural Plast. 2015, 465345 (2015).

42. Miller, E. M. Intelligence and brain myelination: A hypothesis. Pers. Individ. Dif. 17, 803–832 (1994).

43. Ritchie, S. J. et al. Coupled Changes in Brain White Matter Microstructure and Fluid Intelligence in Later Life. J. Neurosci. 35, 8672 (2015).

44. Chiang, M. C. et al. Genetics of Brain Fiber Architecture and Intellectual Performance. J. Neurosci. 29, 2212 (2009).

45. Hill, W. D. et al. A combined analysis of genetically correlated traits identifies 187 loci and a role for neurogenesis and myelination in intelligence. Mol. Psychiatry 24, 169 (2019).

46. Roots, B. I. The phylogeny of invertebrates and the evolution of myelin. Neuron Glia Biol. 4, 101–109 (2008).

47. Sachdev, P. S., Zhuang, L., Braidy, N. & Wen, W. Is Alzheimer's a disease of the white matter? Curr. Opin. Psychiatry 26, 244–251 (2013).

48. Casella, C., Lipp, I., Rosser, A., Jones, D. K. & Metzler-Baddeley, C. A Critical Review of White Matter Changes in Huntington's Disease. Mov. Disord. 35, 1302–1311 (2020).

49. Kubicki, M., McCarley, R. W. & Shenton, M. E. Evidence for white matter abnormalities in schizophrenia. Curr. Opin. Psychiatry 18, 121 (2005).

50. Serafini, G., Gonda, X., Rihmer, Z., Girardi, P. & Amore, M. White matter abnormalities: Insights into the pathophysiology of major affective disorders. World J. Radiol. 6, 223 (2014).

51. Vandewouw, M. M., Hunt, B. A. E., Ziolkowski, J. & Taylor, M. J. The developing relations between networks of cortical myelin and neurophysiological connectivity. Neuroimage 237, 118142 (2021).

52. Buzsáki, G. & Wang, X. J. Mechanisms of Gamma Oscillations. Annu. Rev. Neurosci. 35, 203 (2012).

53. Sohal, V. S., Zhang, F., Yizhar, O. & Deisseroth, K. Parvalbumin neurons and gamma rhythms enhance cortical circuit performance. Nat. 2009 4597247 459, 698–702 (2009).

54. Hu, H., Gan, J. & Jonas, P. Fast-spiking, parvalbumin+ GABAergic interneurons: From cellular design to microcircuit function. Science (80-.). 345, (2014).

55. Pajevic, S., Basser, P. J. & Fields, R. D. Role of Myelin Plasticity in Oscillations and Synchrony of Neuronal Activity. Neuroscience 276, 135 (2014).

56. Uhlhaas, P. J. & Singer, W. Abnormal neural oscillations and synchrony in schizophrenia. Nat. Rev. Neurosci. 2010 112 11, 100–113 (2010).

57. Tewarie, P. et al. Disruption of structural and functional networks in long-standing multiple sclerosis. Hum. Brain Mapp. 35, 5946–5961 (2014).

58. Benamer, N., Vidal, M., Balia, M. & Angulo, M. C. Myelination of parvalbumin interneurons shapes the function of cortical sensory inhibitory circuits. Nat. Commun. 11, 5151 (2020).

59. Bacci, A. & Huguenard, J. R. Enhancement of spike-timing precision by autaptic transmission in neocortical

inhibitory interneurons. Neuron 49, 119–130 (2006).

60. Deleuze, C. et al. Strong preference for autaptic self-connectivity of neocortical PV interneurons facilitates their tuning to γ-oscillations. (2019).

61. Micheva, K. D., Kiraly, M., Perez, M. M. & Madison, D. V. Extensive Structural Remodeling of the Axonal Arbors of Parvalbumin Basket Cells during Development in Mouse Neocortex. J. Neurosci. 41, 9326–9339 (2021).

62. Fields, R. D. A new mechanism of nervous system plasticity: activity-dependent myelination. Nat. Rev. Neurosci. 2015 1612 16, 756–767 (2015).

63. Dubey, M. et al. Myelination synchronizes cortical oscillations by consolidating parvalbumin-mediated phasic inhibition. Elife 11, 1–24 (2022).

64. Hamada, M. S. & Kole, M. H. P. Myelin Loss and Axonal Ion Channel Adaptations Associated with Gray Matter Neuronal Hyperexcitability. J. Neurosci. 35, 7272–7286 (2015).

65. Lewis, D. A. Cortical circuit dysfunction and cognitive deficits in schizophrenia--implications for preemptive interventions. Eur. J. Neurosci. 35, 1871–8 (2012).

66. Benedict, R. H. B., Amato, M. P., DeLuca, J. & Geurts, J. J. G. Cognitive impairment in multiple sclerosis: clinical management, MRI, and therapeutic avenues. Lancet Neurol. 19, 860–871 (2020).

67. Noori, R. et al. Activity-dependent myelination: A glial mechanism of oscillatory self-organization in large-scale brain networks. Proc. Natl. Acad. Sci. U. S. A. 117, 13227 (2020).

68. Lewis, D. A., Hashimoto, T. & Volk, D. W. Cortical inhibitory neurons and schizophrenia. Nat. Rev. Neurosci. 2005 64 6, 312–324 (2005).

69. Lewis, D. A., Curley, A. A., Glausier, J. R. & Volk, D. W. Cortical Parvalbumin Interneurons and Cognitive Dysfunction in Schizophrenia. Trends Neurosci. 35, 57 (2012).

70. Ripke, S. et al. Biological insights from 108 schizophrenia-associated genetic loci. Nat. 2014 5117510 511, 421–427 (2014).

71. Lin, A. An integrative approach to linking genes, brain, and behavior in 22q11.2 copy number variations. (2021).

72. Zuchero, J. B. et al. Article CNS Myelin Wrapping Is Driven by Actin Disassembly. Dev. Cell 34, 152–167 (2015).

73. Liu, S., Xiong, X., Zhao, X., Yang, X. & Wang, H. F-BAR family proteins, emerging regulators for cell membrane dynamic changes - From structure to human diseases. J. Hematol. Oncol. 8, 1–14 (2015).

74. Brockschnieder, D., Sabanay, H., Riethmacher, D. & Peles, E. Ermin, A Myelinating Oligodendrocyte-Specific Protein That Regulates Cell Morphology. J. Neurosci. 26, 757 (2006).

75. Matthews, P. R., Eastwood, S. L. & Harrison, P. J. Reduced Myelin Basic Protein and Actin-Related Gene Expression in Visual Cortex in Schizophrenia. PLoS One 7, e38211 (2012).

76. Bhambhvani, H. P., Mueller, T. M., Simmons, M. S. & Meador-Woodruff, J. H. Actin polymerization is reduced in the anterior cingulate cortex of elderly patients with schizophrenia. Transl. Psychiatry 2017 712 7, 1–7 (2017).

77. Marissal, T. et al. Restoring wild-type-like CA1 network dynamics and behavior during adulthood in a mouse model of schizophrenia. Nat. Neurosci. 21, 1412–1420 (2018).

78. Mukherjee, A., Carvalho, F., Eliez, S. & Caroni, P. Long-Lasting Rescue of Network and Cognitive Dysfunction in a Genetic Schizophrenia Model. Cell 178, 1387-1402.e14 (2019).

79. Bruce, H. A. et al. Potassium Channel Gene Associations with Joint Processing Speed and White Matter Impairments in Schizophrenia. Genes. Brain. Behav. 16, 515 (2017).

80. Jaffe, A. E. et al. Developmental and genetic regulation of the human cortex transcriptome illuminate schizophrenia pathogenesis. Neuroscience 12, (2018).

81. Rasband, M. N. et al. Potassium Channel Distribution, Clustering, and Function in Remyelinating Rat Axons. J. Neurosci. 18, 36–47 (1998).

82. Shi, R. & Sun, W. Potassium channel blockers as an effective treatment to restore impulse conduction in injured axons. Neurosci. Bull. 27, 36 (2011).

83. Rudy, B. & Mcbain, C. J. Kv3 channels : voltage-gated K + channels designed for high-frequency repetitive firing. Trends Neurosci. 24, 517–526 (2001).

84. Gittelman, J. X. & Tempel, B. L. Kv1.1-containing channels are critical for temporal precision during spike initiation. J. Neurophysiol. 96, 1203–1214 (2006).

85. Goldberg, E. M. et al. K + Channels at the Axon Initial Segment Dampen Near-Threshold Excitability of Neocortical. Cell 387–400 (2008).

86. Piskorowski, R. A. et al. Age-Dependent Specific Changes in Area CA2 of the Hippocampus and Social Memory Deficit in a Mouse Model of the 22q11.2 Deletion Syndrome. Neuron 89, 163–176 (2016).

87. Donegan, M. L. et al. Coding of social novelty in the hippocampal CA2 region and its disruption and rescue in a 22q11.2 microdeletion mouse model. Nat. Neurosci. 2020 2311 23, 1365–1375 (2020).

88. Stefansson, H. et al. Neuregulin 1 and Susceptibility to Schizophrenia. Am. J. Hum. Genet. 71, 877–892 (2002).

89. Vartanian, T., Fischbach, G. & Miller, R. Failure of spinal cord oligodendrocyte development in mice lacking neuregulin. Neurobiology 96, 731–735 (1999).

90. Roy, K. et al. Loss of erbB signaling in oligodendrocytes alters myelin and dopaminergic function, a potential mechanism for neuropsychiatric disorders. Proc. Natl. Acad. Sci. U. S. A. 104, 8131 (2007).

91. Vullhorst, D. et al. Selective Expression of ErbB4 in Interneurons, But Not Pyramidal Cells, of the Rodent Hippocampus. J. Neurosci. 29, 12255 (2009).

92. Fazzari, P. et al. Control of cortical GABA circuitry development by Nrg1 and ErbB4 signalling. Nat. 2010 4647293 464, 1376–1380 (2010).

93. Li, K.-X. et al. Neuregulin 1 regulates excitability of fast-spiking neurons through Kv1.1 and acts in epilepsy. Nat. Publ. Gr. 15, (2011).

Appendices

Summary

Myelin is the insulating lipidic sheath that partially covers some of the axons in both the peripheral and central nervous system. In the latter, oligodendrocytes are the glial cells in charge of forming myelin layers around the axons to enhance the conduction velocity and reduce the metabolic consumption of neurons. However, the mechanisms that explain myelination of certain neuronal subtypes are uncovered yet.

In *chapters 2, 3* and *4* we show that morphology is significantly important to predict segmental myelination in both pyramidal cells and GABAergic interneurons in layers II-III of the neocortex. Notably, myelination of pyramidal cells is also region dependent. GABAergic interneurons show different degrees of myelination highly dependent on the cellular profile and their firing frequency. Whilst PV$^+$ interneurons are highly myelinated, other non-fast-spiking interneurons show little to no myelination. Remarkably, in all studied cellular types, human neurons present more cortical myelination than mice, evidencing species divergences.

Understanding the myelination process in cortical areas can shed light to the mechanism underlying the pathophysiology of demyelinating diseases, such as multiple sclerosis and schizophrenia. Cognitive decline, a hallmark to both disorders, is characterised by impaired cortical and cellular connections, desynchronisation and excitation/inhibition imbalance. In this thesis, *chapters 5* and *6* employ the cuprizone mouse model to show that myelinisation of GABAergic interneurons plays a crucial role the synchronisation of the system, the cellular connectivity and the excitability of these cells. Notably, the neurodevelopmental stage at which demyelination occurs can produce different outcomes. Whereas juvenile demyelination of PV$^+$ interneurons causes a reduced number of self-inhibitory contact points, demyelination at a later stage point did not reduce the number of autapses but reduced their excitability. Interestingly, shiverer mice show a similar phenotype to juvenile demyelination. Furthermore, re-myelination partially recovered the detrimental effects caused upon cuprizone treatment.

Chapters 7 and *8* employ two mouse models that carry a mutation found in schizophrenia patients. In *chapter 7*, deletion of the FNBP1 gene, does not cause any impairments to the myelination of PV$^+$ interneurons, indicating that this gene is not essential for this process. *Chapter 8* describes that the 22q11 deletion increases the excitability of PV$^+$ interneurons in the hippocampus without affecting their myelination status. This hyperexcitability is possibly partially driven by the malfunctioning of $K_v1.1$ potassium channels in these cellular subtypes.

Taken together, these results open new targets and experimental approaches to develop drugs to halt or revert the effects of demyelination and therefore lessen the symptoms of patients.

Samenvatting

Myeline is de insulerende vettige laag die axonen bedekt in het perifere en centrale zenuwstelsel. Oligodendrocyten zijn de glia cellen die verantwoordelijk zijn voor deze myelinescheden in het centrale zenuwstelsel om de geleiding te versnellen en metabolische consumptie te verminderen. Het mechanisme dat verklaart waarom bepaalde neuronale cellen myeline hebben is nog niet ontdekt.

In *hoofdstukken 2, 3* en *4* laten we zien dat de morfologie erg belangrijk is bij het voorspellen van segmentale myelinisatie in zowel piramidecellen als GABAerge interneuronen in laag II-III van de neocortex. Opvallend is dat myelinisatie van piramidecellen ook afhankelijk is van de regio. GABAerge interneuronen laten verschillende gradaties van myelinisatie zien afhankelijk van het celullaire profiel en de frequentie waarmee zij actiepotentialen afvuren. Hoewel PV$^+$ interneurons zeer gemyeliniseerd zijn, laten andere snel vurende interneuronen amper tot geen myelinisatie zien. Merkwaardig genoeg is er in verschillende soorten corticale neuronen van mensen meer myelinisatie aanwezig dan diezelfde cellen van muizen. Dit wijst op een divergentie in diersoort.

Het begrijpen van het myelinisatieproces in corticale gebieden van de hersenen kan het mechanisme belichten van de pathofysiologie van demyelinisatie aandoeningen, zoals multiple sclerosis en schizofrenie. Cognitieve achteruitgang, een symptoom bij beide aandoeningen, wordt gekarakteriseerd door verzwakte corticale en cellulaire connecties, desynchronisatie en een onbalans tussen excitatie en inhibitie. In dit proefschrift behandelen *hoofdstukken 5* en *6* het cuprizone muismodel om aan te tonen dat myelinisatie van GABAerge interneuronen een cruciale rol speelt voor het synchroniseren van het systeem, de connectiviteit tussen cellen en exciteerbaarheid van cellen. Met name de ontwikkelingsfase waarin demyelinisatie plaatsvindt, kan verschillende resultaten laten zien. Demyelinisatie van PV$^+$ interneuronen in een jonge fase vermindert het aantal zelf-inhiberende contactpunten, terwijl demyelinisatie in een latere fase deze autapses niet vermindert maar wel de excitatie van de cellen vermindert. Het fenotype in shiverer muizen is vergelijkbaar met demyelinisatie in de jonge fase. Bovendien kan re-myelinisatie de schade van behandeling met cuprizone gedeeltelijk herstellen.

Hoofdstukken 7 en *8* behandelen twee muismodellen die een mutatie dragen die is gevonden in patiënten met schizofrenie. In *hoofdstuk 7* laten wij zien dat deletie van het gen FNBP1 geen beperking veroorzaakt voor myelinisatie van PV$^+$ interneuronen, dus dit gen speelt geen belangrijke rol in dit proces. In *hoofdstuk 8* laten wij zien dat de 22q11 deletie zorgt voor meer excitatie van PV$^+$ interneuronen zonder dat het de myelinisatie verandert. Deze hyperexcitatie wordt waarschijnlijk aangestuurd door K_v1.1 kaliumkanalen die niet meer goed werken in deze type cellen.

Bij elkaar genomen, bieden deze resultaten nieuwe doelwitten en experimentele methoden aan voor het ontwikkelen van medicijnen om demyelinisatie te remmen of te herstellen en zo de symptomen in patiënten te verminderen.

Resumen

La mielina es el recubrimiento lipídico que cubre parcialmente algunos axones en el sistema nervioso central y periférico. En el primero, los oligodendrocitos son las células gliales encargadas de formar capas de mielina que rodean los axones y permiten que la conducción del potencial de acción sea más rápida a la vez que reduce el consumo metabólico de las neuronas. Sin embargo, los mecanismos que explican por qué ciertos tipos neuronales presentan mielina mientras que otros no, aún no han sido descritos.

En los capítulos 2, 3 y 4 demostramos que la morfología del axón es importante para predecir la mielinización de ciertos axones tanto en células piramidales como en las GABAérgicas en las capas II-III de la corteza cerebral. Además, la mielinización de las células piramidales también varía de acuerdo a la región del cerebro en la que se encuentran. Las interneuronas GABAérgicas muestran diferentes grados de mielinización dependiendo del perfil celular y de la frecuencia de disparo. Mientras que las interneuronas PV+ se encuentran altamente mielinizadas, otras interneuronas con menor frecuencias de disparo tienen mielina. Notablemente, en todos los subtipos celulares estudiados, las neuronas de origen humano presentan más mielina, evidenciando las diferencias entre especies.

Entender el proceso de la mielinización de las áreas corticales puede ayudar a comprender los mecanismos que rodean la patofisiología de las enfermedades desmielinizantes, como la esclerosis múltiple o la esquizofrenia. El deterioro cognitivo, tan relevante en ambas enfermedades, se caracteriza por la deficiencia de conexiones corticales y celulares, la desincronización del sistema y el desequilibrio entre excitación e inhibición. En esta tesis, los capítulos 5 y 6 emplean el modelo murino de cuprizona para demostrar que la mielinización de las interneuronas GABAérgicas mantiene un papel fundamental en la sincronización de sistema, de la conectividad neuronal y en la excitabilidad de dichas células. Curiosamente, el momento del desarrollo en el que se produce la desmielinización marca las consecuencias. Mientras que la desmielinización juvenil de las células PV+ reduce el número de autapsis, una desmielinización más tardía no afecta al número de autapsis pero sí reduce la excitabilidad de las neuronas. Además, la remielinización recupera algunos de los efectos de la cuprizona.

Los capítulos 7 y 8 utilizan dos modelos con mutaciones encontradas en pacientes que padecen esquizofrenia. En el capítulo 7, la deleción del gen FNBP1 no causa ninguna deficiencia en la mielina de las células PV+, indicando que este gen no es esencial para este proceso. El capítulo 8 describe que la deleción 22q11 incrementa la excitabilidad de las neuronas PV+ en el hipocampo sin llegar a afectar a su mielinización. Esta hiperexcitabilidad puede estar parcialmente causada por un defecto en los canales de potasio Kv1.1.

En conclusión, estos resultados promueven la aparición de nuevas dianas terapéuticas para parar o revertir los efectos de la desmielinización, y así reducir los síntomas de los pacientes.

Curriculum Vitae

María Pascual García was born on October 25th 1994 in Ciudad Real, Spain. She graduated from the BSc degree in Biomedical Sciences from the Universitat Autònoma de Barcelona in 2016, after completion of her BSc thesis under the supervision of Dr. Jordi Ortiz. Additionally, she worked in the department of Neurobiology of stress and psychopathology vulnerability with the guidance of Prof. dr. Antonio Armario and Prof. dr. Roser Nadal. Next, she enrolled in the Master's Program of Neuroscience at the Vrije Universiteit in Amsterdam, where she worked under the surveillance of Dr. Mark Verheijen and participated in a second internship and MSc thesis supervised by Prof. dr. Maarten Kole. After attaining her MSc degree in 2018, she started working on her PhD thesis under the supervision of Prof. dr. Steven Kushner at the Department of Psychiatry of the Erasmus MC, Rotterdam.

PhD Porfolio

Name	María Pascual García
PhD period	2018 - 2022
Department	Psychiatry Erasmus MC
Promotor	Prof. dr. Steven Kushner
Co-promotor	Dr. Sara Hijazi
Graduate school	ONWAR

Education

PhD Neuroscience at Erasmus MC (Rotterdam, the Netherlands)	2018 - 2022
MSc Neuroscience at Vrije Universiteit (Amsterdam, the Netherlands)	2016 - 2018
BSc Biomedical Sciences at Universitat Autònoma de Barcelona (Barcelona, Spain)	2012 - 2016

Conferences and awards

Dutch Neuroscience Meeting	2018
Axons in the Hills	2018
ONWAR Annual Meeting	2018
Dutch Neuroscience Meeting – Poster presentation	2019
ONWAR Annual Meeting – Poster presentation	2019
FENS – Poster presentation - *FENS-IBRO/PERC grant*	2020
European Glia Meeting - Poster presentation – *Network Glia stipend award*	2021
ONWAR Annual Meeting - Talk	2021
SfN annual meeting - Poster presentation – *TPDA award*	2021
Dutch Neuroscience Meeting – Talk	2022
FENS – Poster presentation	2022

Teaching activities

Supervisor BSc Student – Anke Tolido	2020-2021
Supervisor MSc Student – Yara Nabawi	2021
Supervisor BSc Student – Anh Pham	2021-2022
Patch-clamp workshop Neuroscience master	2021
Supervision Wiki-assignment for Neural signaling and computation course	2021-2022

PhD training courses

Animal welfare course – Erasmus MC	2019
Integrity course - Erasmus MC	2020
Statistics with R - Coursera	2020
Python for science - ONWAR	2021
Grant writing - ONWAR	2021
Biomedical writing – Erasmus MC	2022

List of publications

Pascual-Garcia M, Hijazi S, Unkel M, Slotman JA, Bolleboom A, Bouwen BL, Houtsmuller AB, Dirven C, Gao Z, Kushner SA. Axonal morphology predicts region-dependent myelination of pyramidal cells in human and mouse neocortex. *Manuscript in preparation.*

Pascual-Garcia M, Hijazi S, Unkel M, Slotman JA, Bolleboom A, Bouwen BL, Houtsmuller AB, Dirven C, Gao Z, Kushner SA. Human and mice non-fast-spiking interneurons show similarities in classification and properties but diverge in myelination profile. *Manuscript in preparation.*

Pascual-Garcia M*, Hijazi S*, Pham TPA, Tolido A, Kushner SA. Dysfunctional parvalbumin interneurons in a genetic mouse model of schizophrenia. *Manuscript in preparation.*

Pascual-Garcia M, Hijazi S, Pham TPA, Kushner SA. Deficits in actin polymerization enhancer FNBP1 does not alter the properties and myelination profile of parvalbumin-positive interneurons. *Manuscript in preparation.*

Hijazi S, **Pascual-Garcia M**, Nabawi, Y, Pilati N, Large CH, Kushner SA. A critical period for prefrontal cortex PV neuron myelination and maturation. *Manuscript in preparation.*

Stedehouder J, Brizee D, Slotman JA, **Pascual-Garcia M**, Leyrer ML, Bouwem BL, Driven CM, Gao Z, Berson DM, Hotsmuller AB, Kushner SA (2019). Local axonal morphology guides the topography of interneuron myelination in mouse and human neocortex. *eLife 8:e48615*.

Dubey M, **Pascual-Garcia M**, Helmes K, Wever DD, Hamada MS, Kushner SA, Kole MHP (2022). Myelination synchronizes cortical oscillations by consolidating parvalbumin-mediated phasic inhibition. *eLife* 11:e73827.

*Authors contributed equally

Acknowledgments

If you reached this point… you probably skipped about 250 pages. In the next lines I want to thank all the people that accompanied me on this journey. It has been four years where I have experienced so many wonderful and fearful moments, and where I have learned a lot of science, but foremost, I have grown as a person.

First of all, I want to thank Professor *Steven Kushner* for giving me the opportunity to work on a wonderful thesis and give me the freedom to develop my professional career. Also, to Dr *Sara Hijazi*, for having the immense patience to teach me, guide me and discuss all possible (scientific) ideas with me. Thank you for all the trust and support that you gave me and for being always available to listen to me.

Next, to the reading committee, Professor *María Cecilia Angulo*, Professor *Ype Elgersma* and Dr *Femke de Vrij*. Thank you for reading and your input on the first draft of the thesis. Also, to all the other members of the committee, Dr *Tjakko van Ham,* Dr *Zhenyu Gao* and Dr *Vivi Heine,* thank you for being part of this day.

To all the present and former colleagues of the Kushner-de Vrij lab: *Amir, Anniek, Bas, Christian, Denise, Diana, Femke, Guy, Hilde, Juliette, Jurate, Marlen, Mark, Maurits, Merel, Mernoush, Mirle, Pomme, Sakshi* and *Sophie*. It was a pleasure to work with all of you and to learn from so many different fields and cultures. I will take with me all the jokes, the trips and the parties and particularly, the terrible romcoms and Christmas movies that (unfortunately) I will never forget. Also, I would like to thank some of the students that spent several years with me, *Esmée* and *John*, and specially to those who helped me along these years and that also contributed in this thesis, *Anke*, *Yara* and *Anh*. Lastly, I would also like to mention all the members of the *Elgersma* and *van Woerden lab*, with whom I have shared very nice moments, parties and conferences. Specially, I want to thank my paranymphs: *Pomme* and *Sakshi*, for accepting this endeavour and taking the time and energy to accompany me on this day.

I want to thank Professor *Maarten Kole*, for introducing me to the world of electrophysiology and sharing his knowledge with me. Also, to Dr *Mohit Dubey* for being a supporting shoulder whenever I needed it, both in science and personally. Thank you for teaching me to believe in myself and that science is also passion and fun. I will never forget the feeling of patching for the first time, thank you for sharing that with me.

Quiero agradecer a mis amigos de casa, los de siempre, *Adrián, Diego* y *Nieves*, por las horas y horas que han tenido que aguantarme quejándome de la falta de sol y de calor, por sacarme de aquí cuando lo único que necesitaba era un mojito en la playa y noches de baile y por descubrirme el arte de ver y hacer videos que deberían contemplarse como risoterapia. También a mis amigas de toda la vida, mis primas *Consuelo* y *Raquel*, por las eternas conversaciones alargadas días y días, y las fiestas, y los salseos, y todas las cosas que nos quedan por contar. En Barcelona, a *Silvia*, con la que he sufrido conjuntamente todo el

largo camino hacia el doctorado. Tía, ¡lo hemos conseguido! Y lo vamos a celebrar por todo el mundo, pasando frío, por descontado. Gracias por ayudarme a buscar la parte racional de todas mis tonterías, y todo siempre sin juzgar. Ahora nos toca disfrutar. I per ùltim, a la *Laura*. Van ser molts anys i moltes aventures juntes, i no crec que haguès pogut sobreviure aquí sense tu. Gràcies per regalar-me moments inolvidables al teu costat, ja sigui de festa o parlant de coses sense importància. És una sort saber que no importa on parem, sempre tornem a estar juntes i viure experiencies noves. Per tots els cumpleviajes i les nostres bogeries, gràcies i mil gràcies.

During these years, so many people have passed by my life and changed it in so many different ways. I would like to take my time to thank some people I met here. *Anna*, for that day I could not imagine I would meet such a strong woman. Thank you for your short messages, our parties and our coffee in the park, and specially thanks for being someone I will always be able to rely on. The wonderful thesis design has been made by my dear friend *Bri*. But I have so many more things to thank you for: listening to my rambling with a cup of coffee or a walk in the city, taking care of my kitties, showing me another wonderful culture, cooking, sharing anecdotes, being a wonderful captain, etc. I feel so lucky I ended up in that volleyball team. *Clara*, qué habría hecho yo en Róterdam sin ti. Gracias por cuidarme como lo haces, pero también por sacarme a perrear cuando hace falta. Y, sobre todo, gracias por demostrarme que la ciencia es lo mío y que debemos dejar el mundo del canto para otros. *Emira*, you were the first one to "adopt" me here in Rotterdam. I owe you so much for that, my experience here would not have been the same. Thank you for listening to me and giving the most perfect advice when I needed to hear them. Thanks to *Guntar,* the person I share with my passion for dancing and who introduced me to Rotterdam Latin life (siuu). *María¸* posiblemente también puedas darte por referenciada en amigos de toda la vida. Jamás creí en el destino, pero qué suerte la mía haber cambiado aquel billete de avión ese día. Gracias por traer ese pedacito de casa aquí a Holanda. *Marlen*, it was nice to share the experience of starting the PhD adventure with someone else, share worries and laughs. I missed your quick-fast steps through the corridors, but I am happy that life did not bring us apart. I also want to thank the person I met the most bizarre situation but that I can confidently say that rescued me in more than one occasion. *Victor*, thank you for the parties, the games, the beers and the chats when we were not allowed to be out, and also after. You are the best neighbour one can ever wish to have. Also, I do not to forget my *Volleyball team* with whom I have shared a lot of fun moments in and out of the field and that round up my experience in Rotterdam to be unforgettable.

Lastly, *Sebastian*, the person who has endure every minute of this thesis for four years. I do not think I have enough words to thank you for your kindness, for your quietness when listening to me, for all the help I received after my many surgeries and falls, for opening your door whenever I needed it, for not being judgemental and for always supporting me no matter where that took me. Von ganzem Herzen, ein tausendfaches Dankeschön, dafür, dass Du eine ganz besondere und wichtige Person in meinem Leben bist.